Mix, A.C., Tiedemann, R., Blum, P., et al., 2003
Proceedings of the Ocean Drilling Program, Initial Reports Volume 202

4. Site 1233[1]

Shipboard Scientific Party[2]

INTRODUCTION

Site 1233 (proposed Site SEPAC-19A) is located at 41°0.005′S, 74°26.992′W in a small forearc basin on the continental slope, at a water depth of 838 m, shoreward of the Chile Trench. Basement is likely continental crust. The continental shelf here is 30–60 km wide. Predrilling survey data include high-resolution Parasound profiles that image the site to 80 m below seafloor (mbsf) (Fig. **F1A, F1B**) (Hebbeln et al., 1995, 2001) and an 8-m sediment core (GeoB3313-3), which suggests continuous sedimentation at the site at rates of ~100 cm/k.y. within Holocene time (Lamy et al., 2001). During our approach to Site 1233, acquisition of 3.5-kHz seismic reflection data revealed well-stratified reflective layers. Based on these new data, drilling was approved to 110 mbsf (Fig. **F1C**). The intent of drilling here was to recover a very high resolution record of late Quaternary sediments. Although lower on the slope thick turbidites bury the Peru-Chile Trench as a bathymetric feature, most turbidity currents appear to be channeled away from this shallow basin.

The large-scale oceanic circulation off southern Chile includes the southward-flowing Cape Horn Current, a part of the subpolar system, and the northward-flowing Peru-Chile Current, which forms the eastern boundary of the subtropical gyre of the South Pacific (Strub et al., 1998) (Fig. **F2A**). The transition zone between these systems is currently between 40° and 45°S, coincident with the northernmost reaches of the southern westerlies. Thus, surface-water proxies at Site 1233 will be sensitive to the latitudinal position of the westerly winds.

North of Site 1233, Mediterranean (dry summer) climates prevail on the continent. To the south, heavy year-round precipitation results in alpine glaciation and rapid erosion and transport of sediment from the continent to the ocean. Interannual rainfall in this region of Chile is thought to reflect the influence of El Niño Southern Oscillation (ENSO)

F1. Digital Parasound and 3.5-kHz profiles at Site 1233, p. 20.

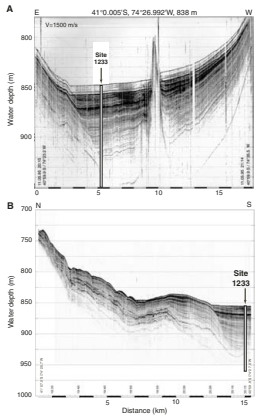

F2. Sites 1232–1235 and oceanographic features off southern and central Chile, p. 22.

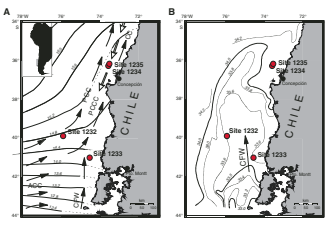

[1]Examples of how to reference the whole or part of this volume.
[2]Shipboard Scientific Party addresses.

Ms 202IR-104

events emanating from the tropics (Dettinger et al., 2001). Thus, we expect variations in terrigenous sediment composition and mineralogy at Site 1233 to reflect changes in the latitudinal position of the westerly winds through time as well as possible linkages to climate changes in the tropical Pacific. Heavy rainfall and runoff in the south results in seasonal transport of relatively low salinity surface waters, known as Chilean Fjord Waters, to the north (Fig. F2). The position of Site 1233 offers an excellent opportunity to monitor sea-surface salinity anomalies caused by variations in river runoff or by melting pulses associated with episodes of net glacier retreat.

Subsurface currents offshore include the southward-flowing Gunther Undercurrent, which can be detected as a relatively low oxygen and high salinity water mass near the shelf edge, at depths of 100–300 m (Fonseca, 1989). This current transports waters of the oxygen minimum zone, which is strongly expressed in northern Chile and Peru, as far as southern Chile. Between ~400 and 1000 m, Antarctic Intermediate Water (AAIW) enters the Pacific from the south. This water mass is relatively high in oxygen and low in salinity. We expect that benthic proxies at Site 1233 will reflect temporal changes in the intensity or character of Antarctic Intermediate Water (Fig. F3).

Primary goals for this site were to

1. Provide a high sedimentation rate site off southern Chile for study of millennial-scale (and perhaps even century scale) changes of climate related to the latitudinal position of the westerly winds. For example, geochemical and isotopic tracers of paleosalinity in near-surface waters will provide information on rainfall, runoff, and meltwater pulses; terrigenous sediments will provide information on source areas and intensity of erosion on the continent and geochemical and isotopic tracers of changes in near-surface paleotemperatures and nutrients will register changes in coastal upwelling in the transition zone between the subpolar and subtropical climate systems.
2. Provide suitable materials to monitor changes in AAIW. For example, species of benthic foraminifers and their chemical and isotopic composition may help to characterize changes in the nutrient, temperature, and, perhaps, salinity of this water mass as it enters the Pacific.

F3. North-south cross section of water masses, p. 23.

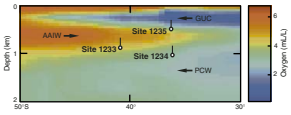

OPERATIONS

The 94-nmi voyage to Site 1233 (proposed Site SEPAC-19A) was accomplished in 10 hr at an average speed of 9.4 kt. The vessel was on station at 0945 hr on 12 April 2002.

Prior to our arrival on site, the maximum approved penetration at Site SEPAC-19A was 80 mbsf, based on the maximum penetration of Parasound seismic records obtained by the *Sonne* in 1995. On approach to the site, the *JOIDES Resolution*'s 3.5-kHz precision depth recorder (PDR) was able to record seismic reflectors to a depth of 110 mbsf. A request to drill to that depth was made to, and approved by, Ocean Drilling Program/Texas A&M University (ODP/TAMU) headquarters.

Hole 1233A

Hole 1233A was initiated with the advanced piston corer (APC) at 1350 hr on 12 April. The first attempt at a mudline core with the APC from 851 meters below rig floor (mbrf) (Core 1H) resulted in a full core barrel (9.9 m; recovery = 105%) that was not suitable for calculating the seafloor depth. This was the only core from Hole 1233A (Table T1).

T1. Operations summary, p. 54.

Hole 1233B

The bit was raised 7 m, and Hole 1233B was initiated from 844.0 mbrf at 1340 hr on 12 April. The seafloor depth calculated from the recovery of the initial core was 848.5 mbrf, 7.9 m shallower than the corrected PDR depth estimate.

Piston coring advanced without incident to 109.5 mbsf. The interval from 5 to 14.5 mbsf was drilled without coring. The cores were oriented starting with Core 2H. Downhole temperature measurements were taken with the APC temperature (APCT) tool (Table T1). Of the 100.0 m cored, 102.0 m was recovered (recovery = 102%) (Table T1). The bit was pulled free of the seafloor at 2200 hr on 12 April.

Hole 1233C

The vessel was offset 10 m southeast of Hole 1233B. Before Core 1H was shot, a bottom water temperature measurement was taken with the APCT tool. In order to obtain a stratigraphic overlap with the previous hole, the bit was positioned at a depth of 847 mbrf. Hole 1232C was initiated with the APC at 2305 hr on 12 April. The seafloor depth calculated from the recovery of the mudline core was 848.7 mbrf. Piston coring advanced to 116.3 mbsf and recovered 121.8 m of core (recovery = 105%) (Table T1). Cores were oriented starting with Core 3H. Downhole temperature measurements were obtained with the APCT tool (Table T1). The combined downhole temperature measurements taken in Holes 1233B and 1233C yielded a temperature gradient of ~4.5°C/100 m. The bit was pulled free of the seafloor at 0745 hr on 13 April.

Hole 1233D

The vessel was offset 10 m southeast of Hole 1233C. In order to obtain a stratigraphic overlap with the previous holes, the bit was positioned at a depth of 841 mbrf. Hole 1233D was initiated with the APC at 0810 hr on 13 April. A seafloor depth of 850.2 mbrf was calculated from the recovery of the mudline core. Piston coring advanced to the depth of 112.3 mbsf. The interval from 43.8 to 45.8 mbsf was drilled without coring to maintain the desired offset in regard to the cores recovered in the previous holes. A total of 110.3 m was cored and 114.9 m recovered (recovery = 104%) (Table T1). Cores were oriented starting with Core 4H. The bit was pulled free of the seafloor at 1715 hr on 13 April.

Hole 1233E

The vessel was offset 10 m southeast of Hole 1233D. The objective for this last hole was to improve the stratigraphic coverage by filling gaps in the core logging data. The bit was placed at 848 mbrf. Hole 1233E was initiated with the APC at 1750 hr on 13 April. A depth of 849.1

mbrf was calculated for the seafloor from the recovery of the mudline core. Piston coring advanced to the target depth of 101.5 mbsf. The interval from 55.9 to 82.5 mbsf was drilled without coring. The cored interval was 74.9 m with 73.7 m recovered (recovery = 98%) (Table T1). Cores were oriented starting with Core 3H.

The vessel was secured for transit. Because of the calm environment, the bottom-hole assembly was not disassembled. The two stands of drill collars were set back in the derrick, and the nonmagnetic and seal bore drill collars were laid down. The 24-hr transit to the next site began at 0400 hr on 14 April.

COMPOSITE SECTION

We built primary and secondary meters composite depth (mcd) scales and splices at Site 1233. A secondary splice was necessary because of the unusually high density of sampling requests at Site 1233. Because most of the site was quadruple cored, creation of a secondary splice was feasible. The mcd scale is constructed to align tie points between cores in the splice. Gas expansion of cores recovered at Site 1233 was unusually high and also spatially variable. Because the two splices have different tie points, when constructing a secondary splice, it was also necessary to construct a secondary mcd scale. When using one of the splices, it is critical to use the correct mcd scale.

The primary mcd scale and primary splice (as defined in "Composite Section," p. 4, in the "Explanatory Notes" chapter) ranges from the top of Core 202-1233C-1H to the bottom of Section 202-1233C-13H-8 (0.00–135.72 mcd) (see Tables T2, T3). Given the available data we conclude that 100% of the cored interval at Site 1233 was recovered in the five APC holes drilled at the site. All cores from the five holes can be placed into the composite section using the core offsets listed in Table T2.

The secondary mcd scale and secondary splice (as defined in "Composite Section," p. 4, in the "Explanatory Notes" chapter) ranges from the top of Core 202-1233B-1H to 202-1233C-13H-5, 39 cm (0.00–130.14 mcd). (See Tables T4, T5; also see the "Supplementary Materials" contents list for Splicer compatible affine and splice tables.) All cores from the five holes can be placed into the secondary composite section using the core offsets listed in Table T4. The secondary splice is discontinuous at five tie points because of a lack of two copies of the sedimentary sequence. The first gap in the secondary splice is between Section 202-1233E-4H-6, 65 cm, and Section 202-1233B-4H-1, 0 cm (39.29–39.47 mcd). The second gap is between Section 202-1233B-7H-7, 40 cm, and Section 202-1233C-9H-1, 0 cm (81.50–81.89 mcd). The third gap occurs between Section 202-1233B-10H-6, 85 cm, and Section 202-1233C-12H-1, 0 cm (113.09–114.13 mcd). The fourth gap lies between Section 202-1233C-12H-3, 65 cm, and Section 202-1233B-11H-1, 0 cm (116.58–117.05 cm). The fifth gap is between Section 202-1233D-13H-3, 20 cm, and Section 202-1233C-13H-1, 0 cm (124.72–125.05 mcd). The secondary splice ends 4.4 m before the primary splice because of the fact that this section of the sedimentary sequence at Site 1233 was recovered only once. The five gaps and the missing bottom of the splice mean that the secondary splice is missing 6.81 m (5%) of the sedimentary sequence at Site 1233.

The mcd scales and the splices are based on the stratigraphic correlation of whole-core OSU Fast Track magnetic susceptibility data (OSUS-

T2. Primary composite depth scale, p. 55.

T3. Primary splice tie points, p. 56.

T4. Secondary composite depth scale, p. 57.

T5. Secondary splice tie points, p. 58.

MS) collected at 5-cm depth intervals using 1-s integration times. OSUS-MS data for Holes 1233A, 1233B, 1233C, 1233D, and 1233E and the primary splice constructed from them are presented on the primary mcd scale in Figure **F4** and in Tables **T6, T7, T8, T9,** and **T10.** Correlations were checked using multisensor track data (MST-MS) collected at 5-cm depth intervals. The primary splice tie points (Table **T3**) were then used to construct representative spliced records for gamma ray attenuation (GRA) bulk density and natural gamma radiation (NGR) data. The spliced records of reflectance (L*), NGR, GRA, and magnetic susceptibility (MS) are presented in Figure **F5.**

Magnetic susceptibility was the most useful tool for stratigraphic correlation at Site 1233. GRA bulk density was helpful in intervals where MS structure was ambiguous. Correlation between cores from different holes was sometimes poor in the top and bottom ~1 m of cores. We interpret this lack of correlation as evidence for disturbance resulting from the effects of the coring process at Site 1233. For the primary mcd scale, we assumed that the uppermost sediment (the "mudline") in Core 202-1233C-1H was the sediment/water interface. For the secondary mcd scale, we assumed that the uppermost sediment (the "mudline") in Core 202-1233B-1H was the sediment/water interface. Comparison with site survey core GeoB3313-1 suggests that the top of Cores 202-1233C-1H and 202-1233B-1H successfully recovered near-surface sediments.

Cores 202-1233C-1H and 202-1233B-1H, the respective anchors in the primary and secondary composite depth scales, are the only cores in which depths are the same on the mbsf and mcd scales. From these anchors, we worked downhole, correlating records on a core-by-core basis. A comparison of the primary mcd and mbsf depth scales (Fig. **F6**) shows that the primary mcd scale is, on average, 18% greater than the mbsf scale. Note that Core 202-1233E-1H was assigned a negative offset (–0.34 m) because its top is not correlative with the other two realizations of the near-surface sediments that we recovered (Sections 202-1233B-1H-1 and 202-1233C-1H-1).

To facilitate the calculation of the mass accumulation rate (MAR), we provide corrected meters composite depth (cmcd) in Tables **T2, T3, T4,** and **T5.** The mcd growth factor for the spliced interval at Site 1233 is 1.18.

LITHOSTRATIGRAPHY

The 136-m-thick hemipelagic sediment sequence probably spanning the last ~170 k.y. was recovered at Site 1233. A single lithologic unit (Unit I) was defined primarily on the basis of visual core description and smear slide examination and is dominated by clay and silty clay with varying amounts of calcareous nannofossils. Siliciclastic components include abundant clay minerals and feldspars and lesser amounts of quartz. Amphiboles, pyroxenes, mica, and opaque minerals are present as minor components throughout Unit I. Biogenic constituents vary in abundance and consist primarily of nannofossils with less abundant diatoms, spicules, silicoflagellates, and foraminifers. The sediments contain authigenic pyrite and monosulfidic minerals appearing as discrete dark spots or as finely dispersed particles, causing a distinct color mottling in the otherwise homogeneous olive-gray to dark olive-gray sediments. Rare interbedded minor lithologies include thin silt and silty sand layers and volcanic ash layers.

F4. OSUS-MS vs. mcd depth for the primary spliced record, p. 24.

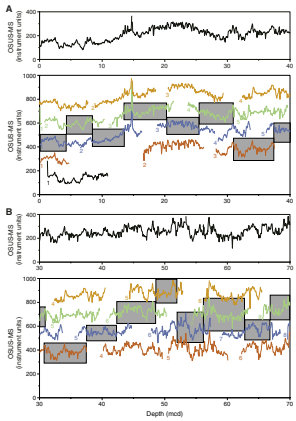

T6. OSUS-MS measurements, Hole 1233A, p. 59.

T7. OSUS-MS measurements, Hole 1233B, p. 60.

T8. OSUS-MS measurements, Hole 1233C, p. 61.

T9. OSUS-MS measurements, Hole 1233D, p. 62.

T10. OSUS-MS measurements, Hole 1233E, p. 63.

F5. Spliced records of L*, NGR, GRA density, and MS, p. 27.

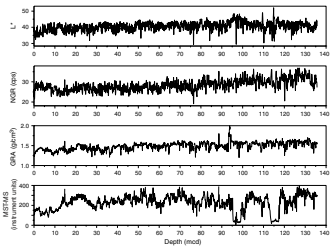

F6. A comparison of mbsf and mcd scales, p. 28.

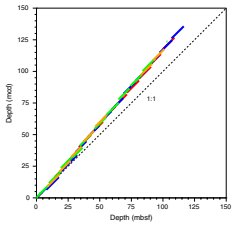

Sediment density generally increases with depth and reflects the effect of mechanical sediment compaction and dewatering. Magnetic susceptibility is lower in the uppermost part (~0–10 mcd) of the recovered sequence, increases downhole to ~20 mcd, and shows two low-intensity intervals (~93–98 and ~113–118 mcd) that correspond to higher chroma a* values (Fig. F7).

Except for the rare silt and silty sand layers that may represent distal turbidites, the lithology of sediments at Site 1233 is consistent with undisturbed hemipelagic sedimentation. Above-average sedimentation rates even for upper continental slope settings are likely the result of enhanced fluvial supply of terrigenous material induced by heavy precipitation in the mountainous continental hinterland.

Description of Lithologic Unit

Unit I

Intervals: Core 202-1233A-1H; Cores 202-1233B-1H through 11H; Cores 202-1233C-1H through 13H; Cores 202-1233D-1H through 13H; and Cores 202-1233E-1H through 8H

Depths: Hole 1233A: 2.50–7.53 mbsf (3.7–8.73 mcd); Hole 1233B: 0–109.59 mbsf (0.06–127.24 mcd); Hole 1233C: 0–116.77 mbsf (0–136.06 mcd); Hole 1233D: 0–112.78 mbsf (0–133.61 mcd); and Hole 1234E: 0–101.27 mbsf (0.34–117.85 mcd)

Age: late Quaternary (~0–170 ka) (see **"Age Model and Mass Accumulation Rates,"** p. 16).

Primarily based on visual core description and smear slide analysis, we distinguished one lithologic unit at Site 1233 (Unit I) (Fig. F7; Table T11). The dominant lithology defining Unit I is primarily homogeneous nannofossil clay, nannofossil silty clay, and nannofossil-bearing silty clay (Fig. F8). Some intervals contain more abundant siliceous microfossils (diatom nannofossil clay, diatom-bearing silty clay, and diatom-nannofossil-bearing clay) and less abundant clayey nannofossil ooze.

Sediments of Unit I display little visual variability and few sedimentary structures (Fig. F8). Thin fissures induced by degassing of the sediment are present throughout the unit. Sediment color ranges from dark olive-gray to dark gray with occasional meter- to decimeter-scale olive-gray to gray intervals. Color changes are subtle and gradational. Upon opening, most cores display abundant black spots and mottles along the surface (Fig. F9), originating from disseminated monosulfides that fade during the core processing time (1–1.5 hr). Bioturbation is rarely visible, probably because of the homogeneous lithology. Some cores contain randomly oriented isolated macroscopic shell fragments.

The siliciclastic fraction within the major lithology lacks sand. Silt contents vary from ~10% to 30% without any remarkable downhole trend (Fig. F10). Silt-sized siliciclastic components are dominated by feldspar (predominantly plagioclase) followed by quartz. Overall, the quartz/feldspar ratio decreases slightly downhole (Fig. F10). Amphiboles, pyroxenes, micas, and opaque minerals are present in variable minor amounts. Small amounts of volcanic glass, partly altered to palagonite, as well as authigenic monosulfides and pyrite are ubiquitous. Primarily, finely dispersed pyrite is present and occasionally is concentrated as framboids in biogenic material such as diatoms and foraminifers.

F7. Lithostratigraphic summary, p. 29.

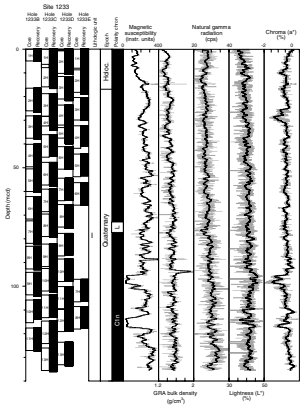

T11. Lithologic Unit I, p. 64.

F8. Major lithology, p. 30.

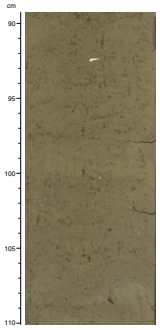

F9. Black mottled disseminated sulfide interval, p. 31.

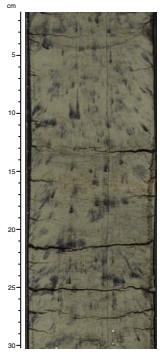

F10. Siliciclastic and authigenic components vs. magnetic susceptibility, p. 32.

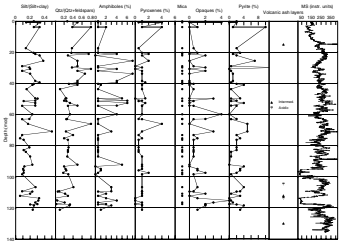

From ~0 to 40 mcd, biogenic components are fairly constant and are dominated by nannofossils and smaller amounts of foraminifers (Fig. F11). Downhole, the proportion of biogenic components is lower and more variable with an increased abundance of siliceous microfossils (predominantly diatoms, minor spicules, radiolarians, and silicoflagellates). Two biogenic-rich intervals appear between ~49 and 53 mcd and ~93 and 98 mcd, with nannofossil abundance exceeding 50%.

Calcium carbonate concentrations vary from ~2 to 10 wt% and roughly parallel the observed changes in the biogenic carbonate fraction (Fig. F11) (see "Geochemistry," p. 13). No smear slides were taken from the first carbonate maximum at ~9–19 mcd, but the lower part of the second interval of increased carbonate contents (~93–100 mcd) correlates with the occurrence of clayey nannofossil oozes and with a distinct minimum in the magnetic susceptibility record (Fig. F11). In contrast, the pronounced second interval of low magnetic susceptibility (~113–118 mcd) is nearly barren of calcareous and siliceous microfossils. Here abundant carbonate concretions suggest strong diagenesis (Fig. F11).

Silt-rich layers and volcanic ash layers are notable minor lithologies. Silt-rich (primarily clayey silt) layers (<1 cm) are present in two intervals from ~9 to 25 mcd and from ~104 to 113 mcd (Table T12). Two thicker (~7–20 cm) fining-upward silty sand layers were observed at ~89 and 93 mcd (Table T12). Volcanic ash layers consisting of up to 95% unaltered volcanic glass are present at ~15 mcd and in the 105- to 130-mcd interval (Fig. F12; Table T12). The five ash layers are of both acidic and intermediate composition (Table T12; Fig. F10). Acidic ash layers are characterized by andesine plagioclase and higher quartz and mica together with low pyroxene contents, whereas ash layers of intermediate composition contain labradorite plagioclase, less quartz, and mica, as well as more abundant pyroxenes.

Magnetic susceptibility is low in the uppermost part (0–10 mcd) of the recovered sequence, increases downhole to ~20 mcd, and fluctuates on a high level from 20 to 140 mcd with two prominent low-intensity intervals (~93–98 and ~113–118 mcd) (Fig. F7).

Color parameter a* indicates that sediments are generally more greenish (Fig. F7) in intervals with low magnetic susceptibility, with the exception of the first 20 mcd, where a* does not agree with magnetic susceptibility. This relationship suggests that reductive dissolution of oxyhydroxides is incomplete above 20 mcd, drawing a* toward red values (a* > 0). L* is constant at ~40%, with slightly lower values in the upper 20 mcd and higher values in some of the low-susceptibility intervals (Fig. F7). In the a*-b* color space, almost all color measurements at Site 1233 plot in the "yellow" domain (Fig. F13). Color parameter b* is weakly correlated with the total organic carbon (TOC) content (r^2 = ~0.5). Assuming a two-component chromatic system, preliminary predictive relationships between reflectance, carbonate, and TOC (Fig. F14) were developed via a multiple linear regression with encouraging results (i.e., r^2 = ~0.7 for carbonate, and r^2 = ~0.8 for TOC).

GRA and moisture and density (MAD) bulk density increase with depth as a consequence of sediment compaction and dewatering, most evidently in the upper 20 mcd. MAD measurements also show this downhole trend (Figs. F7, F15). GRA density data and MAD discrete bulk density measurements show a very good correlation in the upper 7 m of the sequence. Below 7 mcd, however, an offset of ~0.1 to 0.3 g/cm³ between the two sets of density data degrades the correlation. The systematically lower values for GRA bulk density correspond to the lack of

F11. Biogenic components, calcium carbonate, and magnetic susceptibility, p. 33.

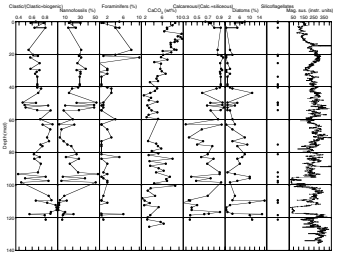

T12. Ash layers, p. 65.

F12. Black ash layer, p. 34.

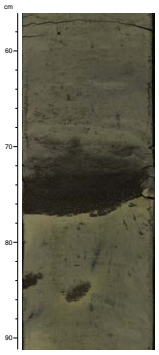

F13. Color measurements, p. 35.

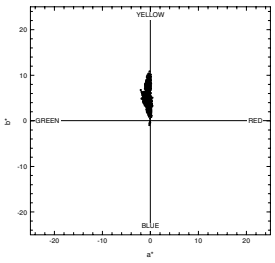

F14. Measured and predicted carbonate and TOC, p. 36.

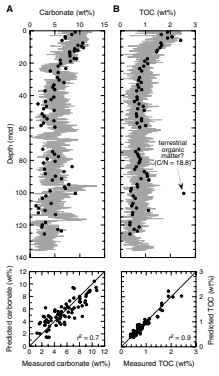

a *P*-wave signal below 10 mcd. Both effects are probably caused by gas expansion that generates voids and fissures within the sediments.

Interpretation and Depositional History

Sediments at Site 1233 are dominated by lithologically homogeneous fine-grained terrigenous material with varying amounts of well-preserved biogenic components (see **"Biostratigraphy,"** p. 9). This lithology suggests that hemipelagic sedimentation predominates, with the exception of rare thin silt and silty sand layers that might represent distal turbidites. This is consistent with the physiographic setting of the site (see **"Introduction,"** p. 1): a small forearc basin on the upper continental slope away from major pathways of turbidity currents, which are rather channelized in this region (Thornburg and Kulm, 1987). The preliminary age model (see **"Age Model and Mass Accumulation Rates,"** p. 16) suggests very high average sedimentation rates in the range of 100 to 170 cm/k.y. for the late glacial and Holocene sequence at Site 1233. Such sedimentation rates are above average, even for upper continental slope settings (approximately a decimeter per thousand years), and can be explained by extremely high terrigenous sediment supply (likely a result of enhanced fluvial discharge in response to heavy continental rainfall in mountainous southern Chile). However, preliminary paleomagnetic evidence suggests that sedimentation rates were lower by a factor of three prior to ~41 ka (~70 mcd) (see **"Age Model and Mass Accumulation Rates,"** p. 16), which may indicate that changes in transport pathways of terrigenous material to Site 1233 and syndepositional sediment focusing within the small forearc basin could have changed through time. Mineral assemblages are consistent with a siliciclastic sediment provenance in both the Andes and the Coastal Range. These results are in agreement with clay mineral and major element composition data from gravity core GeoB 3313-1 from the same location (Lamy et al., 2001). The slight downhole decrease observed in the quartz/feldspar ratios at Site 1233 (Fig. **F10**) might indicate a relative increase in the supply of basaltic to andesitic Andean source rocks vs. predominantly metamorphic Coastal Range source rocks.

Magnetic susceptibility increases, whereas TOC and, to a lesser extent, calcium carbonate contents decrease from the Holocene (~0–12 mcd) to the late glacial, suggesting an enhanced terrigenous dilution of the biogenic component during the late glacial (see **"Geochemistry,"** p. 13). This shift may be a result of increased late glacial continental rainfall as suggested for central Chile (~33°) (Lamy et al., 1999) and/or may be induced by the glacial sea level lowering and resulting higher terrigenous supply to Site 1233.

In the interval from ~93 to 98 mcd, a maximum in calcareous components corresponds to both higher calcium carbonate contents and a pronounced minimum in magnetic susceptibility (Fig. **F11**). However, the second minimum in magnetic susceptibility from ~113 to 118 mcd is associated with very low calcareous microfossil abundance with poor preservation (see **"Biostratigraphy,"** p. 9). Carbonate concretions and the dissolution of fine-grained ferromagnetic minerals (see **"Paleomagnetism,"** p. 11) indicate an early diagenetic overprint during this interval.

Five volcanic ash layers ranging from intermediate to acidic composition were observed at Site 1233. These layers may provide regional stratigraphic markers.

F15. Moisture and density, p. 37.

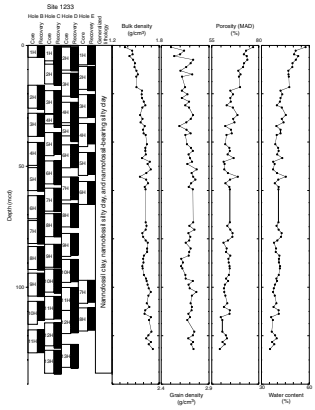

BIOSTRATIGRAPHY

Calcareous nannofossils and diatoms were examined in core catcher samples from Holes 1233A, 1233B, and 1233C and samples from all sections of Hole 1233B. Planktonic and benthic foraminifers were examined in core catcher samples from Hole 1233B. All groups exhibit moderate to high abundances and good preservation (Fig. F16).

Precise age assignments are not possible, although the continued presence of *Emiliania huxleyi* to the bottom of Hole 1233B indicates that the entire sequence is younger than 0.26 Ma.

F16. Calcareous nannofossils and planktonic and benthic foraminifers and diatoms, p. 38.

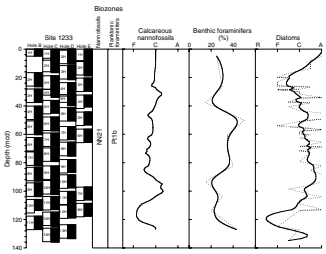

Calcareous Nannofossils

This fossil group is generally abundant and well preserved at the site. The continued presence of *E. huxleyi* to the bottom of Hole 1233B indicates that the entire sequence is younger than 0.26 Ma.

E. huxleyi is generally rare to few and significantly less abundant than *Gephyrocapsa* spp. in the samples examined. This suggests that the *E. huxleyi* acme zone of Thierstein et al. (1977) (0–0.08 Ma) may be missing at the site, or more likely, the zone cannot be applied to this part of the southeast Pacific.

Nannofossil taxa commonly seen at the site include various species of the genus *Gephyrocapsa, E. huxleyi, Calcidiscus leptoporus, Helicosphaera carteri, Braarudosphaera bigelowii, Rhabdosphaera clavigera, Umbilicosphaera sibogae,* and *Umbellosphaera tenuis* (Table T13). The generally low fluctuating abundance of tropical (warm water) taxa, such as *R. clavigera, U. sibogae,* and *U. tenuis,* at the site is believed to indicate variations in the influence of the northward-flowing colder water. This colder water may also be responsible for the generally low abundance of the index species *E. huxleyi.*

T13. Distribution of calcareous nannofossils, p. 66.

Planktonic Foraminifers

Planktonic foraminifers are abundant and relatively well preserved in all samples. The planktonic foraminiferal assemblage includes *Globorotalia truncatulinoides, Globorotalia inflata, Globorotalia scitula, Globorotalia ungulata, Globigerina bulloides, Globigerinita glutinata, Neogloboquadrina dutertrei, Neogloboquadrina pachyderma,* and *Orbulina universa*. This assemblage is present down to 127.05 mcd, indicating the late Pleistocene Subzone Pt1b of Berggren et al. (1995) (Table T5, p. 69, in the "Explanatory Notes" chapter). The composition of the assemblage generally reflects temperate transitional climatic conditions.

Benthic Foraminifers

Benthic foraminifers are generally abundant (representing between 15% and 50% of the total foraminiferal assemblage) and well preserved, although a small proportion of tests are pyritized. For a preliminary assessment of assemblage composition and variability downhole, ~200 specimens from the >150-µm fraction were picked from each core catcher sample and mounted onto slides prior to identification and counting. A total of 44 taxa were identified (Table T14). Common species are *Bulimina marginata, Cassidulina teretis, Chilostomella ovoidea, Ehrenbergina serrata, Eubuliminella exilis, Nonionella auris, Globobulimina pyrula, Globobulimina affinis, Hoeglundina elegans, Melonis affinis, Plan-*

T14. Distribution of foraminifers, p. 68.

ulina wuellerstorfi, Praeglobobulimina spinescens, Pullenia bulloides, Pullenia quinqueloba, Pyrgo serrata, Rutherfordoides mexicanus, Trifarina tricarinata, and *Uvigerina peregrina*.

This upper bathyal assemblage is characteristic of environments receiving an enhanced carbon flux at the seafloor. Many of the species found at Site 1233 are present in assemblages from upwelling regions (e.g., off Pakistan [Maas, 2000; W. Kuhnt and A. Thies, unpubl. data] and off Peru [Oberhänsli et al., 1990; Andresen, 1995]). Oxygen is often depleted in these environments, and distinctive downslope foraminiferal successions are observed that are related to the ambient oxygen and carbon-flux gradients (Jannink et al., 1998; W. Kuhnt and A. Thies, unpubl. data). Species with a high tolerance to oxygen depletion (*B. marginata, C. ovoidea, E. exilis, G. pyrula, G. affinis,* and *P. spinescens*) provide useful indicators for seafloor oxygenation. At Site 1233, their highest abundance in Samples 202-1233-1H-CC, 2H-CC, 4H-CC, 5H-CC, 6H-CC, 7H-CC, and 10H-CC indicates relatively intense dysoxia at the seafloor during sediment deposition. The species *C. teretis* and *U. peregrina* thrive when food is abundant but require higher oxygenation levels. These species show higher abundance in Samples 202-1233-3H-CC, 8H-CC, 9H-CC, and 11H-CC, reflecting more oxic conditions.

Diatoms

Diatom abundance is generally high, and assemblages are moderately to well preserved in both the core catcher samples of Holes 1233B and 1233C and the split-core samples from Hole 1233B. Silicoflagellates, radiolarians, ebridians, sponge spicules, and phytoliths are also observed in most samples.

The major constituents of the flora are taxa typical from intermittent upwelling conditions, such as *Chaetoceros* spores, bristles and vegetative cells, and *Thalassiosira* species (Schuette, 1980; Abrantes 1988; Schrader and Sorknes, 1990; Abrantes and Moita, 1999). *Delphineis* sp., *Pseudonitzschia* sp., and *Thalassionema nitzschioides* are secondary components of the flora (Table **T15**).

T15. Distribution of diatoms, p. 70.

Pelagic warm water–related species, such as *Azpetia nodulifer, Coscinodiscus radiatus,* and *Nitzschia marina,* are found in a few levels and more consistently from Samples 202-1233B-8H-2, 40 cm, through 9H-CC; at 10H-2, 40 cm; and from 8H-CC through 10H-CC. Pelagic cold water–related forms, such as *Actinocyclus curvatulus* and the *Rhizosolenia hebetata* group, were present at the following levels: Samples 202-1233B-2H-3, 40 cm, through 2H-7, 40 cm; 5H-5, 40 cm, through 5H-7, 40 cm; 6H-1, 40 cm, through 6H-5, 40 cm; 8H-2, 40 cm, through 8H-4, 40 cm; 10H-2, 40 cm; 10H-4, 40 cm; 2H-CC; and 7H-CC.

Occasionally, floras are enriched in heavily silicified neritic forms, such as *Actinoptychus senarius, Stephanopyxis turris*. Freshwater diatoms, mainly *Aulacoseira granulata,* are also present in low abundance (trace/rare) throughout the core but more consistently between Sections 202-1233B-6H-CC and 11H-CC (57–113 mcd). Marine benthic forms are found sporadically in the uppermost five cores and more consistently between Sections 202-1233B-6H-CC and 11H-CC (57–113 mcd), indicating some redeposition.

Aside from the presence of *Fragilariopsis doliolus* in Sample 202-1233B-9H-CC, which assigns the core to the Quaternary, no other biostratigraphically useful marker species are observed.

PALEOMAGNETISM

Natural Remanent Magnetization

The natural remanent magnetization (NRM) of archive-half sections were initially measured and then remeasured after alternating-field (AF) demagnetization at selected levels. Sections obviously affected by drilling disturbance were not measured. Core 202-1233A-1H was demagnetized at peak fields of 10, 15, and 20 mT. Cores 202-1233B-1H through 3H were demagnetized at 15 and 20 mT. Cores 202-1233B-4H through 11H were demagnetized at 20 and 25 mT. All other cores (202-1233C-1H through 13H, 202-1233D-1H through 13H, and 202-1233E-1H through 8H) were demagnetized at 25 mT only.

Initial NRM intensities were very high, ranging from 0.2 to 3.25 A/m (Fig. F17). The high NRM intensities are due largely to a drill string magnetic overprint. This overprint, characterized by steep positive inclinations (averaging +59° in Hole 1233B), was substantially reduced (typically by 75%) by demagnetization at peak AF fields as low as 10 mT. NRM intensities, though substantially reduced, were still quite strong (averaging near 0.1 A/m) after 25-mT AF demagnetization. A few intervals that will be discussed below had much lower intensities ($\approx 1 \times 10^{-3}$ A/m). AF demagnetized inclinations (20 or 25 mT), aside from a few intervals, averaged approximately –52° (Fig. F18). This value is close to the expected inclination for an axial geocentric dipole (–59°) at this site latitude (~40°S) and is an indicator that most of the drill string overprint was removed by 25-mT AF demagnetization. Declinations demagnetized at 25 mT also appear to remove the drill string overprint, whereas prior to demagnetization declinations were biased toward 0° or 360°, which is also consistent with a drill string overprint.

The strength of the NRM intensity is probably related to two factors. First, these sediments are composed of homogenous fine-grained terrigenous material of an Andean and Coastal Range provenance with minor biogenic components (see "Lithostratigraphy," p. 5) that contains abundant detrital Fe oxides. Second, prior to demagnetization, the magnetic field imparted by the drilling process results in a strong ubiquitous magnetic overprint. In most instances at Site 1233, this overprint is removed. However, for some cores, the drilling overprint is much larger (higher NRM intensity prior to demagnetization) and incompletely removed even after demagnetization (Fig. F18). This harder overprint is present during times when the APCT tool was used (see Lund et al., this volume). It is thought that this larger and harder overprint results from the longer time that the core barrel sits in the mud when this tool is being used.

Directional Variability

Figure F18 displays the paleomagnetic field directions for Holes 1233B, 1233C, 1233D, and 1233E after AF demagnetization at 25 mT. For the upper few cores the high positive inclinations associated with the drilling overprint are removed by 20 mT. Below that, an additional increment of AF demagnetization (25 mT) is required to recover inclinations closer to expected values (approximately –59°). Negative inclinations dominate the sediments in all cores. Near the bottom of each hole, positive inclinations probably associated with the drilling overprint are still observed in narrow intervals. We were unwilling to de-

F17. NRM before and after AF demagnetization, p. 39.

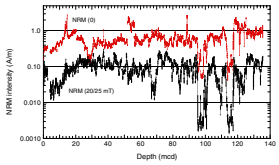

F18. NRM inclination, rotated declination, and intensity after demagnetization, p. 40.

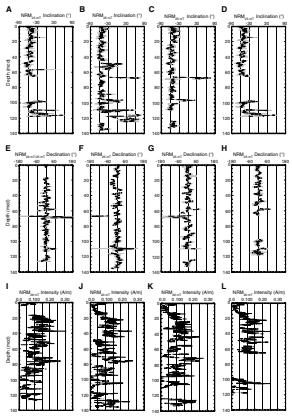

magnetize these sediments further so as to preserve the NRM for shore-based paleomagnetic measurements. The drilling overprint appears to affect inclination more than declination. In Figure F18, the declinations presented have for each core been rotated by assuming their average declination was 0°. Such a rotation is generally consistent with the tensor orientation tool, which was used from the third core down in all holes drilled at this site. The declination variation within individual cores is in most cases consistent with that expected of normal secular variation (<40°). The one exception is an apparent reversal in both inclinations and declinations near 68 mcd. We interpret this to be a magnetic field excursion and discuss it in more detail below. Overall, these data suggest that the sediments at Site 1233 are of normal polarity and Brunhes Chron (0–0.78 Ma) in age.

Shipboard measurements also suggest that a record of paleomagnetic secular variation (PSV) is preserved in Site 1233 sediments (Fig. F18). Initial comparison of the inclination and declination variability from hole to hole shows that this can be correlated (Fig. F19). If shored-based paleomagnetic studies corroborate these measurements and demonstrate that a high-fidelity PSV signal is recorded, then Site 1233 would provide the first pre-Holocene PSV record in the Southern Hemisphere from the eastern South Pacific to South American region. Currently the only published PSV data from this region come from Holocene lakes of Argentina. A summary of PSV data for the last 3000 yr together with historical observations of the geomagnetic field at the same location are shown in Figure F20A (from Lund and Constable, unpubl. data). The paleomagnetic results in Figure F20A have been dated with several bulk radiocarbon dates (calendar year corrected), and the estimated ages are consistent with the historical observations. The PSV variability at Site 1233 is shown in Figure F20B. The chronology for this interval has been determined from several accelerator mass spectrometry (AMS) radiocarbon dates from nearby piston core GeoB3313-1 (Lamy et al., 2001), which have been transferred to Site 1233 based on magnetic susceptibility correlation. The two PSV records in Figure F20 can be correlated, and selected PSV features are noted (D1–D4 and I1–I2). The apparent ages of these features are similar (~±200 yr). This comparison provides an independent assessment of PSV data quality and surface age estimates at Site 1233.

An apparent geomagnetic field excursion is recorded between 65 and 70 mcd in Holes 1233B, 1233C, and 1233D. The NRM (25 mT) shows an interval of steep positive inclinations and declinations ~180° opposed to the other declination values within these cores. One example of this record from Core 202-1233D-8H is displayed in Figure F21. NRM intensities are also low within this interval, suggesting that this may represent one of the Brunhes age geomagnetic excursions. Significant shore-based work will be needed to examine this interval and assess its reliability. Based on estimated sedimentation rates for the surficial sediments described above, the Laschamp geomagnetic field excursion (~41 ka) is the most likely candidate for this excursion. The thickness over which this excursion is recorded in Hole 1233B (~2 m) (Fig. F21) suggests that it may represent one of the highest resolution records of this geomagnetic phenomenon ever observed.

Relative Paleointensity Estimates

Under ideal circumstances, an estimate of the relative changes in past geomagnetic field strength (paleointensity) can be recovered from

F19. Comparison of declinations, Holes 1233B and 1233D, p. 42.

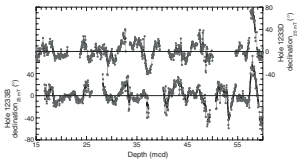

F20. PSV records, p. 43.

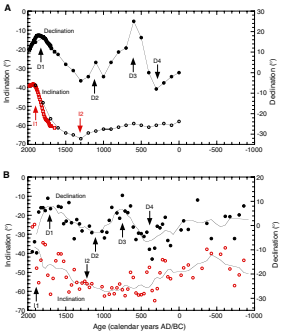

F21. Possible magnetic field excursion, p. 44.

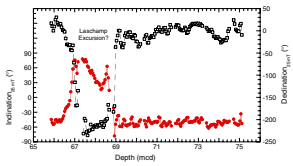

deep-sea sediments. Relative paleointensity can be estimated by normalizing the demagnetized NRM intensity by a proxy that can account for changes in the remanence-carrying magnetic material in the sediment. Under ideal conditions, the residual should reflect changes in geomagnetic field strength. The sediments at Site 1233 appear to record a stable magnetization that is consistent with what is expected for the site latitude and therefore may provide such a record. In order to assess this potential, the shipboard NRM data were normalized with the whole-core MST-derived magnetic susceptibility data. Though far from being an optimal paleointensity proxy, the susceptibility-normalized NRM can provide a first approximation of whether these sediments can be used for this purpose. Results (Fig. F22) show a general reproducibility in the ratio among four holes drilled at Site 1233. Low ratios in the excursional interval (~65–70 mcd) as well as the overall pattern of variability are consistent with what is known about paleointensity record for the last 150 k.y. Extremely low values at 95.5–99 mcd and 113.5–116 mcd may reflect early sediment diagenesis (see below) and must be considered with caution.

Site 1233 is generally characterized by high values of both parameters, presumably due to the high concentration of detrital magnetic grains in this siliciclastic-rich sediment. However, within two intervals (95.5–99 and 113.5–116 mcd) in the lower part of the record, magnetic susceptibility drops by an order of magnitude, from ~250 to ~35 instrument units, and NRM intensities by almost two orders of magnitude, from ~0.1 A/m to 2×10^{-3} A/m (Fig. F23). The larger drop in NRM intensity relative to susceptibility suggests that the finer-grained remanence-carrying part of the magnetic fraction has been preferentially reduced and/or dissolved to nonferromagnetic phases relative to the coarser-grained component. The fact that this does not always occur suggests time-dependent sediment diagenesis that may reflect stronger reducing conditions. The anomalous magnetic directions within these intervals (Fig. F18) may be at least partially due to these conditions. Anomalously low NRM and MS values were not observed in the interval recording the excursional magnetic directions at ~65–67 mcd.

F22. Demagnetized and normalized NRM intensity, p. 45.

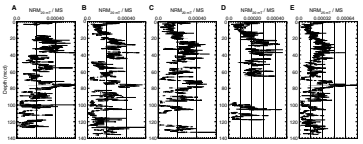

F23. MS vs. demagnetized NRM intensity, p. 46.

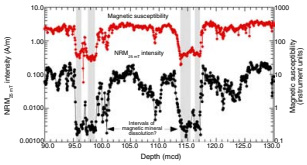

GEOCHEMISTRY

Sediment Gases

Concentrations of headspace and vacutainer gases were routinely monitored in Hole 1233B sediments according to shipboard safety and pollution prevention considerations. Low methane concentrations were first detected in the shallowest headspace gas sample at 1.5 mcd (Table T16; Fig. F24). Methane concentrations increased by 21.1 mcd, and vacutainer samples had high methane concentrations (≥95 vol%) from 23.1 to 121.8 mcd. No significant amounts of higher molecular weight hydrocarbons were observed (Table T16).

High methane concentrations, low concentrations of higher molecular weight hydrocarbons, and the resulting high C_1/C_2 ratio (Fig. F24) indicate that the methane originates from in situ fermentation (methanogenesis) of sedimentary organic matter. A biogenic origin for methane is supported by the disappearance of interstitial dissolved sulfate below 2 mcd. The presence of interstitial sulfate inhibits methanogenesis in marine sediments (Claypool and Kvenvolden, 1983).

T16. Headspace and vacutainer gas concentrations and C_1/C_2 ratio, p. 71.

F24. Headspace and vacutainer methane and C_1/C_2 vs. depth, p. 47.

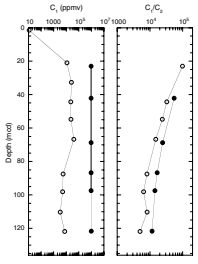

Interstitial Water Geochemistry

We collected 14 interstitial water samples from Site 1233, 11 from Hole 1233B and 3 from Hole 1233C. These are treated as constituting a single mcd profile. Chemical gradients at this site (Table T17) reflect the likely presence of gas hydrates, the influence of organic matter diagenesis by microbially mediated oxidation reactions, a limited degree of biogenic opal dissolution, and the effects of authigenic mineralization reactions on fluid composition.

Chlorinity decreases by >12%, from 561 mM at 1.5 mcd to ~490 mM by 110–120 mcd (Fig. F25). Salinity, measured refractively as total dissolved solids, ranges from 37 to 30, decreasing with increasing depth (Table T17). Sodium concentrations measured by inductively coupled plasma–atomic emission spectrophotometry were typically within <4% of those estimated by charge balance reported here (Table T17). Sodium concentrations decrease by >12% by 110–120 mcd, in accord with the decreases seen in chlorinity and salinity.

The decreasing chlorinity gradient at Site 1233 is significantly larger than the gradients observed at the deeper-water, mid-slope Peru margin basin sites drilled during Leg 112 (Sites 682, 683, 685, and 688; Suess, von Huene, et al., 1988). The decomposition of gas hydrates in Site 1233 sediments can explain the observed chloride gradient in interstitial water as a result of dilution, either through in situ decomposition at depth in the sediment column or during sediment recovery. The second process is usually evident from spiky, low values in chloride profiles, not observed here. Other possible explanations for the chloride gradient include mineral dehydration reactions at depth, clay membrane ion filtration reactions at depth, and advection of fresher fluid at depth (Kastner et al., 1990).

Organic matter diagenesis, driven by microbial oxidation reactions, dominates many of the interstitial water profiles. The relatively low organic carbon contents are apparently counterbalanced by high total sedimentation rates to result in pronounced depth variations in interstitial water chemistry, as typically observed in more organic carbon–rich, continental margin settings. Sulfate concentration at 1.5 mcd is 12.5 mM, already substantially lower than typical seawater values of 29 mM, and all deeper samples have sulfate concentrations below the detection limit (~0.5 mM). Organic matter decomposition by sulfate reduction and methanogenesis drives large increases in alkalinity, which increases to peak values of >60 mM from 21.0 to 44.3 mcd then decreases to 30 mM at 121.8 mcd.

The profiles of the reduced forms of the secondary oxidants manganese and iron show variations with depth, although not simply related to that of sulfate. Dissolved manganese concentrations average <3 µM, with small maxima at 11.0 mcd and from 76.9 to 87.5 mcd. Dissolved iron concentrations rapidly increase to 53 µM at 11.0 mcd, decrease sharply to <15 µM by 21.0 mcd, and then decrease gradually with increasing depth.

Organic matter decomposition generates increases in phosphate and ammonium in interstitial water. Phosphate concentrations are >100 µM throughout, with values >210 µM from 11.0 to 66.7 mcd. Ammonium concentrations increase from 1.7 mM at 1.5 mcd to values >5 mM from 11.0 to 76.9 mcd, with decreasing values to 3.1 mM at 121.8 mcd. The maximum in ammonium concentration is broader and deeper than the phosphate maxima.

T17. Interstitial water geochemical data, p. 72.

F25. Interstitial water geochemical data, p. 48.

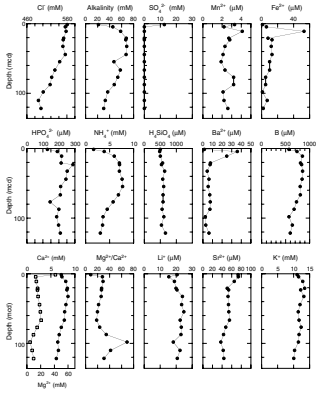

Dissolved silicate concentrations average ~570 µM (Fig. F25), indicating that the interstitial waters are not at saturation with respect to biogenic opal. This may reflect the limited amount of biogenic opal available for dissolution or other controls on opal solubility in these sediments. Barium concentrations increase to a sharp maximum of 36 µM at 4.5 mcd, coincident with the disappearance of dissolved sulfate, and are <10 µM from 21.0 mcd to total depth. The dissolution of barite, driven by the decrease in dissolved sulfate, is consistent with the observed profiles. Boron concentrations increase to values >800 µM from 11.0 to 66.7 mcd then generally decrease with increasing depth to values at low as ~600 µM. The resemblance of the boron and ammonium profiles indicates that adsorption/desorption reactions may influence the boron profile.

Calcium concentrations decrease sharply from 6 mM at 1.5 mcd to values <2 mM from 4.5 to 11.0 mcd, then increase to ~3 mM at 66.7 mcd, followed by a decrease with increasing depth to a minimum of 0.7 mM at 98.1 mcd. Magnesium concentrations increase to >55 mM from 11.0 to 54.7 mcd, then decrease to 43 mM at 121.8 mcd. The very strong decrease in calcium by 4.5 mcd is consistent with authigenic mineralization reactions driven by the alkalinity increase. Increasing magnesium/calcium ratios with the calcium decrease indicate that calcite precipitation is the most likely reaction taking place. Magnesium/calcium ratios are >25 from 4.5 to 32.6 mcd, decreasing to only as low as 19, before increasing to a sharp maximum of 69 at 98.1 mcd coincident with the calcium minimum. Lithium concentrations first decrease sharply then generally increase with increasing depth. Strontium concentrations generally decrease slightly with increasing depth, and potassium concentrations increase to >12 mM from 11.0 to 44.3 mcd then decrease with increasing depth (Fig. F25).

Sedimentary Inorganic Carbon and Organic Carbon, Nitrogen, and Sulfur Concentrations

Inorganic carbon (IC), total carbon (TC), and total nitrogen (TN) concentrations were determined on sediment samples from Holes 1233A, 1233C, and 1233E (Table T18). Organic matter carbon/nitrogen ratios were employed to characterize the organic matter.

The calcium carbonate profile reflects the overall uniformity of the sedimentary section at this site (Fig. F26; also see "Lithostratigraphy," p. 5). Calcium carbonate concentrations are low throughout the record, ranging between 1.2 and 10.8 wt% (average = 5.4 wt%). Calcium carbonate concentrations are higher in the uppermost 30 mcd, with lower concentrations in the intervals from 30 to 60 mcd and from 102 to 126 mcd. Stronger-amplitude variations of 3–6 wt% mark the interval from 80 to 105 mcd. The highest calcium carbonate concentrations correspond to observations of increased abundance of calcareous nannofossils and foraminifers (see "Lithostratigraphy," p. 5).

TOC concentrations range between 0.4 and 2.4 wt% (average = 0.9 wt%) (Table T18). TOC variations are similar to those of calcium carbonate (Fig. F26). TOC concentrations decrease from ~2 wt% at the top to ~0.5 wt% at 30 mcd. At greater depths, the TOC concentrations and amplitude fluctuations remain low. TN concentrations have similar trends.

TOC/TN ratios are between 5 and 9 (average = 5.9) (Table T18), indicating a predominance of marine organic matter throughout the record (Bordovskiy, 1965; Emerson and Hedges, 1988; Meyers, 1997). In addi-

T18. IC, $CaCO_3$, TC, TOC, and TN concentrations and TOC/TN ratio, p. 73.

F26. Calcium carbonate, TOC, and TN vs. depth, p. 49.

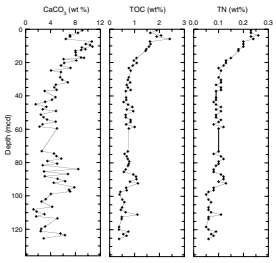

tion, the lack of a significant correlation between TOC/TN ratios and decreases in TOC contents indicates that the TOC decrease in the upper 30 mcd is not induced by diagenesis of the organic matter (Fig. F27). This decrease in TOC and, to a lesser extent, in calcium carbonate concentrations may reflect a decrease in export productivity and/or a dilution effect caused by an increased supply of siliciclastic material (see "Lithostratigraphy," p. 5).

F27. TOC/TN vs. TOC, p. 50.

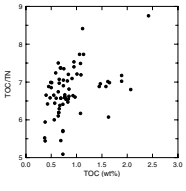

AGE MODEL AND MASS ACCUMULATION RATES

A 136.1-mcd thick (116.8 mbsf) late Pleistocene (~170 ka) hemipelagic sediment sequence was recovered at Site 1233. Age control points for the last 7 k.y. were derived from a nearby sediment record (core GeoB 3313-1; Lamy et al., 2002) that was dated by AMS ^{14}C. For the interval >7 ka, variations in paleomagnetic directions and intensities at Site 1233 could be correlated to dated records elsewhere (Table T19). Linear sedimentation rates (LSRs), MARs, and carbonate MARs were calculated at 10-k.y. intervals (see "Age Models and Mass Accumulation Rates," p. 41, in the "Explanatory Notes" chapter).

T19. Age control points, p. 75.

Age-Depth Model

The late Pleistocene interval recovered at Site 1233 provided no biostratigraphic datum to define an age model. The continued presence of *E. huxleyi* to the bottom of Hole 1233B indicates that the entire sequence is younger than 260 ka. The *E. huxleyi* acme zone (base at 80 ka) was not observed either because of the generally low abundance of the species or, more likely, because the zone cannot be applied to this part of the southeast Pacific (see "Biostratigraphy," p. 9).

The magnetic susceptibility record of the uppermost 9 mcd recovered at Site 1233 could be correlated directly to the magnetic susceptibility of the ^{14}C-dated sediment record of core GeoB 3313-1 (Fig. F28), which justified the transfer of six AMS ^{14}C ages ranging from 0.260 to 7.090 ka to Site 1233 (Table T19). The ^{14}C age of 5.590 ka was not considered as an age control point at Site 1233 because of an uncertain match between the magnetic susceptibility records in this interval.

F28. Correlation of MS between Site 1233 core GeoB 3313-1, p. 51.

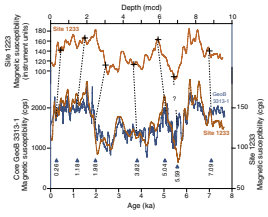

Site 1233 provided an unprecedented high-resolution Southern Hemisphere record of centennial- to millennial-scale variability in paleomagnetic intensities (Fig. F29), which offered the opportunity for developing a preliminary age model. We used the paleointensity record from Site 1089 in the sub-Antarctic South Atlantic (Stoner et al., in press) that was dated by oxygen isotope stratigraphy as a target record for correlation with Site 1233. The Sint-200 paleointensity stack (Guyodo and Valet, 1996) is also shown for reference in Figure F29. To avoid overinterpretation regarding the small-scale variability, we correlated only the large-scale pattern of changes in paleointensity between Sites 1233 and 1089 (Fig. F29). Among them, the most prominent feature in late Pleistocene paleointensity fluctuations of the geomagnetic field is the intensity low associated with the Laschamp Event (41 ka). At Site 1233, the directional record of this event is observed to occur over a 2-m interval between 65 and 70 mcd in Holes 1233B, 1233C, and 1233D (see "Paleomagnetism," p. 11). The correlation of magnetic intensity variations between Sites 1233 and 1089 provided additional age control points for the interval from 41 to 121 ka (Table T19). We chose to add age uncertainties of ±3 k.y. and depth uncertainties of ±2 m to these tie

F29. Geomagnetic paleointensity from Sites 1233 and 1089 and Sint-200, p. 52.

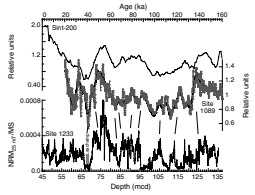

points, which resulted in a conservative straight-line model for depths >75 mcd.

Linear Sedimentation Rates and Mass Accumulation Rates

Average MARs and LSRs are generally very high at Site 1233, ranging from 40 to 150 g/cm²/k.y. and from 40 to 160 cm/k.y., respectively (Fig. F30; Table T20). The lowest average MAR and LSR mark the interval from ~150 to ~50 ka (MIS 5 to 3). The rates increased by a factor of three on average from 50 ka to ~10 ka (marine isotope stage [MIS] 3) and the maximum MAR and LSR values at that time represent a rough estimate for the last glacial maximum (LGM). During the Holocene, the average MAR dropped to one third the LGM level, to ~50 g/cm²/k.y.

Siliciclastic material dominates the late Quaternary sediment at Site 1233 (generally >90 wt%). The total MAR therefore reflects the input of terrigenous material largely derived from the Andes and the Coastal Range provinces (see "Lithostratigraphy," p. 5). The current source is dominated by fluvial input. The late Pleistocene maximum in total MARs between ~50 and 10 ka indicates that this source has been enhanced during the LGM, possibly associated with temporal changes in continental rainfall patterns and/or refocusing of fluvial sediment discharge during glacial sea level lowstand. We cannot exclude the possibility that the tripling of MAR during MISs 2 and 3 is a random event, perhaps driven by a newly formed channel that favored a higher sediment flow to Site 1233.

Carbonate MARs account for only a small portion of the total MAR at Site 1233 but they are the highest carbonate MARs compared to any of the Leg 202 sites. Similarly, TOC MARs are very high (up to ~2 g/m²/yr after 50 ka) even if compared to other high-productivity regions like the upwelling zone offshore northwest Africa and California (1–4 g/m²/yr) (Stein et al., 1989; Lyle et al., 2000). The carbonate MAR increased from the lowest values of 1–2 g/cm²/k.y. at ages >50 ka to a maximum of ~10 g/cm²/k.y. at 20–10 ka, and then decreased to half that value, suggesting a significantly reduced productivity during the late Holocene. TOC accumulation parallels this trend. This is consistent with the findings of Hebbeln et al. (2002), who reconstructed the paleoproductivity off central Chile based on records of TOC, carbonate, and biogenic opal accumulation rates for the last 33 k.y. and found maximum values for the LGM and lower values for the late Holocene. Studies of productivity indicators in surface sediments from the Chile margin (Hebbeln et al., 2002) and in the Holocene sedimentary record of gravity core GeoB 3313-1 located at Site 1233 (Lamy et al., 2002) suggest that productivity changes off southern Chile are primarily controlled by the inflow of high-nutrient and low-chlorophyll waters of the Antarctic Circumpolar Current supplemented by micronutrients (e.g., iron) derived from the continental detritus. Future studies will address whether or not additional variations in the presently very restricted seasonal upwelling at Site 1233 contributed to the biogenic MAR changes.

F30. Age model, p. 53.

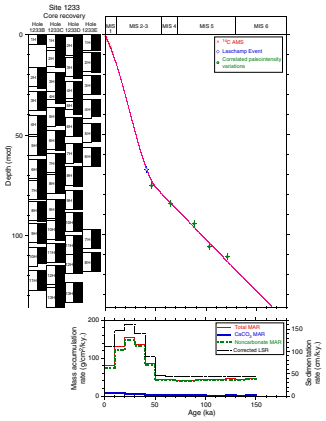

T20. Age-depth model, LSRs, and MARs, p. 76.

REFERENCES

Abrantes, F., 1988. Diatom assemblages as upwelling indicators in surface sediments off Portugal. *Mar. Geol.,* 85:15–39.

Abrantes, F., and Moita, T., 1999. Water column and recent sediment data on diatoms and coccolithophorids, off Portugal, confirm sediment record as a memory of upwelling events. *Oceanol. Acta,* 22:319–336.

Andresen, N., 1995. Veränderlichkeit der benthischen Foraminiferenfauna und des spätglazialen bis holozänen Küstenauftriebes bei 11°S vor Peru [Thesis]. Christian-Albrechts-Universität, Kiel.

Berggren, W.A., Kent, D.V., Swisher, C.C., III, and Aubry, M.-P., 1995. A revised Cenozoic geochronology and chronostratigraphy. *In* Berggren, W.A., Kent, D.V., Aubry, M.-P., and Hardenbol, J. (Eds.), *Geochronology, Time Scales and Global Stratigraphic Correlation*. Spec. Publ.—SEPM, 54:129–212.

Bordovskiy, O.K., 1965. Accumulation and transformation of organic substances in marine sediments, 2. Sources of organic matter in marine basins. *Mar. Geol.,* 3:5–31.

Brandhorst, W., 1971. Condiciones oceanográficas extivales frente a la costa de Chile. *Revista Biologica Marina (Valparaiso),* 14:45–84.

Claypool, G.E., and Kvenvolden, K., 1983. Methane and other hydrocarbons gases in marine sediment. *Annu. Rev. Earth Planet. Sci.,* 11:299–327.

Dettinger, M.D., Battisti, D.S., Garreaud, R.D., McCabe, G.J., Jr., and Blitz, C.M., 2001. Interhemispheric effects of interannual and decadal ENSO-like climate variations on the Americas. *In* Markgraf, V. (Ed.), *Interhemispheric Climate Linkages:* San Diego (Academic Press), 1–16.

Emerson, S., and Hedges, J.I., 1988. Processes controlling the organic carbon content of open ocean sediments. *Paleoceanography,* 3:621–634.

Fonseca, T.R., 1989. An overview of the poleward undercurrent and upwelling along the Chilean coast. *In* Neshyba, S.J., Mooers, C.N.K., Smith, R.L., and Barber. R.T. (Eds.), *Poleward Flows along Eastern Ocean Boundaries:* New York (Springer), 203–228.

Guyodo, Y., and Valet, J.-P., 1996. Relative variations in geomagnetic intensity from sedimentary records: the past 200,000 years. *Earth Planet. Sci. Lett.,* 143:23–36.

Hebbeln, D., and Cruise Participants, 2001. PUCK, report and preliminary results of *R/V Sonne* Cruise 156, Valparaiso (Chile)–Talcahuano (Chile), March 29–May 14, 2001. *Berichte aus dem Fachbereich Geowissenschaften der Universität Bremen,* 182: Bremen, Germany (Geowissenschaften der Universität Bremen), 1–195.

Hebbeln, D., Marchant, M., and Wefer, G., 2002. Paleoproductivity in the southern Peru-Chile Current through the last 33,000 years. *Mar. Geol.,* 186:487–504.

Hebbeln, D., Wefer, G., Baltazar, M., Beese, D., Bendtsen, J., Butzin, M., Daneri, G., Dellarossa, V., Diekamp, V., Dittert, N., Donner, B., Giese, M., Glud, R., Gundersen, J., Haese, R., and Hensen, C., 1995. Report and preliminary results of SONNE-Cruise SO 102, Valparaiso–Valparaiso, 95. *Berichte aus dem Fachbereich Geowissenschaften der Universität Bremen,* 68: Bremen, Germany (Geowissenschaften der Universität Bremen), 1–134.

Jannink, N.T., Zachariasse, W.J., and Van der Zwaan, G.J., 1998. Living (Rose Bengal stained) benthic foraminifers from the Pakistan continental margin (northern Arabian Sea). *Deep-Sea Res. I,* 45:1438–1513.

Kastner, M., Elderfield, H., Martin, J.B., Suess, E., Kvenvolden, K.A., and Garrison, R.E., 1990. Diagenesis and interstitial-water chemistry at the Peruvian continental margin—major constituents and strontium isotopes. *In* Suess, E., von Huene, R., et al., *Proc. ODP, Sci. Results,* 112: College Station, TX (Ocean Drilling Program), 413–440.

Lamy, F., Hebbeln, D., Röhl, U., and Wefer, G., 2001. Holocene rainfall variability in southern Chile: a marine record of latitudinal shifts of the southern Westerlies. *Earth Planet. Sci. Lett.,* 185:369–382.

Lamy, F., Hebbeln, D., and Wefer, G., 1999. High-resolution marine record of climatic change in mid-latitude Chile during the last 28,000 years based on terrigenous sediment parameters. *Quat. Res.,* 51:83–93.

Lamy, F., Rühlemann, C., Hebbeln, D., and Wefer, G., 2002. High- and low-latitude control on the position of the southern Peru-Chile current during the Holocene. *Paleoceanography,* 1710.1029/2001PA000727.

Lyle, M., Mix, A., Ravelo, C., Andreasen, D., Heusser, L., and Olivarez, A., 2000. Millennial-scale $CaCO_3$ and C_{org} events along the northern and central California margins: stratigraphy and origins. *In* Lyle, M., Koizumi, I., Richter, C., and Moore, T.C., Jr. (Eds.), *Proc. ODP, Sci. Results,* 167: College Station, TX (Ocean Drilling Program), 163–182.

Maas, M., 2000. Verteilung lebendgefärbter benthischer Foraminiferen in einer intensivierten Sauerstoffminimumzone, Indo-Pakistanischer Kontinentalrand, nördliches Arabisches Meer. *Meyniana,* 52:101–129.

Meyers, P.A., 1997. Organic geochemical proxies of paleoceanographic, paleolimnologic, and paleoclimatic proxies, *Org. Geochem.,* 27:213–250.

Oberhänsli, H., Heinze, P., Diester-Haass, L., and Wefer, G., 1990. Upwelling off Peru during the last 430,000 yr and its relationship to the bottom-water environment, as deduced from coarse grain-size distributions and analyses of benthic foraminifers at Holes 679D, 680B, and 681B, Leg 112. *In* Suess, E., von Huene, R., et al., *Proc. ODP, Sci. Results,* 112: College Station, TX (Ocean Drilling Program), 369–390.

Ocean Climate Laboratory, 1999. *World Ocean Atlas 1998 (WOA98)* [CD-ROM]. Available from: National Climatic Data Center, Asheville NC 28801-5001, USA.

Schrader, H., and Sorknes, R., 1990. Spatial and temporal variation of Peruvian coastal upwelling during the latest Quaternary. *In* Suess, E., von Huene, R., et al., *Proc. ODP, Sci. Results,* 112: College Station, TX (Ocean Drilling Program), 391–406.

Schuette, G., 1980. Recent marine diatom taphocoenoses off Peru and off southwest Africa: reflection of coastal upwelling [Ph.D. dissert.]. Oregon State Univ.

Stein, R., ten Haven, H.L., Littke, R., Rullkotter, J., and Welte, D.H., 1989. Accumulation of marine and terrigenous organic carbon at upwelling Site 658 and nonupwelling Site 657 and 659: implications for the reconstruction of paleoenvironments in the eastern subtropical Atlantic through late Cenozoic times. *In* Ruddiman, W., Sarnthein, M., et al. (Eds), *Proc. ODP, Sci. Results,* 108: College Station, TX (Ocean Drilling Program), 361–385.

Stoner, J.S., Channell, J.E.T., Hodell, D.A., and Charles, C.D., in press. A 580 kyr paleomagnetic record from the sub-Antarctic South Atlantic (ODP Site 1089). *J. Geophys. Res.*

Strub, P.T., Mesias, J.M., Montecino, V., Rutllant, J., and Salinas, S., 1998. Coastal ocean circulation off western South America. *In* Robinson, A.R., and Brink, K.H. (Eds.), *The Sea* (Vol. 11): *Coastal Oceans:* New York (Wiley), 273–313.

Suess, E., von Huene, R., et al., 1988. *Proc. ODP, Init. Repts.,* 112: College Station, TX (Ocean Drilling Program).

Thierstein, H.R., Geitzenauer, K., Molfino, B., and Shackleton, N.J., 1977. Global synchroneity of late Quaternary coccolith datum levels: validation by oxygen isotopes. *Geology,* 5:400–404.

Thornburg, T.M., and Kulm, L.D., 1987. Sedimentation in the Chile Trench: depositional morphologies, lithofacies, and stratigraphy. *Geol. Soc. Am. Bull.,* 98:33–52.

Figure F1. A, B. Digital Parasound profile at Site 1233 (Hebbeln et al., 1995). Note in B the possibility of a hiatus near 65 mbsf. (Continued on next page.)

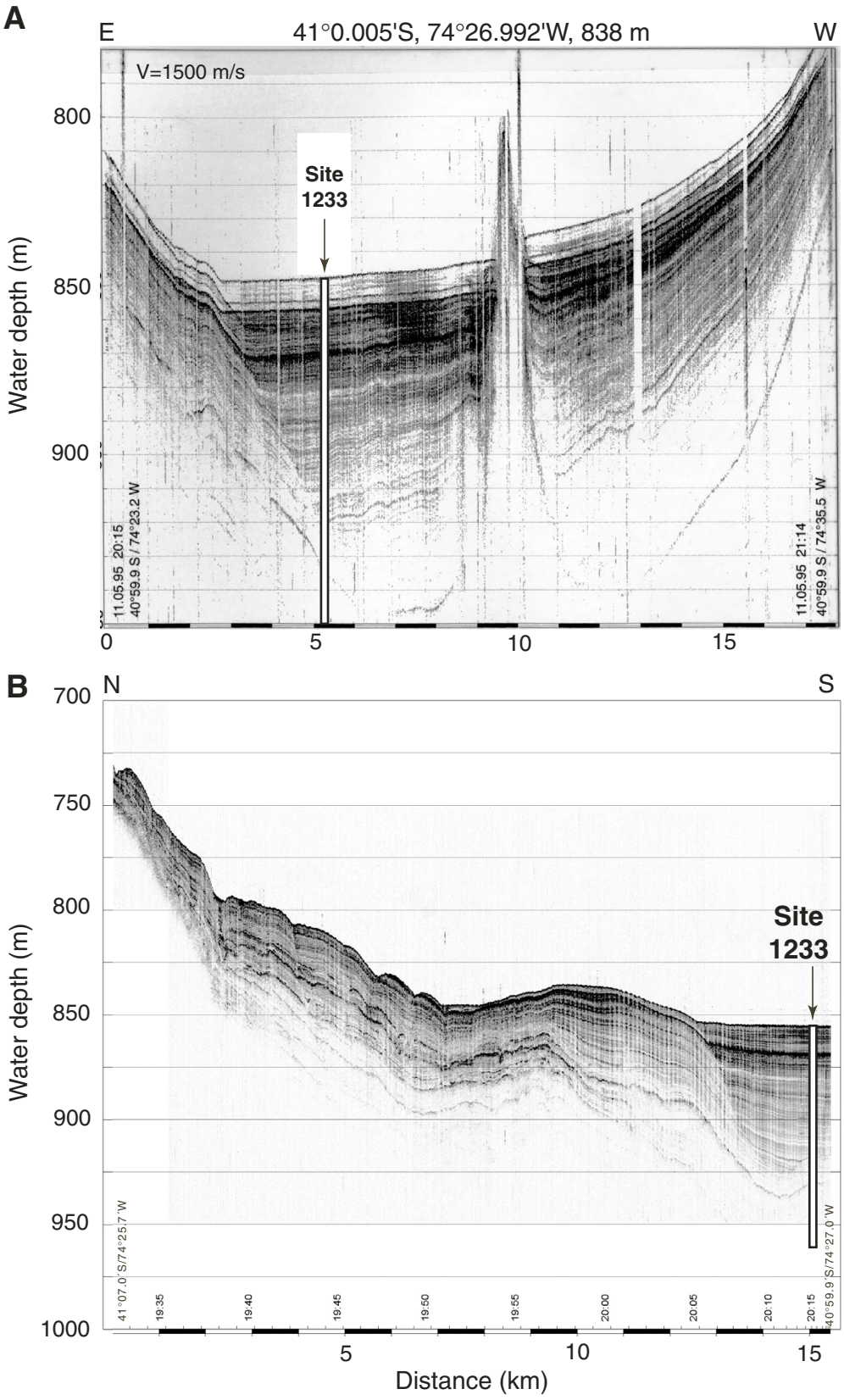

Figure F1 (continued). C. Analog 3.5-kHz profile acquired during approach to Site 1233. Significant reflectors (R1 to R8) are noted, with their apparent depths calculated assuming a sound velocity of 1500 m/s.

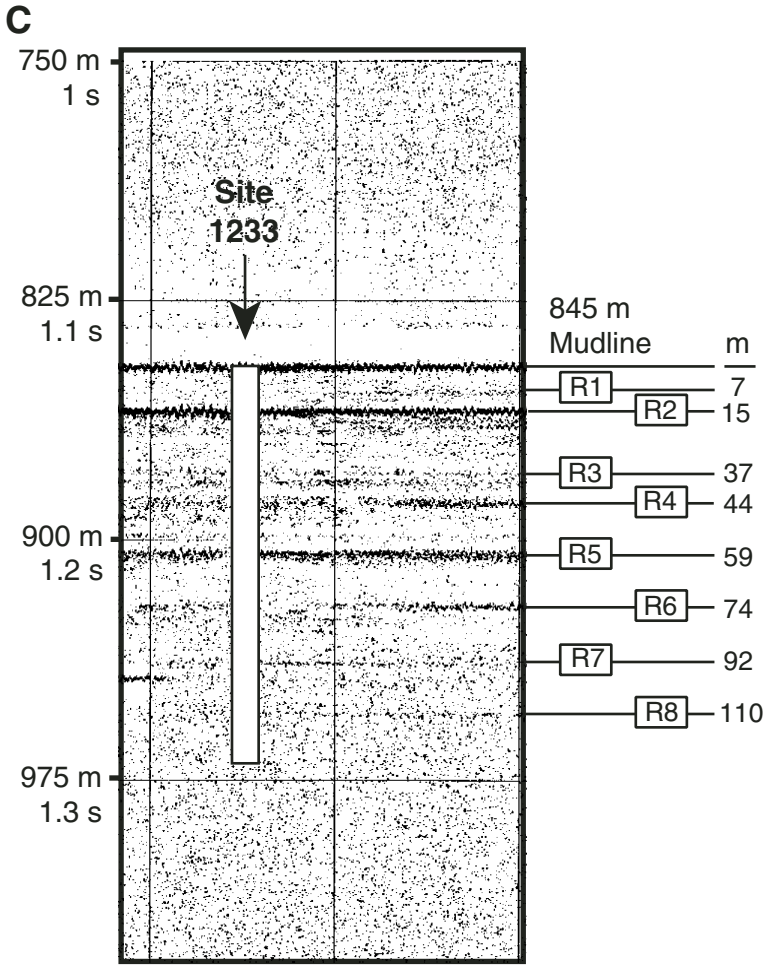

Figure F2. Locations of Site 1232–1235 and oceanographic features off southern and central Chile (ACC = Antarctic Circumpolar Current, PCC = Peru-Chile Current, PCCC = Peru-Chile Countercurrent, CC = Chile Coastal Current, CFW = Chilean Fjord Water) after Strub et al. (1998) and Lamy et al. (2002). **A.** Modern mean annual sea-surface temperatures (SSTs) (contours are in degrees Celsius, after Ocean Climate Laboratory, 1999; dashed isotherms are extrapolated). **B.** Modern sea-surface salinities (SSSs) measured during the *Marchile* cruise in February to March 1960 (Brandhorst, 1971).

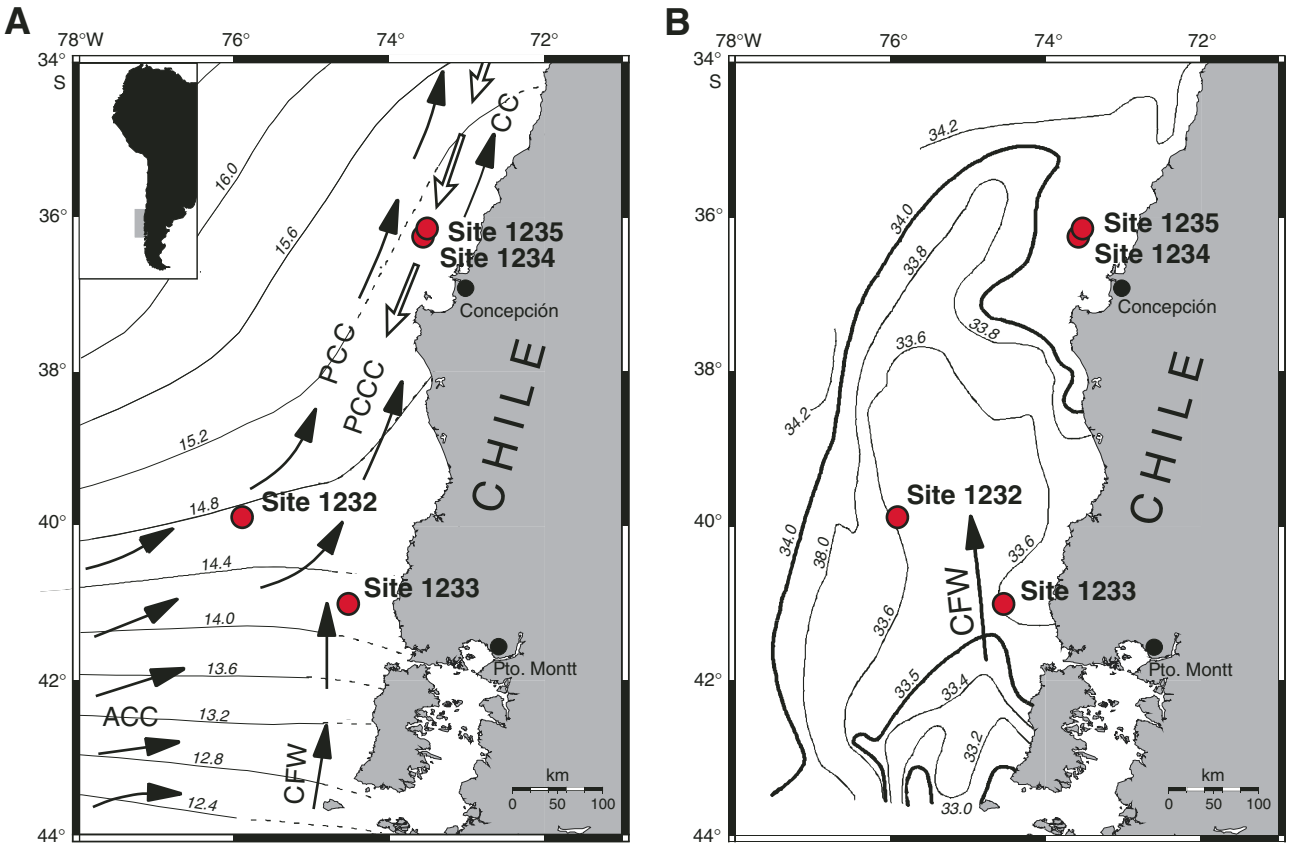

Figure F3. North-south cross section of water masses, characterized by dissolved oxygen concentrations in the southeast Pacific (Ocean Climate Laboratory, 1999). Southward-spreading middepth waters (PCW = Pacific Central Water) are characterized by relatively low oxygen and salinity and high nutrients. Northward-spreading Antarctic Intermediate Water (AAIW), ~400–1000 m depth, is high in oxygen but is low in both salinity and nutrients. The Gunther Undercurrent (GUC) flows southward between 100 and 400 m water depth and is characterized by relatively low oxygen and high nutrients. Vertical tails on site locations indicate likely changes in position relative to water masses associated with ~130-m sea level lowering at the Last Glacial Maximum.

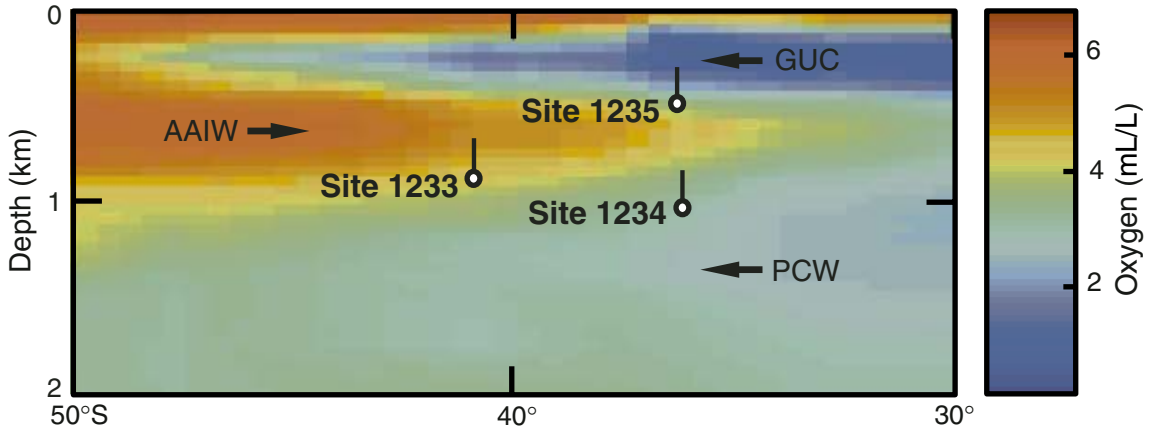

Figure F4. OSU Fast Track magnetic susceptibility data (OSUS-MS) vs. mcd for the primary spliced record and Holes 1233A through 1233E. Gray boxes indicate the portions of cores that are in the primary splice. **A.** 0–40 mcd. **B.** 30–70 mcd. (Continued on next two pages.)

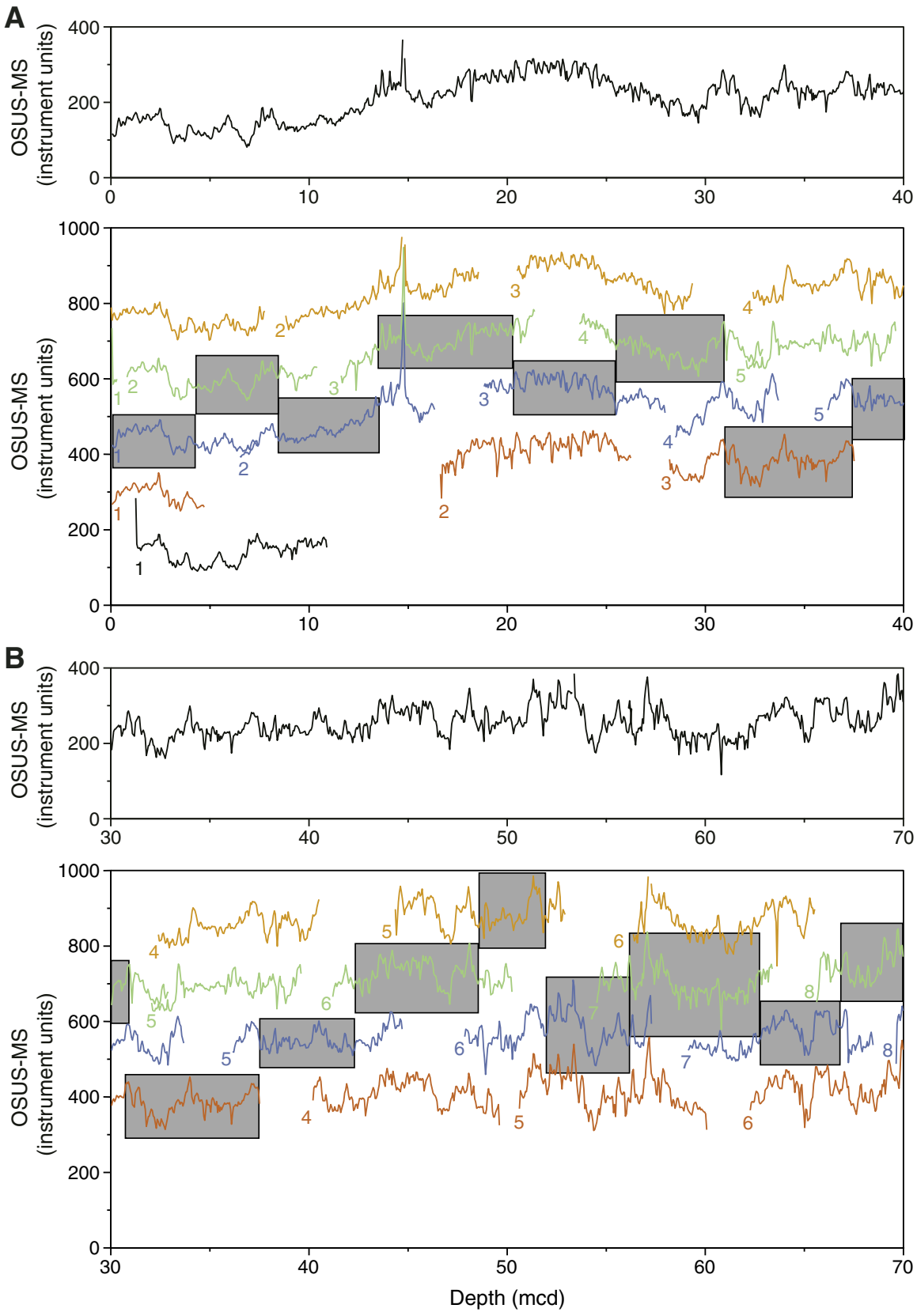

Figure F4 (continued). C. 60–100 mcd. D. 90–130 mcd.

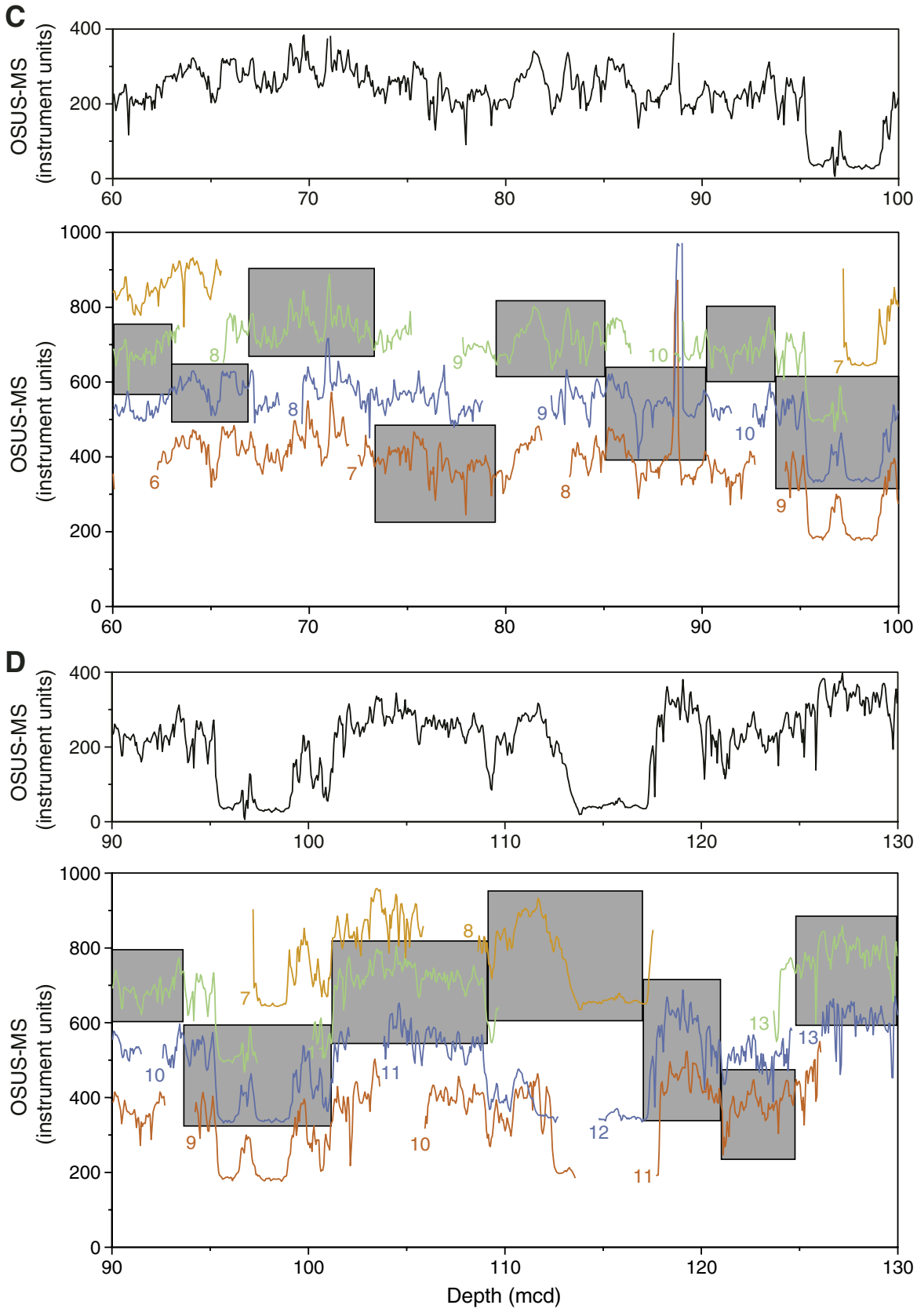

Figure F4 (continued). E. 120–160 mcd.

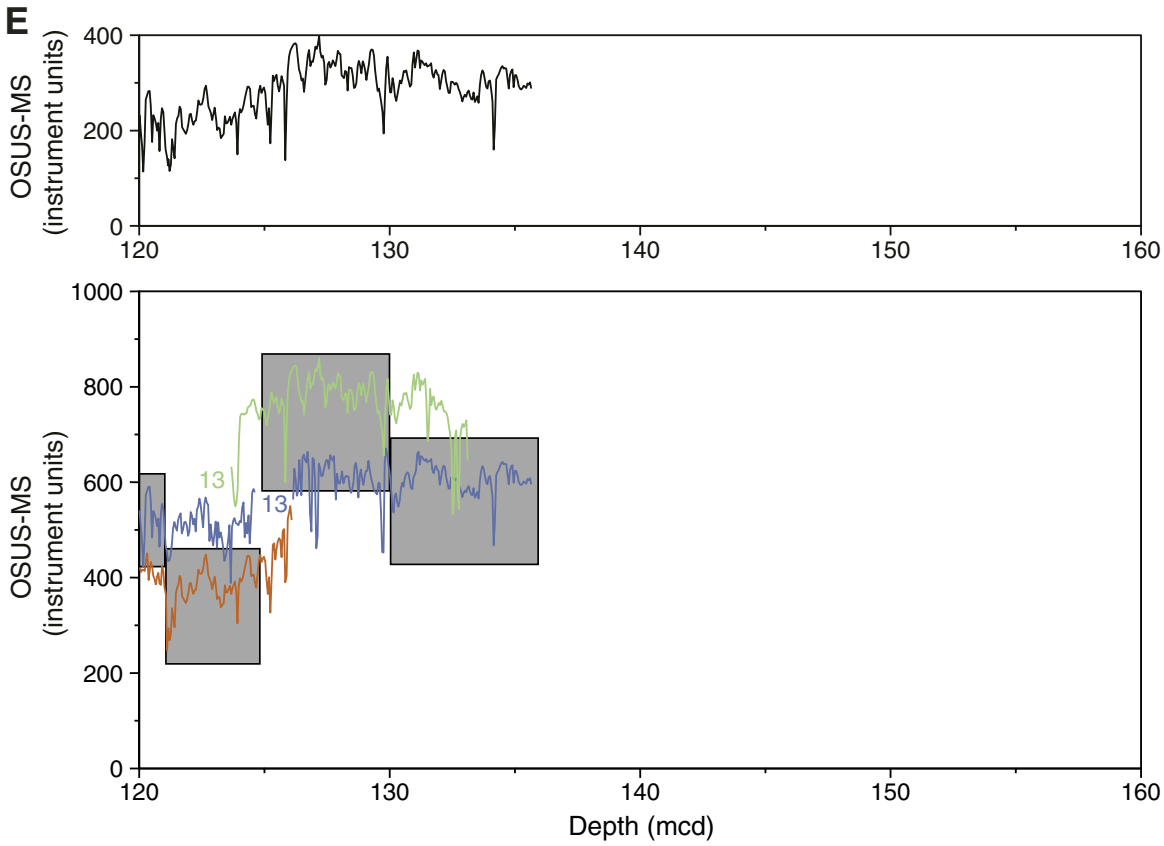

Figure F5. Records of reflectance (L*), NGR, GRA density, and MST-MS data from Site 1233 constructed using the primary splice.

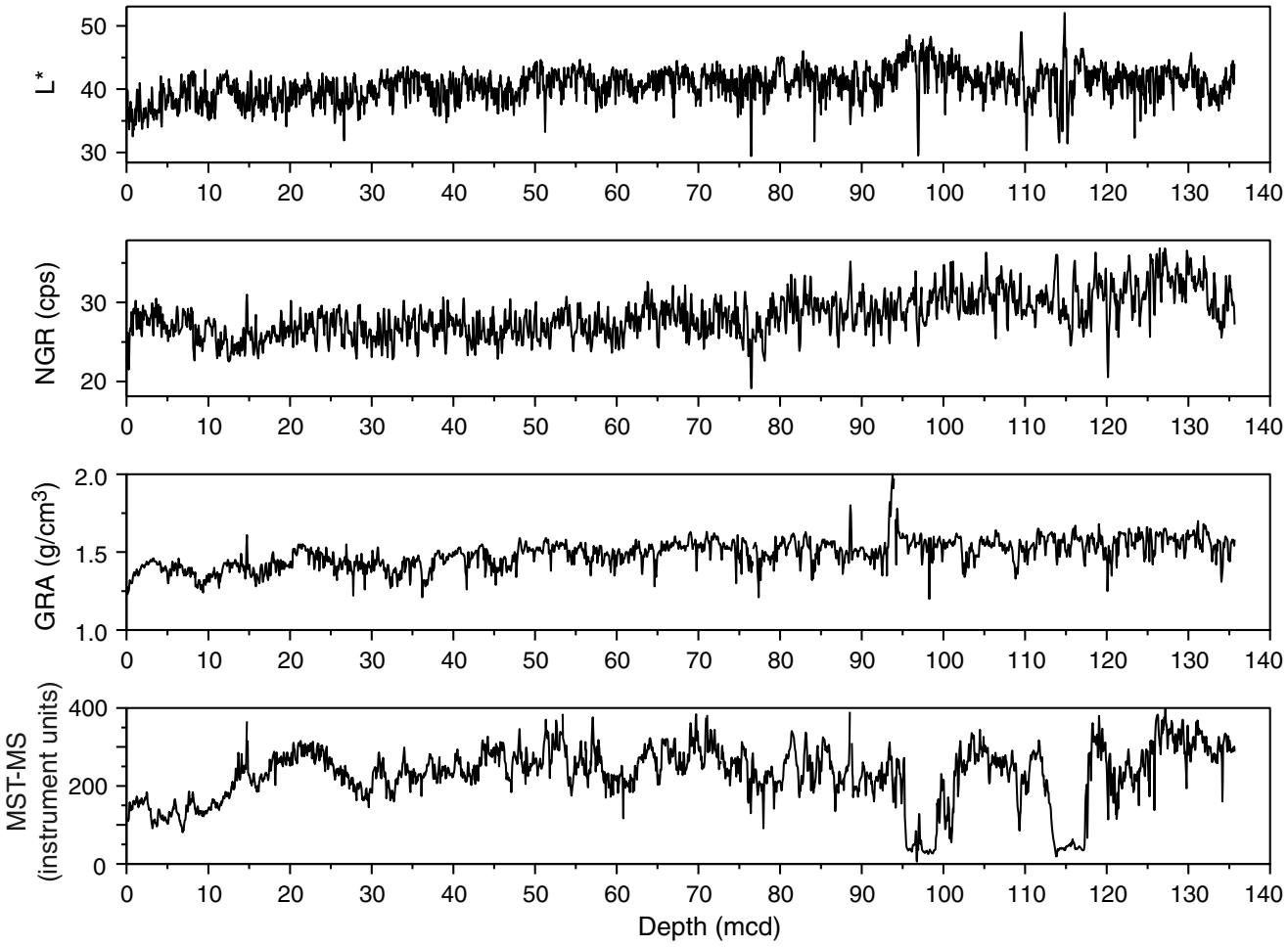

Figure F6. A comparison of the drillers depth (mbsf) and the primary meters composite depth (mcd) scales in Holes 1233A through 1233E. On average, mcd is 18% greater than mbsf. The 1:1 (mbsf:mcd) line is also shown for comparison.

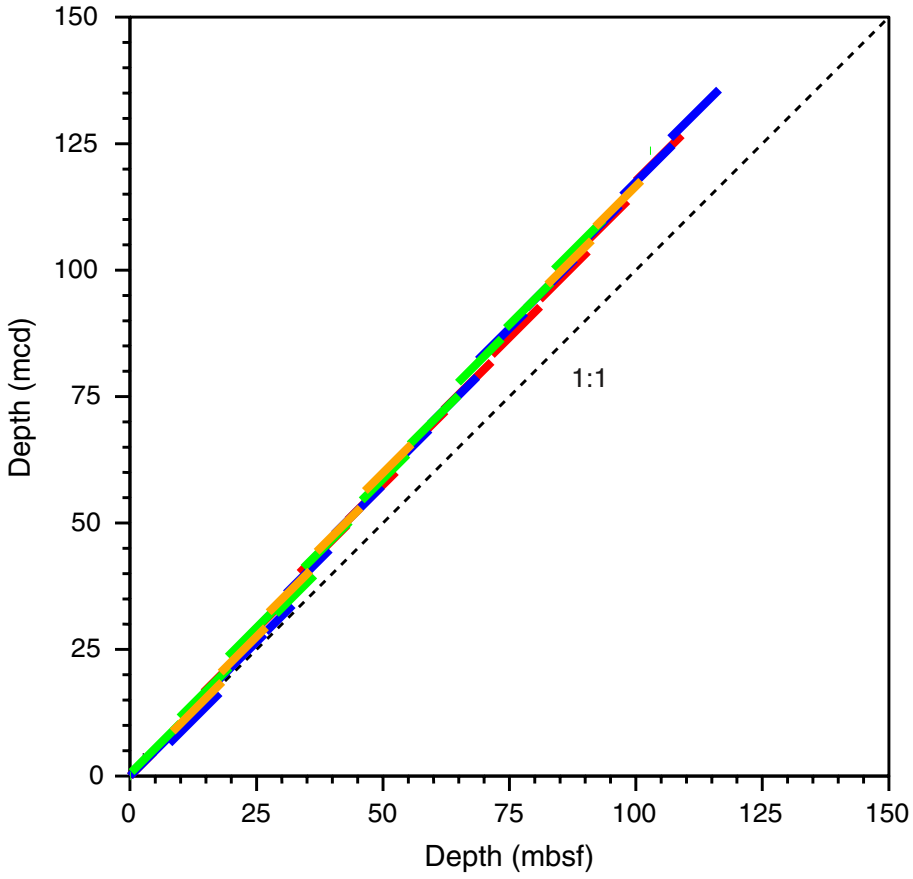

Figure F7. Core recovery, lithostratigraphy, age, percentage reflectance and chroma, gamma ray attenuation (GRA) and MAD (dots) bulk densities, magnetic susceptibility, and natural gamma radiation of recovered sediments from Site 1233. The position of Holocene/Pleistocene boundary is based on a correlation to the ^{14}C-dated sediment record of gravity core GeoB 3313-1). L = Laschamp Excursion (~41 ka).

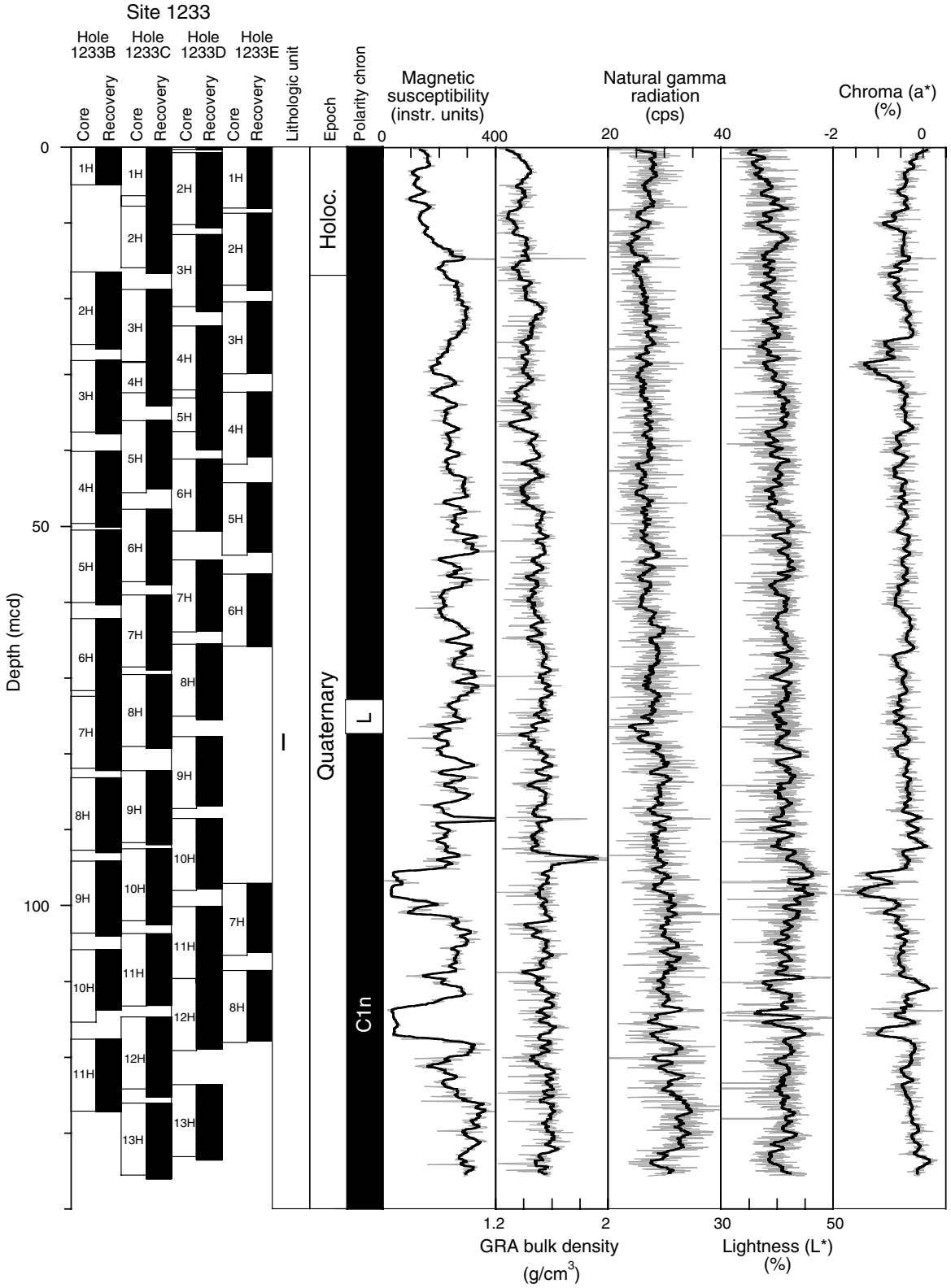

Figure F8. Close-up photograph showing a representative interval of the major lithology at Site 1233 (interval 202-1233-8H-5, 90–110 cm). Sediment color ranges from dark olive gray to dark gray.

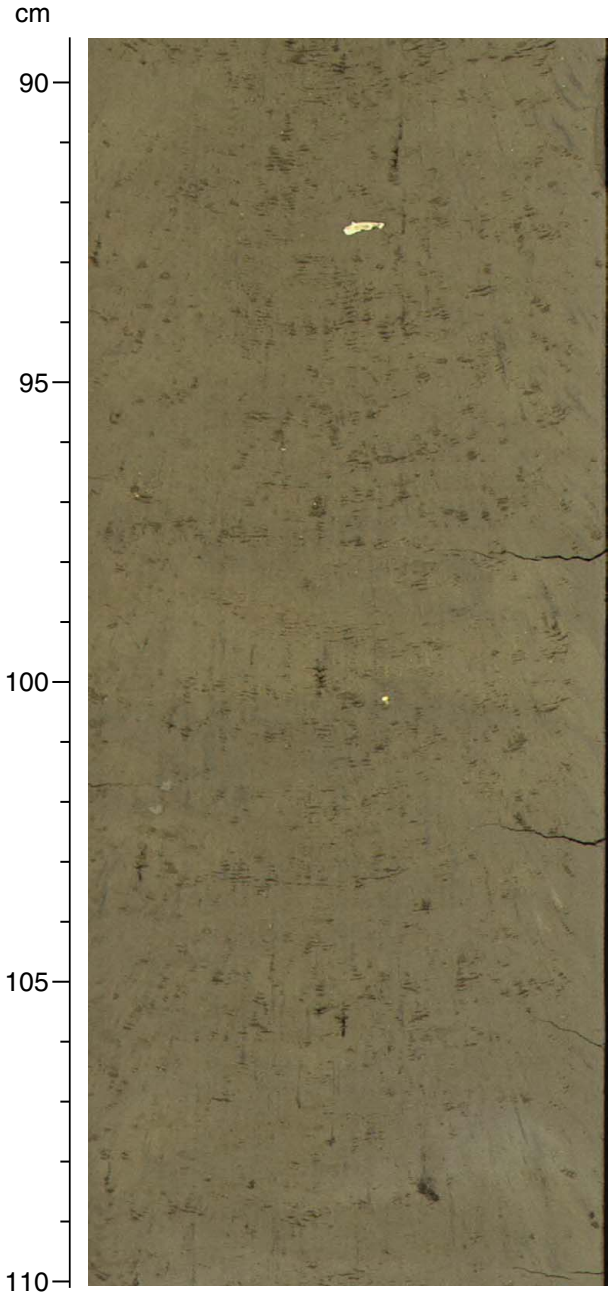

Figure F9. Close-up photograph showing a typical black mottled interval with disseminated monosulfides (interval 202-1233C-6H-5, 2–30 cm).

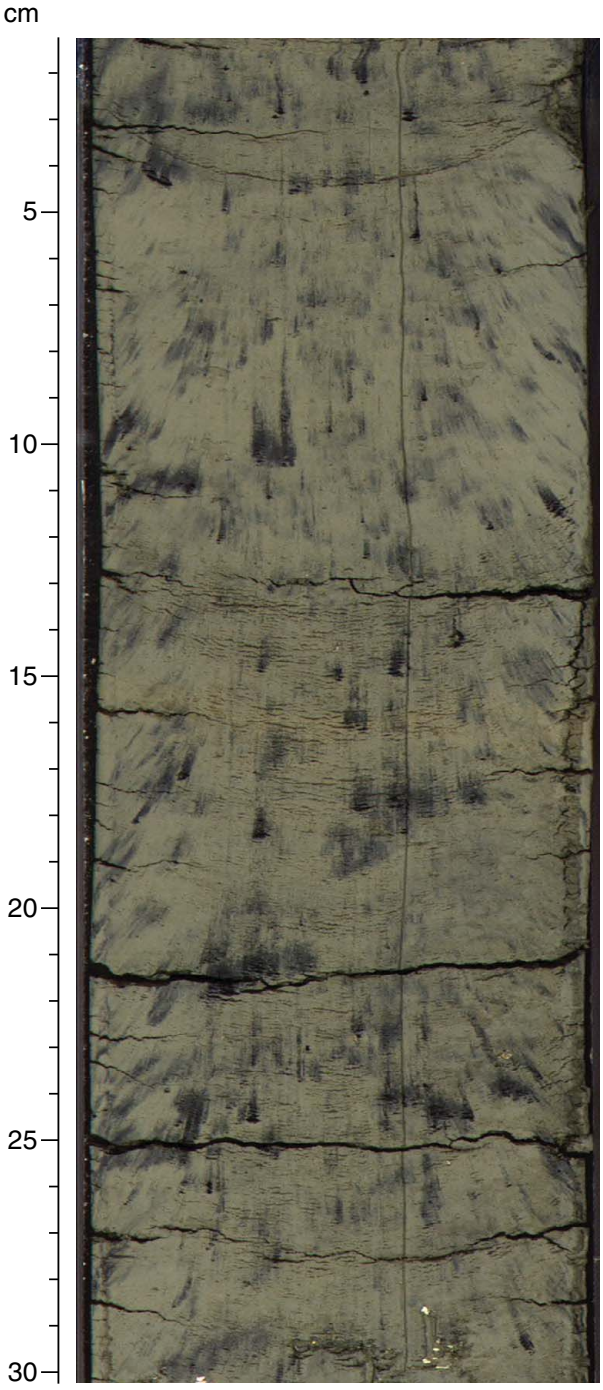

Figure F10. Siliciclastic and authigenic components observed in smear slides (only dominant lithologies) compared to the magnetic susceptibility (MS) record. The position and composition of volcanic ash layers is indicated.

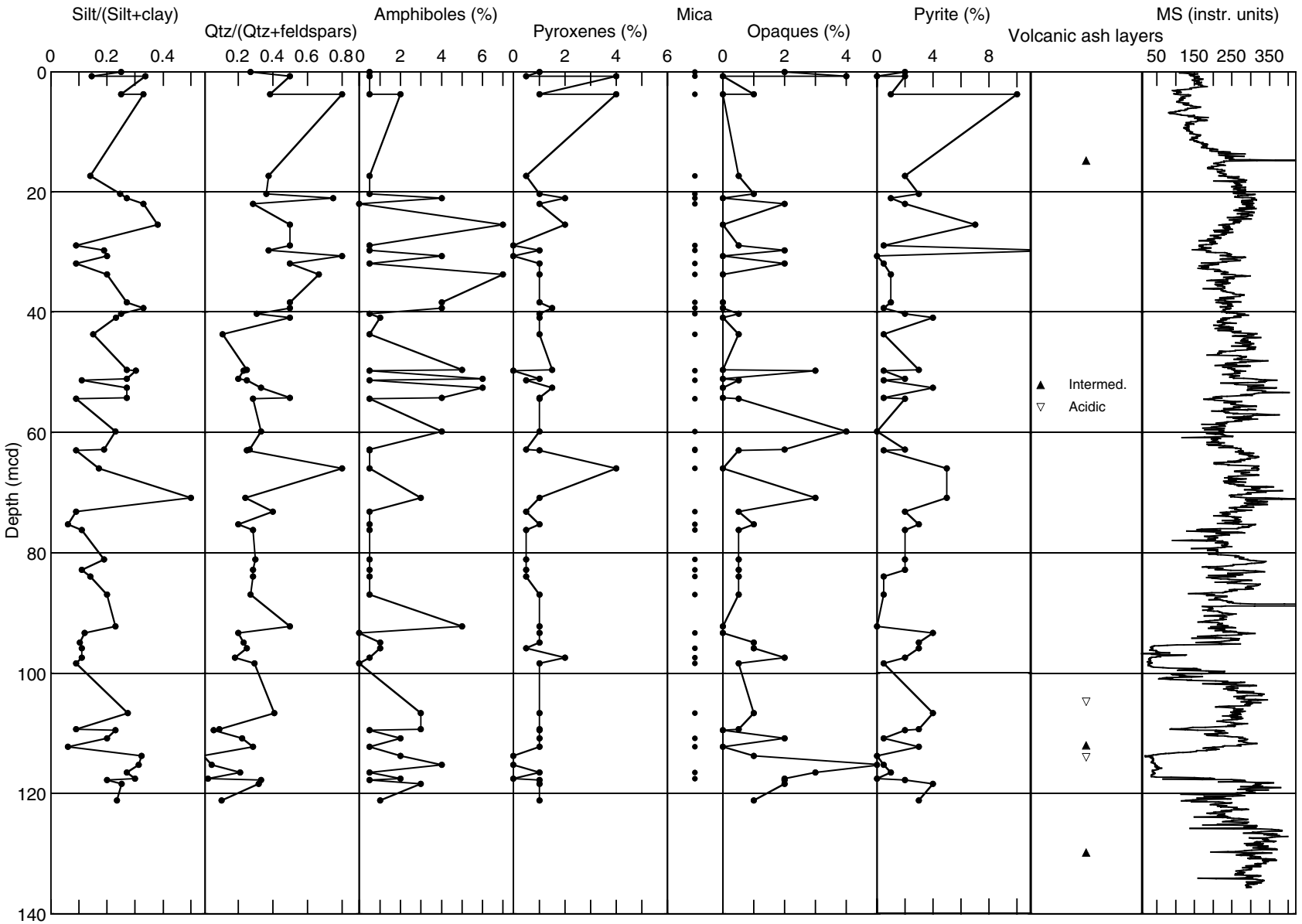

Figure F11. Biogenic components observed in smear slides (only dominant lithologies), calcium carbonate contents (see "Geochemistry," p. 13), and the magnetic susceptibility (Mag. sus.) record.

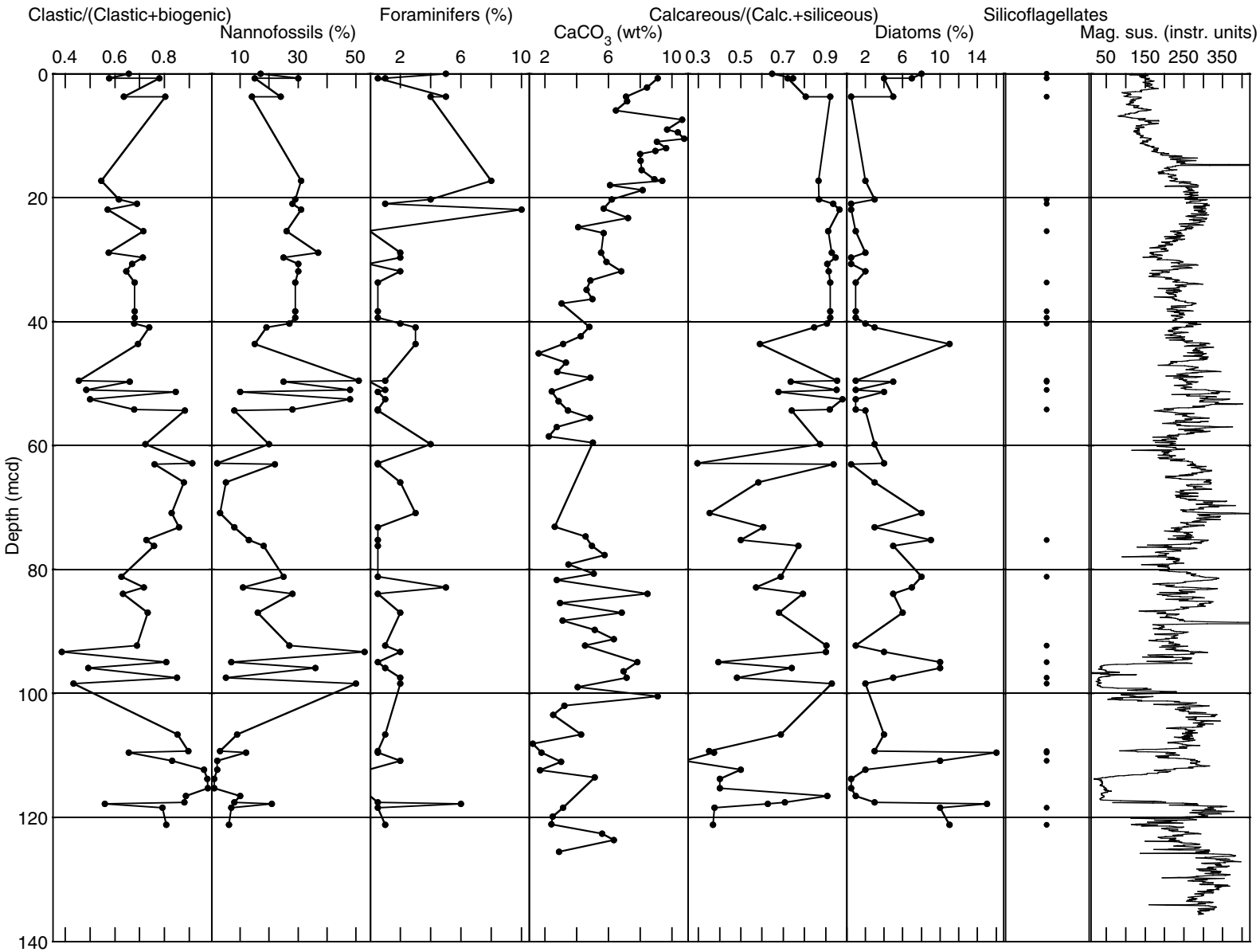

Figure F12. Close-up photograph of a black ash layer of intermediate composition (interval 202-1233C-2H-6, 57–91 cm). The layer is ~8 cm thick, has a sharp basal contact, and grades upward into the overlying sediment.

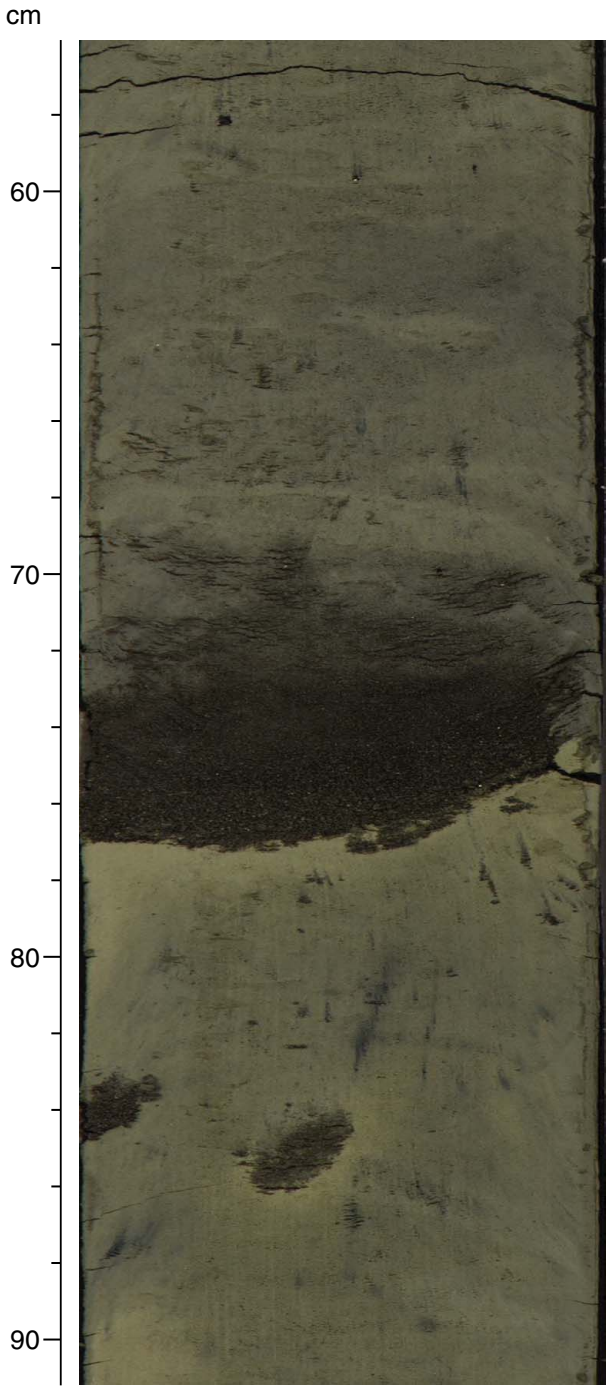

Figure F13. Color measurements plotted in the a*-b* color plane.

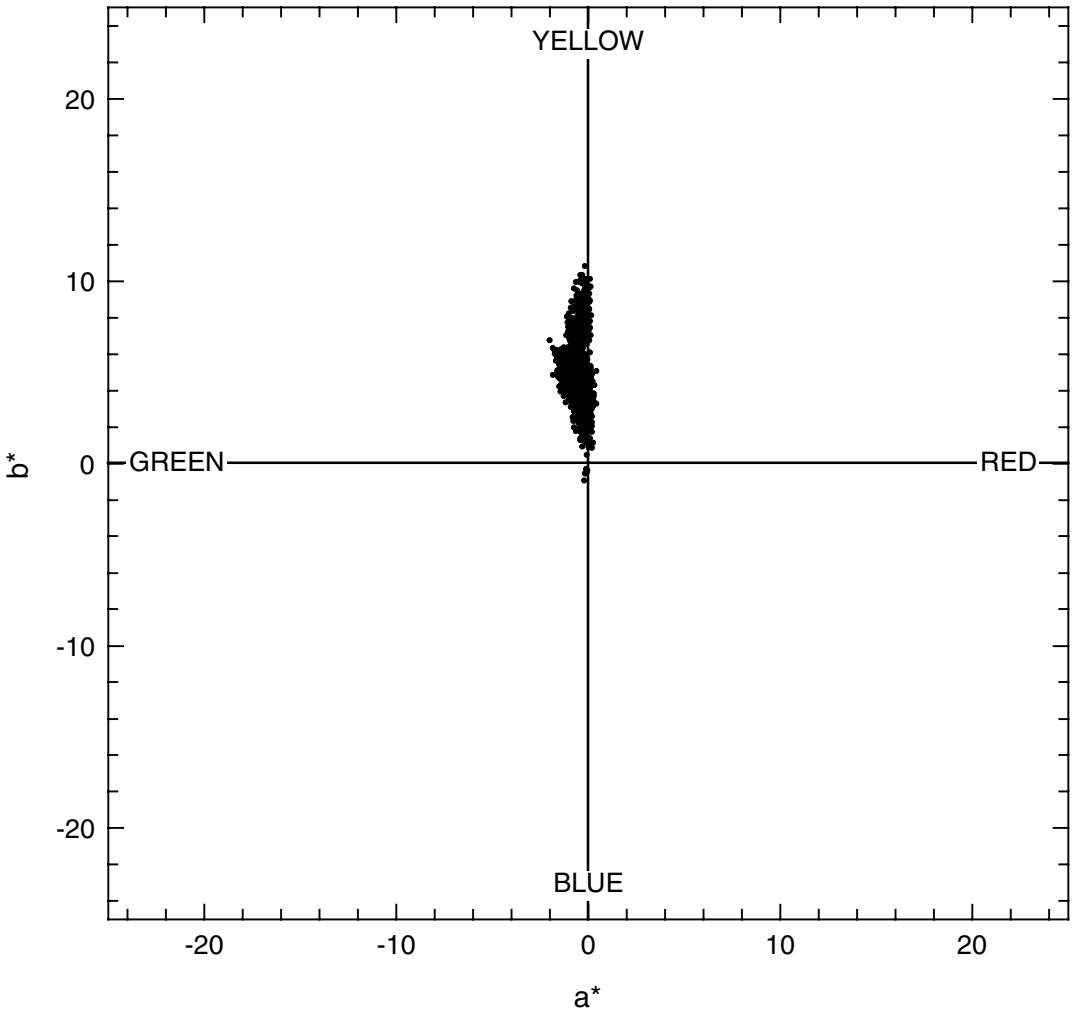

Figure F14. Measured (dots) and predicted (shaded lines) shipboard (**A**) carbonate and (**B**) total organic carbon (TOC). Predicted values are calculated by multiple linear regressions of shipboard reflectance data and geochemical measurements. Correlation coefficients are r^2 = ~0.7 for carbonate and r^2 = ~0.8 for TOC. One measured TOC value with C/N = 18.8 (presumably of terrestrial origin) was not included in the TOC regression.

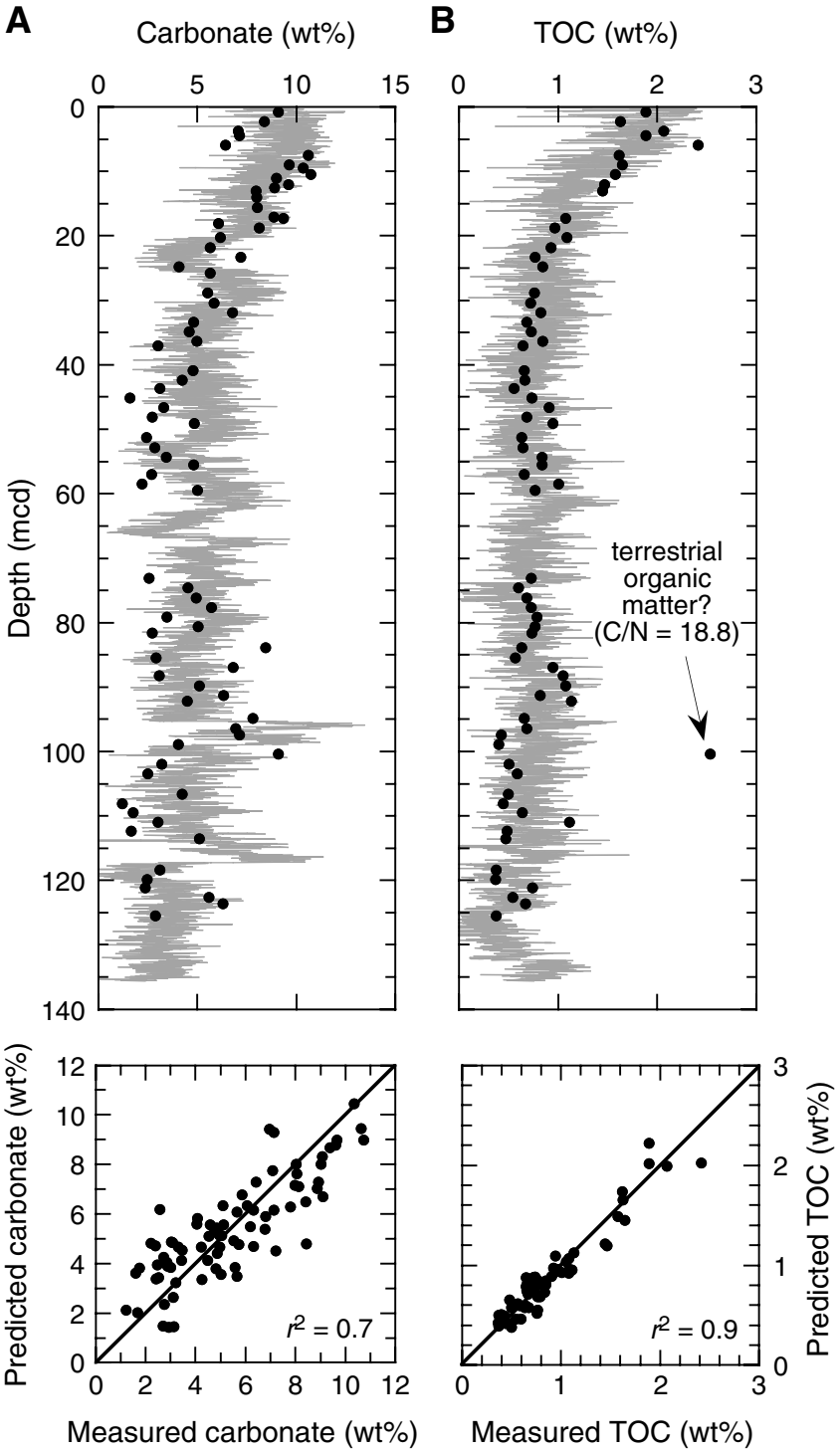

Figure F15. Lithology, and sediment pore water phase relationships. MAD = moisture and density.

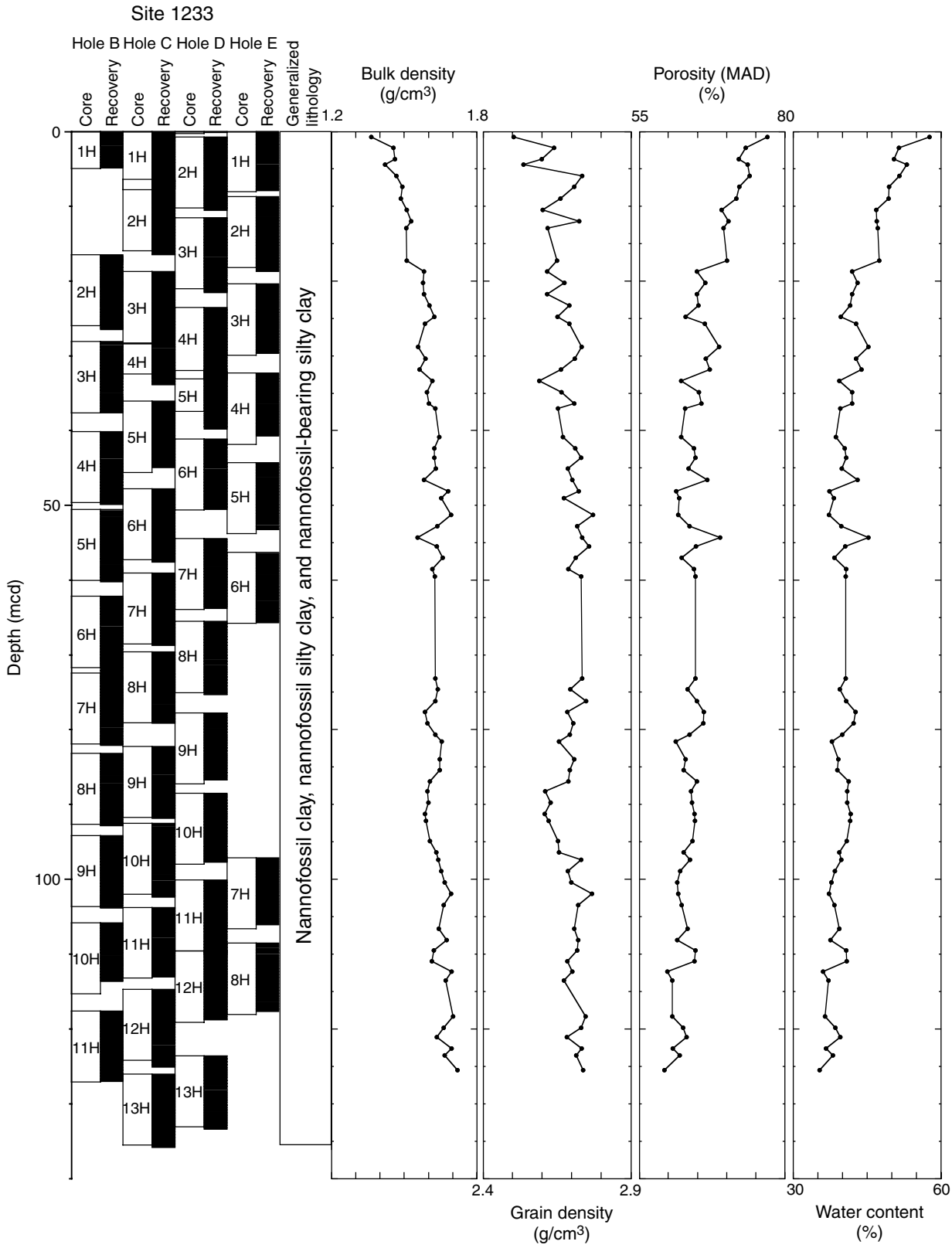

Figure F16. Core recovery, calcareous nannofossil and planktonic foraminifer abundance, benthic foraminifer percentage of total foraminifers, and diatom abundance at Site 1233. R = rare, F = few, C = common, A = abundant.

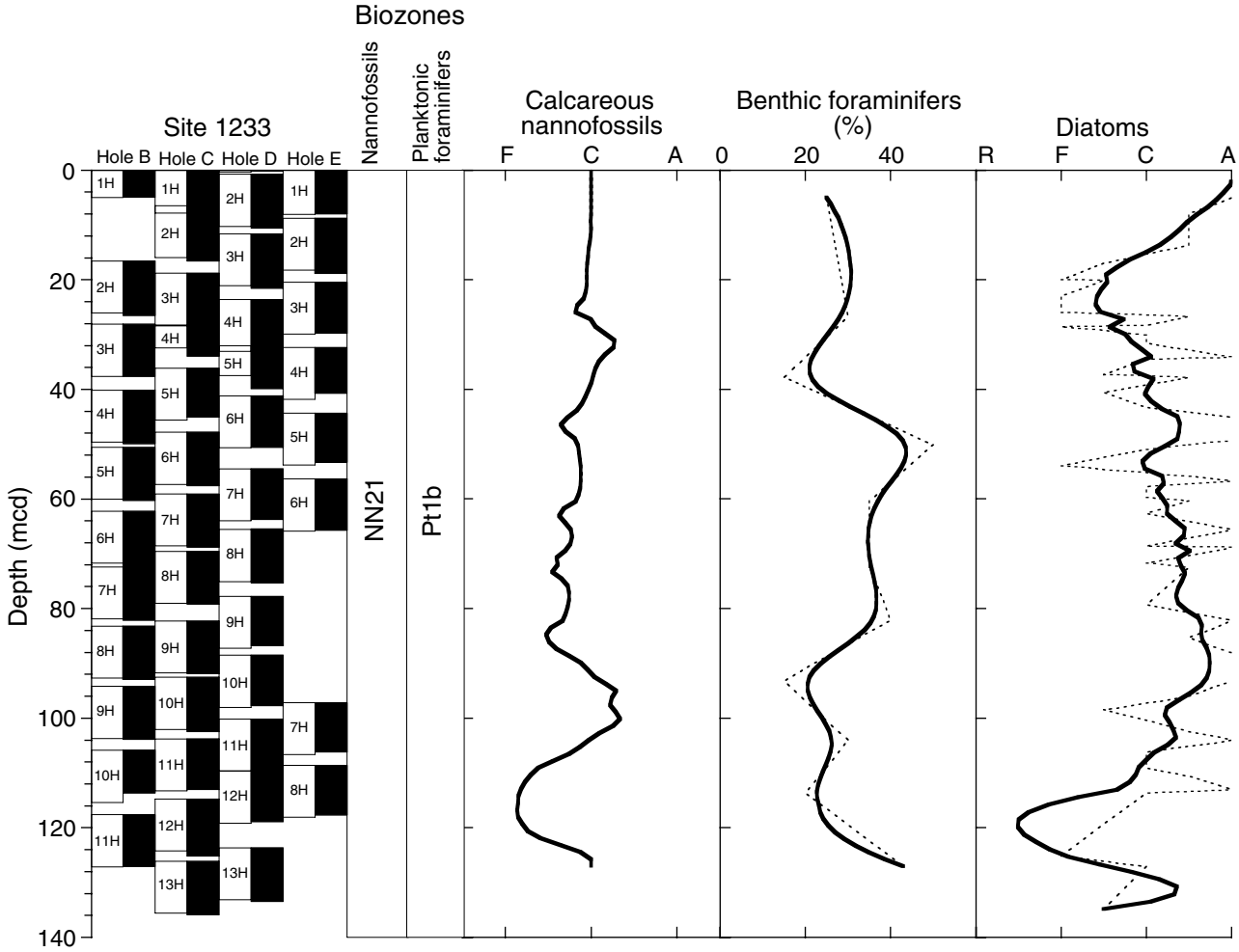

Figure F17. Natural remanent magnetization (NRM) intensity before and after AF demagnetization at peak field of either 20 or 25 mT for the Site 1233 splice.

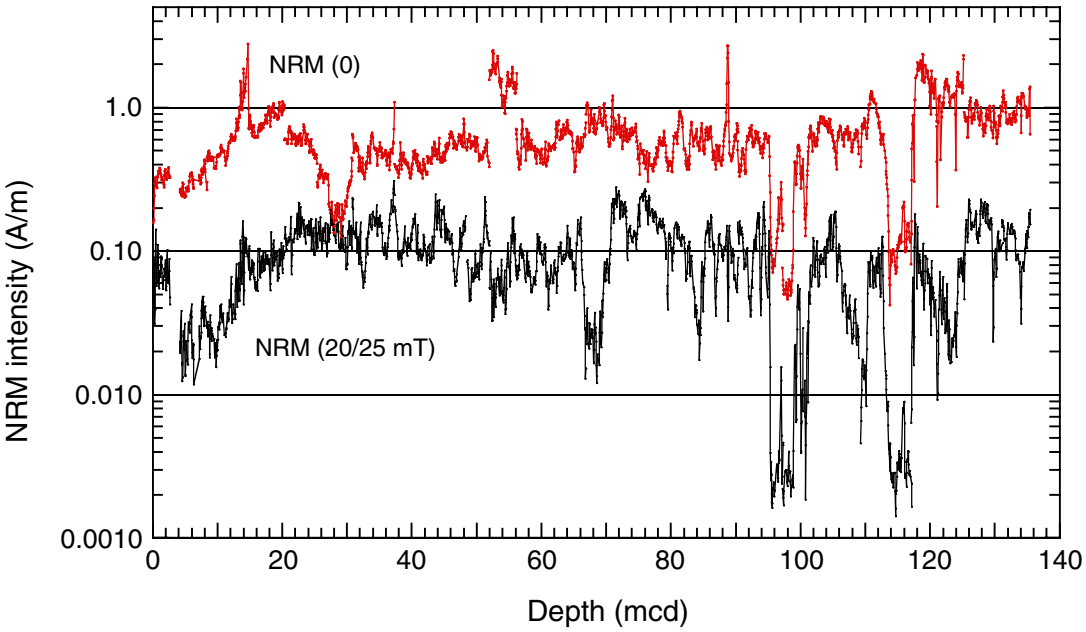

Figure F18. The cleaned natural remanent magnetization (NRM) inclination (top), declination rotated to a core mean of zero (middle) presented before and after smoothing with a seven-point running mean, and intensity (bottom) after demagnetization at 20 or 25 mT for Holes 1233B–1233E. **A.** Inclination for Hole 1233B. **B.** Inclination for Hole 1233C. **C.** Inclination for Hole 1233D. **D.** Inclination for Hole 1233E. **E.** Declination for Hole 1233B. **F.** Declination for Hole 1233C. **G.** Declination for Hole 1233D. **H.** Declination for Hole 1233E. **I.** Declination for Hole 1233B. **J.** NRM intensity for Hole 1233C. **K.** NRM intensity for Hole 1233D. **L.** NRM intensity for Hole 1233E. (**Figure shown on next page.**)

Figure F18 (continued). (Caption shown on previous page.)

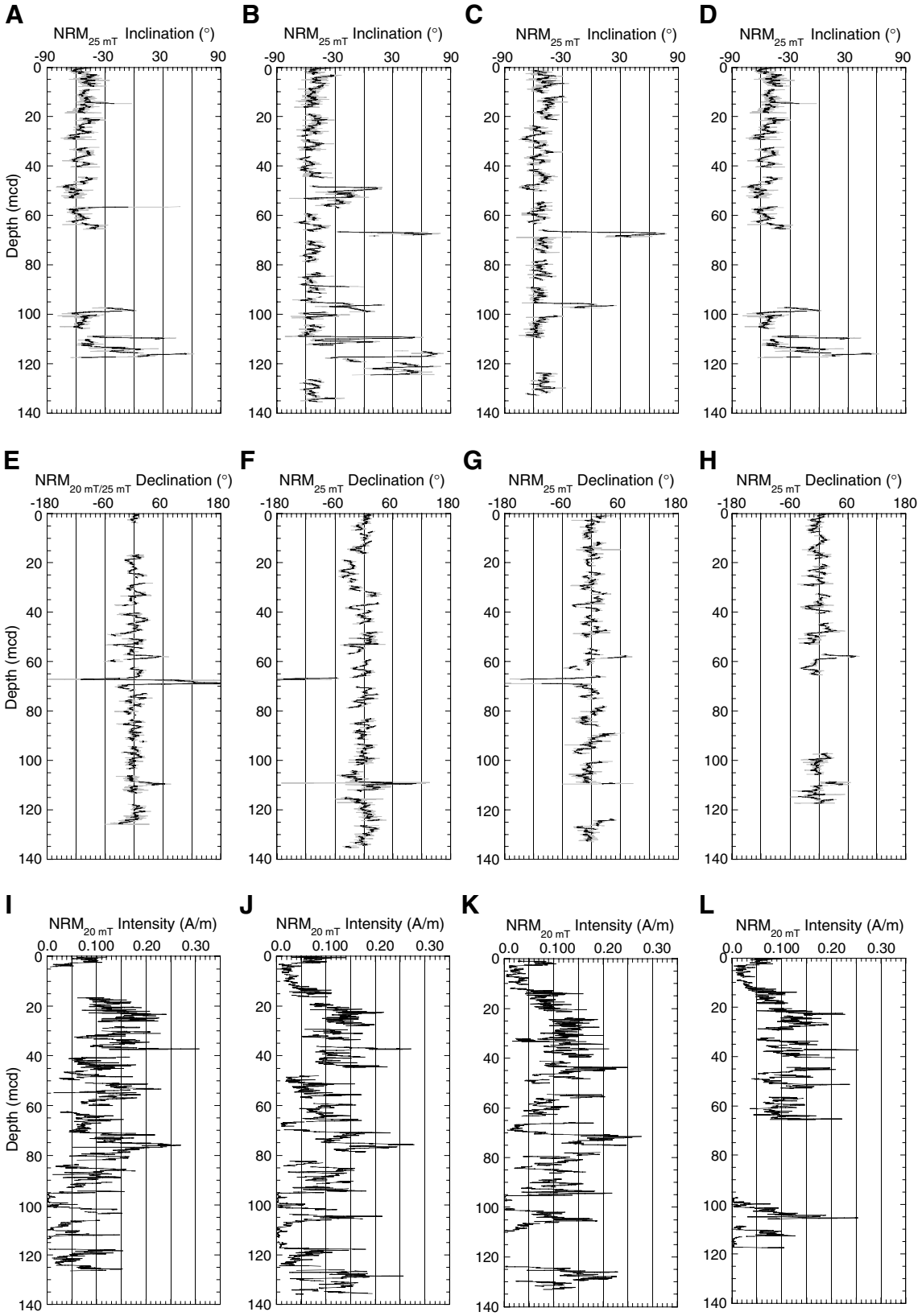

Figure F19. Comparison of declinations (25 mT) from Holes 1233B and 1233D within a 50-m interval. Notice the strong similarity in directional secular variation that can be correlated between these two holes. The solid line represents a seven-point running mean of the individual data points (solid circles).

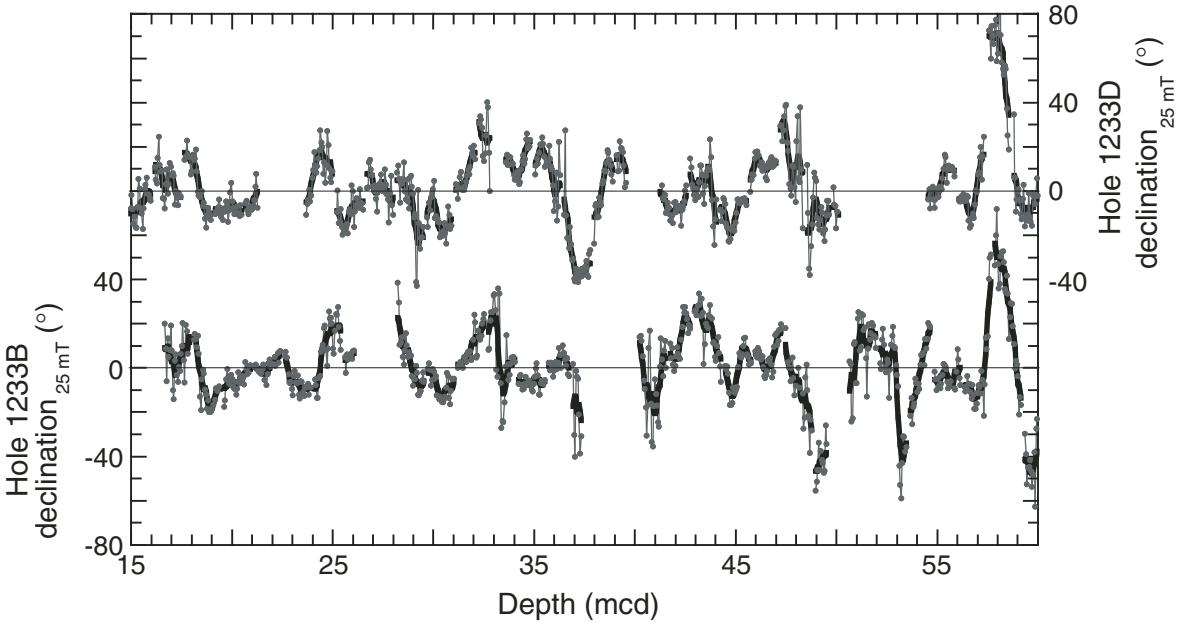

Figure F20. Paleomagnetic field secular variation (PSV) records. **A.** PSV for the last 2000 yr estimated from paleomagnetic studies of lake sediments in Argentina, dating based on bulk-radiocarbon dates. Data for the last 400 yr are the expected directional variability at the site of the lakes based on spherical harmonic analysis of other historical global field data (modified from Lund and Constable, unpubl. data). **B.** PSV recorded in Core 202-1233B-1H. The chronology is derived by correlating magnetic susceptibility to nearby piston core GeoB3313-1, which has been dated by AMS-^{14}C on planktonic foraminifers (Lamy et al., 2001). The distinctive inclination and declination features (labeled I1–I2 and D1–D4) can be correlated to similar PSV features in A.

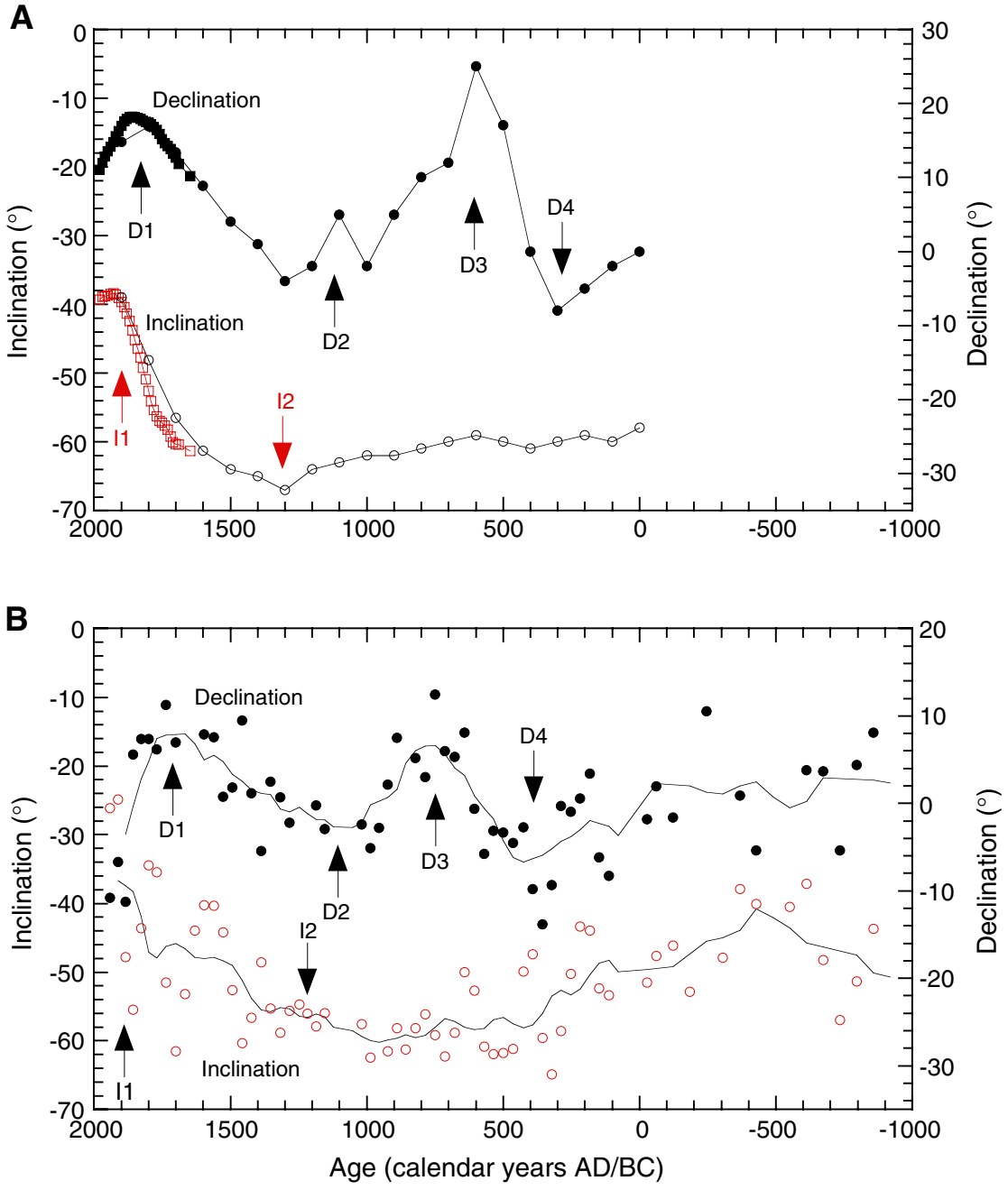

Figure F21. Possible magnetic field excursion recorded in Core 202-1233D-8H. This excursion is also noted in other holes (see Fig. F18, p. 40). Extrapolation of inferred Holocene sedimentation rates would suggest an age of 40–50 ka, suggesting that this may be the Laschamp Excursion, which has an age of ~41 ka. Open squares = declination data, solid circles = inclination data.

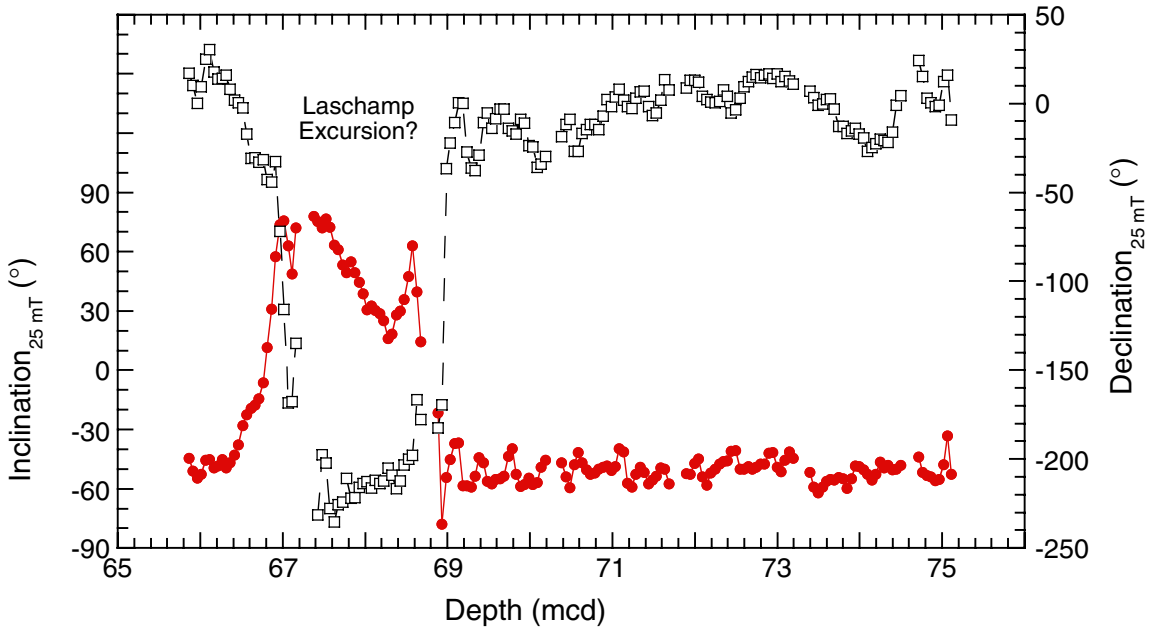

Figure F22. Natural remanent magnetization (NRM) intensity demagnetized at 20 or 25 mT normalized by whole-core MST-derived magnetic susceptibility (MS). **A.** Hole 1233B. **B.** Hole 1233C. **C.** Hole 1233D. **D.** Hole 1233E. **E.** Site 1233 splice.

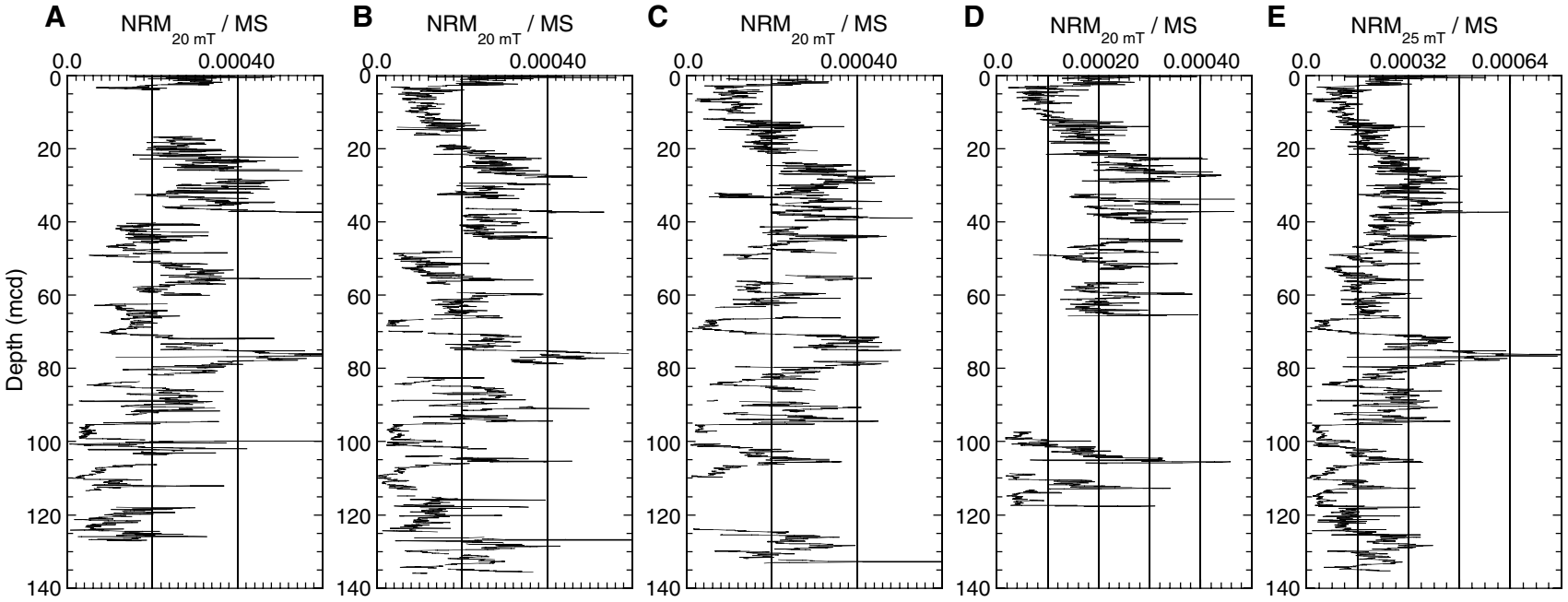

Figure F23. MST-derived whole-core magnetic susceptibility (top) compared with the natural remanent magnetization (NRM) intensity measured after 25-mT AF demagnetization for the lowermost 40 m of the Site 1233 splice. Two intervals of weak magnetic susceptibility and NRM intensity imply diagenetic loss of fine-grained ferromagnetic phases relative to coarse-grained material.

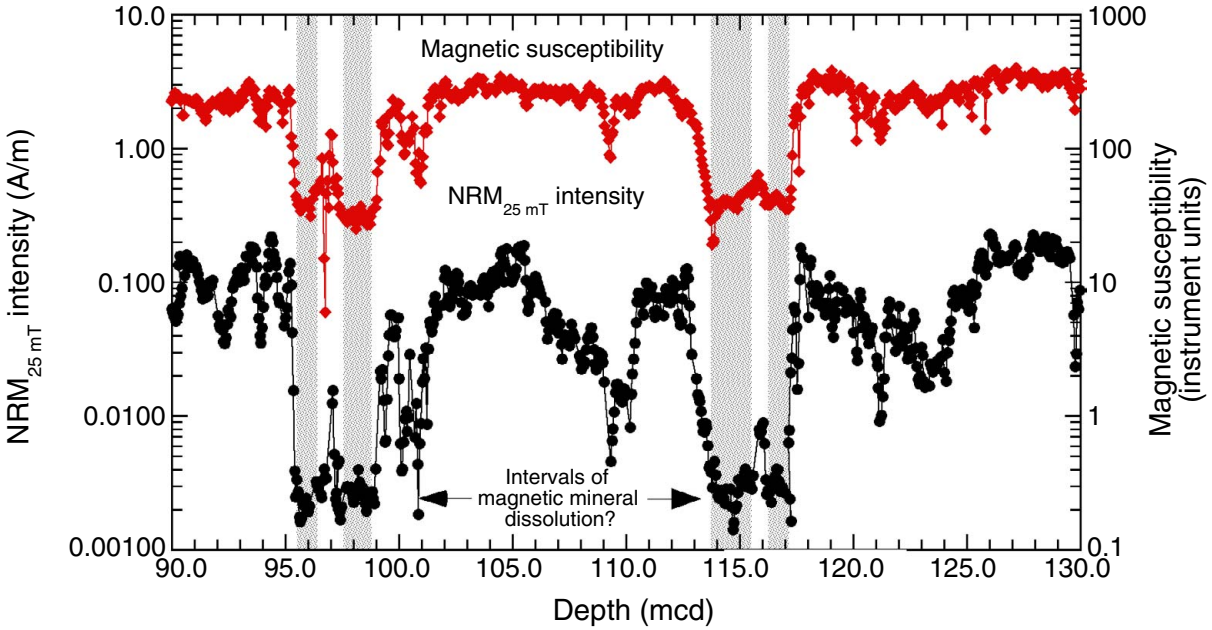

Figure F24. Headspace and vacutainer methane (C_1) concentrations and C_1/C_2 ratio in sediments from Hole 1233A vs. depth. Open circles = headspace, solid circles = vacutainer. Because of the direct sampling method, vacutainer gas concentrations are higher than headspace gas concentrations.

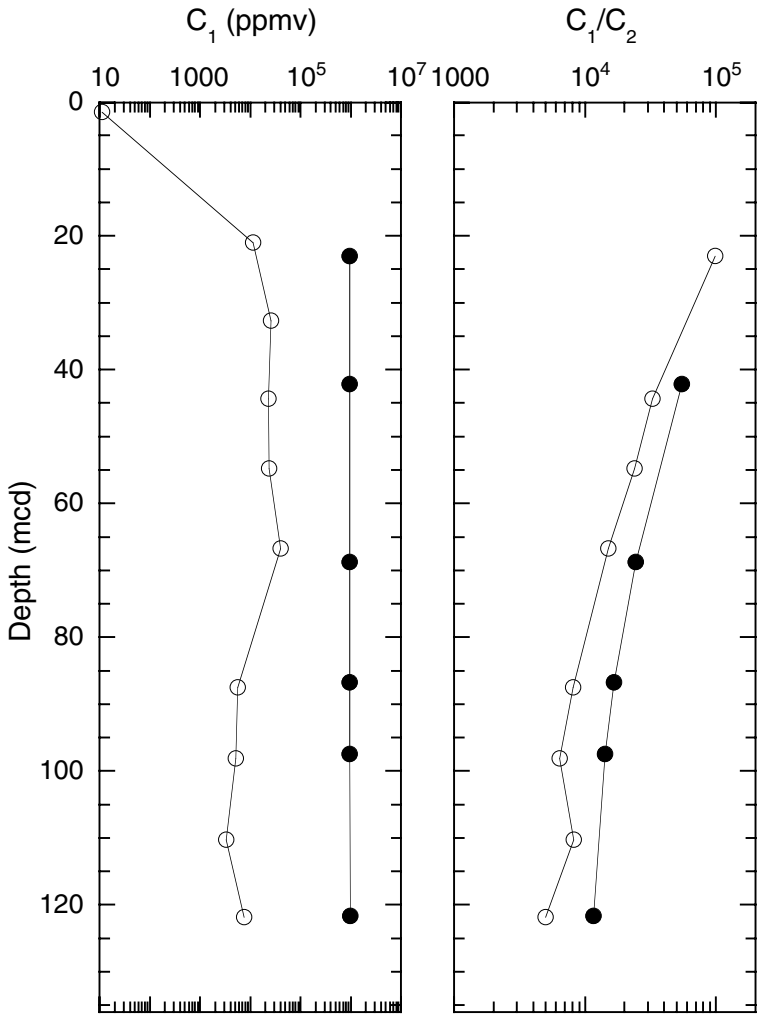

Figure F25. Interstitial water geochemical data for Site 1233. Sulfate values below the detection limit (~0.5 mM) are plotted at zero. Open squares = calcium concentrations.

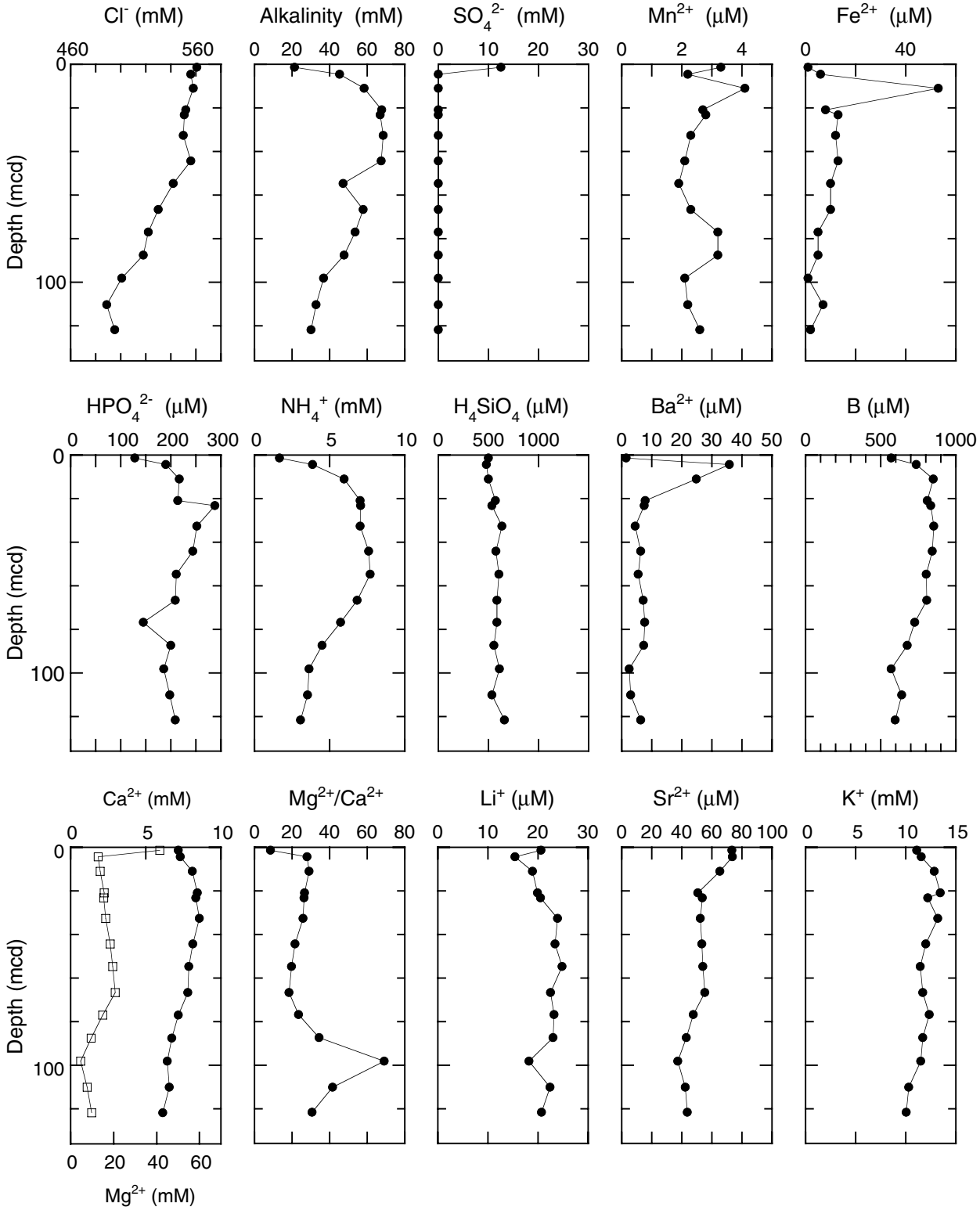

Figure F26. Calcium carbonate ($CaCO_3$), total organic carbon (TOC), and total nitrogen (TN) concentrations vs. depth from sediments of Site 1233. Data from Holes 1233A, 1233B, and 1233E are used to construct single profiles in meters composite depth.

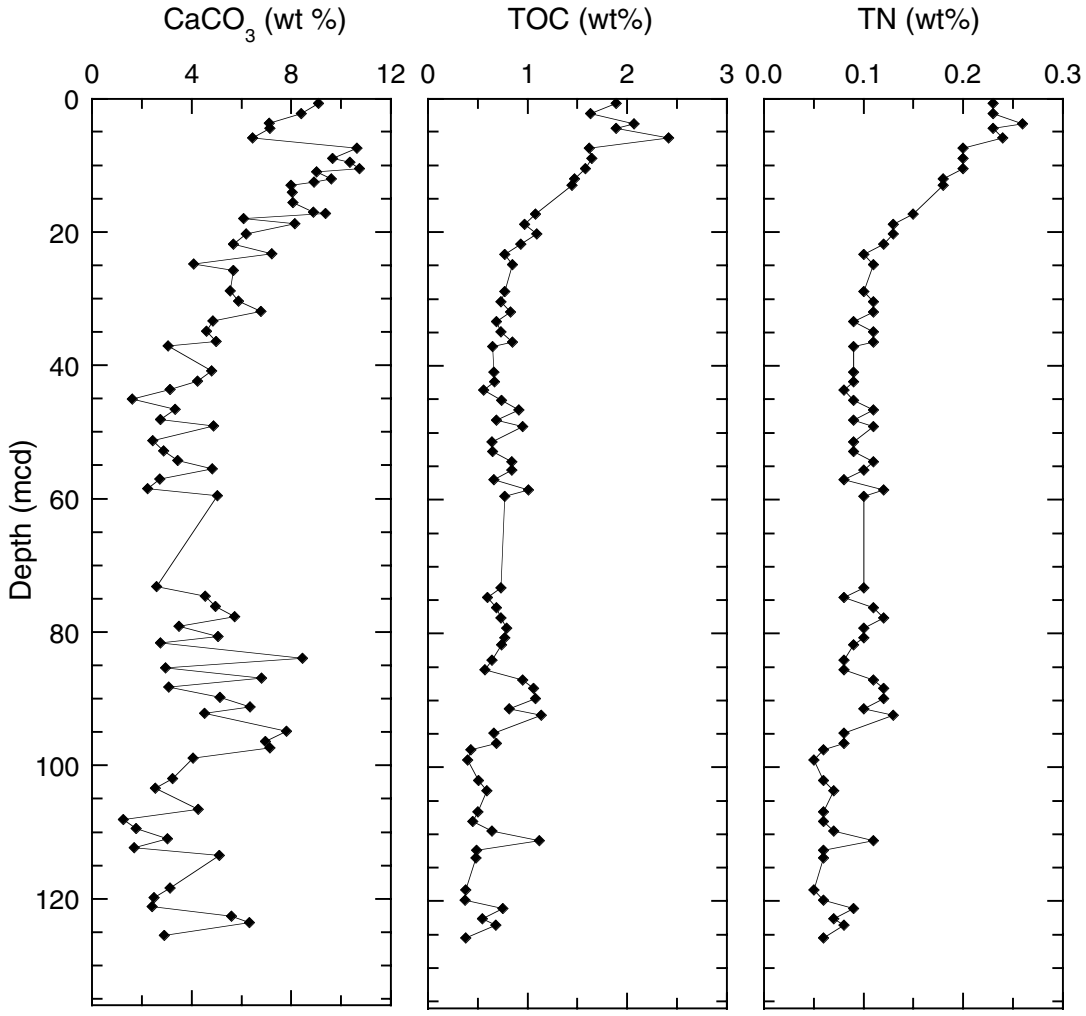

Figure F27. Total organic carbon/total nitrogen (TOC/TN) vs. TOC in sediments at Site 1233.

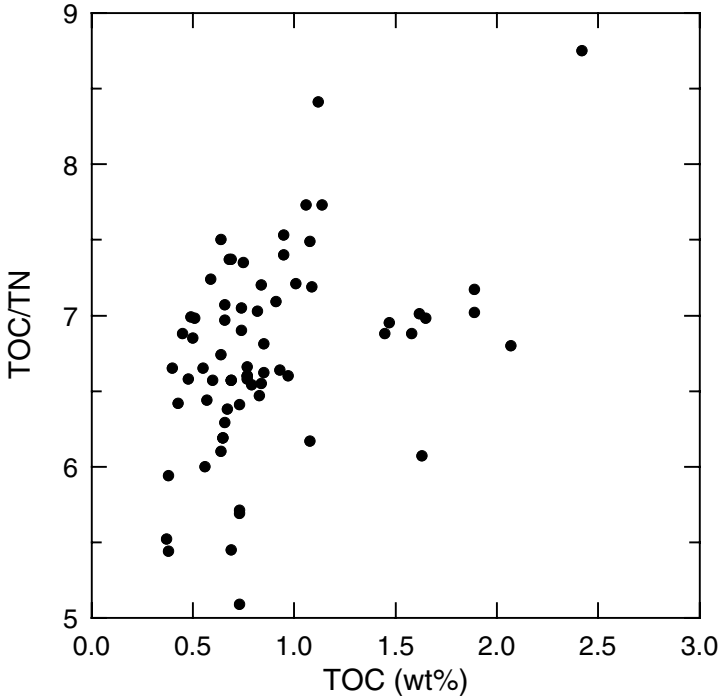

Figure F28. Correlation of magnetic susceptibility records between Site 1233 (thin line) and AMS-^{14}C dated core GeoB 3313-1 vs. age. Assigned tie points for transferring ages from core GeoB 3313-1 to the mcd scale of Site 1233 are indicated. The transfer of age control point 5590 yr is not well constrained because of weak correlation in this interval.

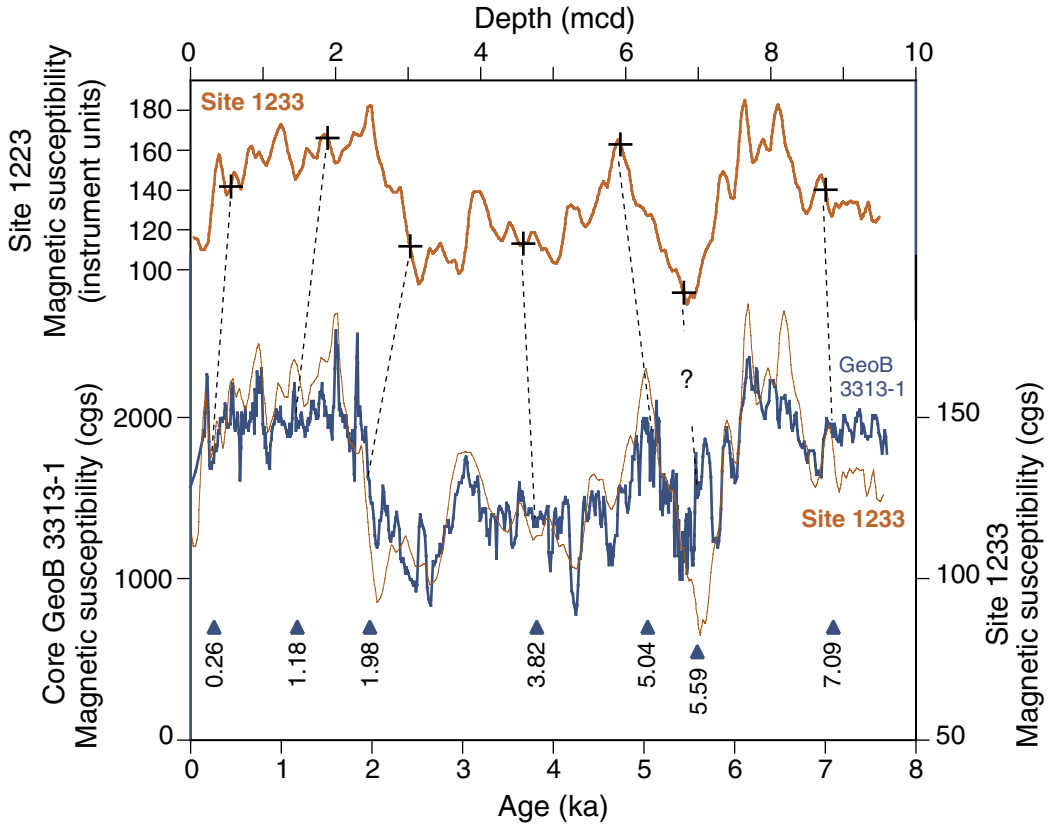

Figure F29. Comparison of a proxy record for relative geomagnetic paleointensity from Site 1233 with the Sint-200 global low-resolution relative paleointensity stack (Guyodo and Valet, 1996) and with a high-resolution southern hemispheric record, shown with a 4-k.y. running mean, from sub-Antarctic South Atlantic ODP Site 1089 (Stoner et al., in press). The Site 1233 shipboard relative paleointensity proxy is derived by normalizing the natural remanent magnetization (NRM) measured after AF demagnetization at 25 mT from archive-half sections with the whole-core MST-derived low-field magnetic susceptibility (MS) (see **"Paleomagnetism,"** p. 11). The record presented is from the shipboard splice. Vertical lines indicate preliminary correlations between Sites 1233 and 1089 and Sint-200. Site 1089 is dated by a high-resolution benthic oxygen isotope record (Stoner et al., 2002). The inferred position of the Laschamp Event is indicated.

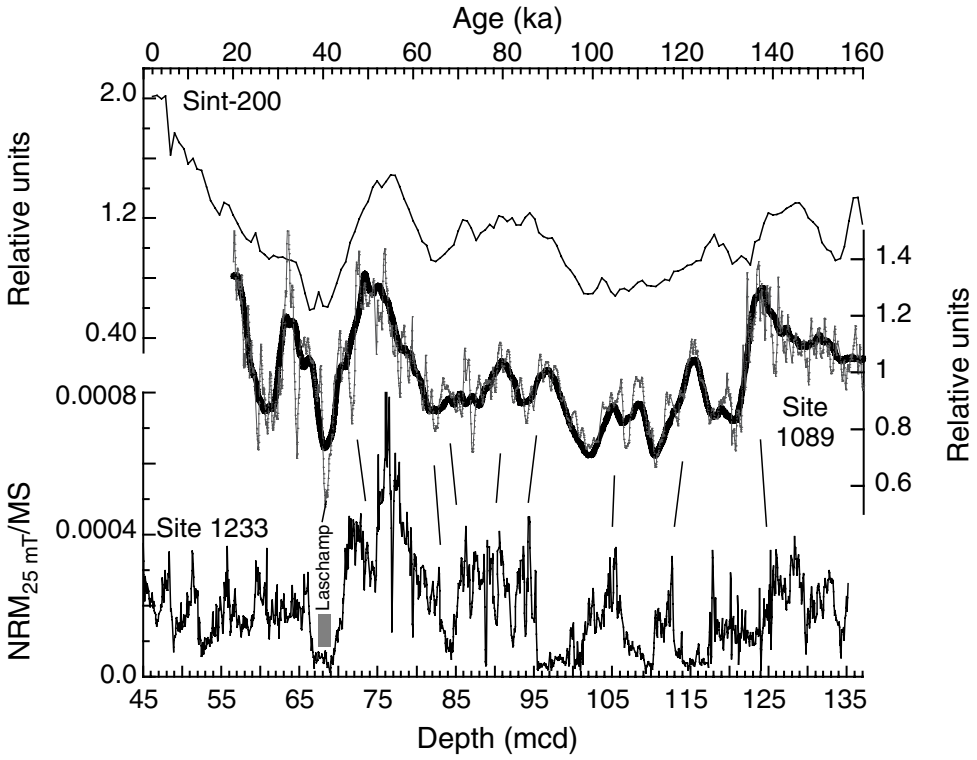

Figure F30. Age-depth model, recovery, linear sedimentation rates (LSRs), and mass accumulation rates (MARs) at Site 1233. MIS = marine isotope stage. AMS = accelerator mass spectrometry.

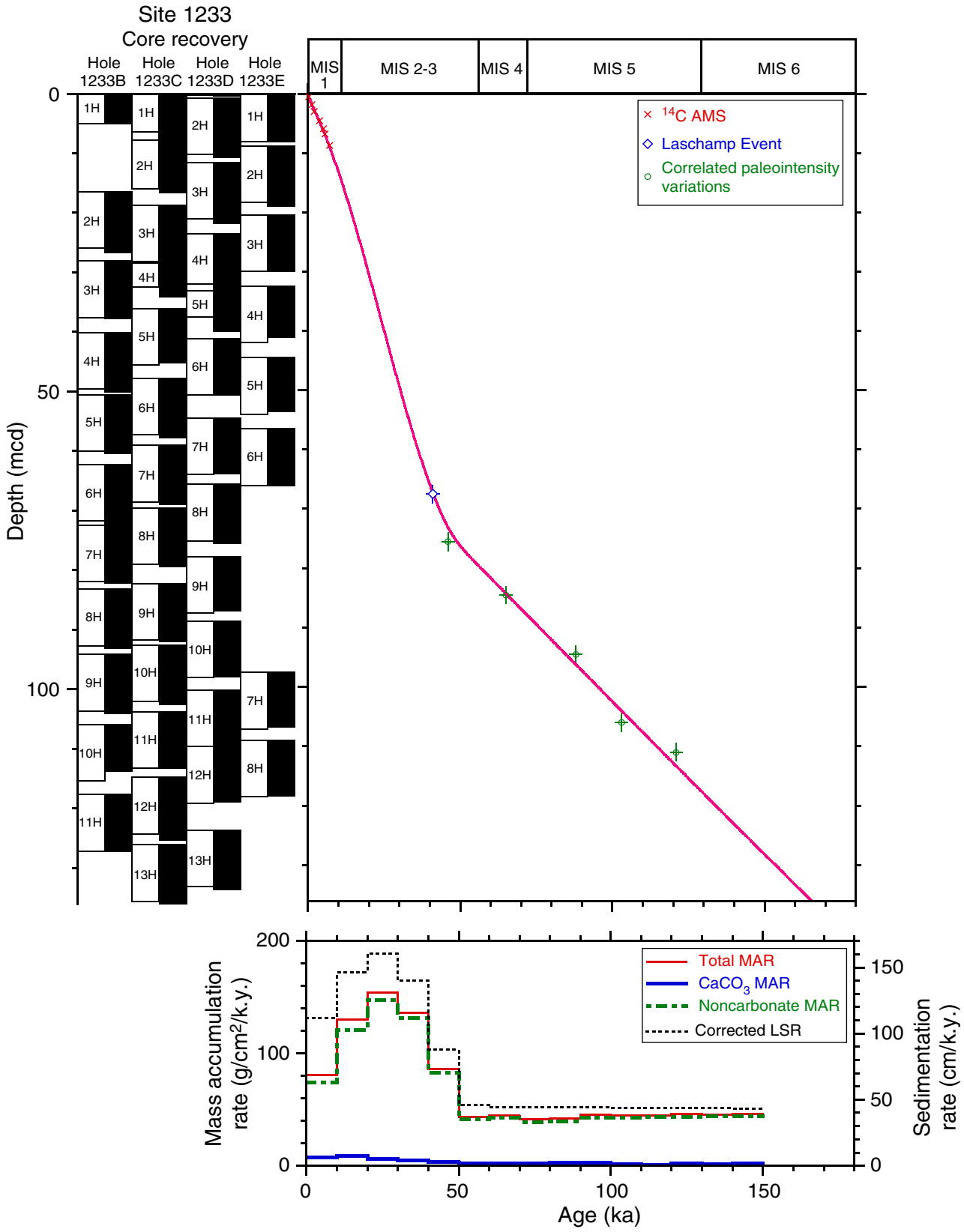

Table T1. Operations summary, Site 1233.

Core	Date (Apr 2002)	Local time (hr)	Depth (mbsf) Top	Depth (mbsf) Bottom	Length (m) Cored	Length (m) Recovered	Recovery (%)	APCT	Orientation
202-1233A-									
1H	12	1350	2.5	12.0	9.5	9.94	104.6		
				Cored totals:	9.5	9.94	104.6		
202-1233B-									
1H	12	1420	0.0	5.0	5.0	5.03	100.6		
2H	12	1500	14.5	24.0	9.5	10.13	106.6		Tensor
3H	12	1525	24.0	33.5	9.5	9.70	102.1		Tensor
4H	12	1625	33.5	43.0	9.5	9.99	105.2	X	Tensor
5H	12	1645	43.0	52.5	9.5	9.83	103.5		Tensor
6H	12	1730	52.5	62.0	9.5	10.28	108.2	X	Tensor
7H	12	1800	62.0	71.5	9.5	9.80	103.2		Tensor
8H	12	1845	71.5	81.0	9.5	9.85	103.7	X	Tensor
9H	12	1920	81.0	90.5	9.5	9.88	104.0		Tensor
10H	12	1950	90.5	100.0	9.5	7.93	83.5		Tensor
11H	12	2055	100.0	109.5	9.5	9.59	101.0	X	Tensor
				Cored totals:	100.0	102.01	102.0		
202-1233C-									
1H	12	2310	0.0	7.8	7.8	7.87	100.9	X	
2H	12	2345	7.8	17.3	9.5	10.21	107.5		
3H	13	0020	17.3	26.8	9.5	9.61	101.2		Tensor
4H	13	0055	26.8	30.8	4.0	5.69	142.3		Tensor
5H	13	0125	30.8	40.3	9.5	9.04	95.2		Tensor
6H	13	0220	40.3	49.8	9.5	9.95	104.7	X	Tensor
7H	13	0250	49.8	59.3	9.5	9.86	103.8		Tensor
8H	13	0325	59.3	68.8	9.5	9.74	102.5		Tensor
9H	13	0400	68.8	78.3	9.5	9.71	102.2		Tensor
10H	13	0430	78.3	87.8	9.5	10.07	106.0		Tensor
11H	13	0505	87.8	97.3	9.5	9.45	99.5		Tensor
12H	13	0605	97.3	106.8	9.5	10.58	111.4	X	Tensor
13H	13	0645	106.8	116.3	9.5	9.97	105.0		Tensor
				Cored totals:	116.3	121.75	104.7		
202-1233D-									
1H	13	0820	0.0	0.3	0.3	0.35	116.7		
2H	13	0850	0.3	9.8	9.5	9.96	104.8		
3H	13	0915	9.8	19.3	9.5	10.20	107.4		
4H	13	1010	19.3	28.8	9.5	9.74	102.5		Tensor
5H	13	1035	28.8	34.3	5.5	7.91	143.8		Tensor
6H	13	1105	34.3	43.8	9.5	9.52	100.2		Tensor
7H	13	1225	45.8	55.3	9.5	9.41	99.1		Tensor
8H	13	1310	55.3	64.8	9.5	9.95	104.7		Tensor
9H	13	1340	64.8	74.3	9.5	9.10	95.8		Tensor
10H	13	1410	74.3	83.8	9.5	9.30	97.9		Tensor
11H	13	1500	83.8	93.3	9.5	10.16	107.0		Tensor
12H	13	1535	93.3	102.8	9.5	9.30	97.9		Tensor
13H	13	1645	102.8	112.3	9.5	9.98	105.1		Tensor
				Cored totals:	110.3	114.88	104.2		
202-1233E-									
1H	13	1800	0.0	8.4	8.4	8.44	100.5		
2H	13	1830	8.4	17.9	9.5	10.18	107.2		
3H	13	1910	17.9	27.4	9.5	9.47	99.7		Tensor
4H	13	1945	27.4	36.9	9.5	8.51	89.6		Tensor
5H	13	2020	36.9	46.4	9.5	9.10	95.8		Tensor
6H	13	2100	46.4	55.9	9.5	9.55	100.5		Tensor
7H	13	2240	82.5	92.0	9.5	9.13	96.1		Tensor
8H	13	2350	92.0	101.5	9.5	9.27	97.6		Tensor
				Cored totals:	74.9	73.65	98.3		
				Site totals:	411.0	422.23	102.7		

Notes: APCT = advanced piston corer temperature tool (stainless-steel housing is cutting shoe). X = APCT was used. Tensor = brand name for core-barrel orientation tool.

Table T2. Primary composite depth scale, Site 1233.

Core	Depth of core top		Depth offset		Translation to cmcd	
	Drillers (mbsf)	Composite (mcd)	Cumulative (m)	Differential (m)	Growth factor*	Depth (cmcd)†
202-1233A-						
1H	2.5	3.70	1.20		1.18	3.14
202-1233B-						
1H	0.0	0.00	0.00		1.18	0.00
2H	14.5	16.53	2.03	2.03	1.18	14.01
3H	24.0	28.14	4.14	2.11	1.18	23.85
4H	33.5	40.15	6.65	2.51	1.18	34.03
5H	43.0	50.57	7.57	0.92	1.18	42.86
6H	52.5	62.22	9.72	2.15	1.18	52.73
7H	62.0	72.42	10.42	0.70	1.18	61.37
8H	71.5	83.20	11.70	1.28	1.18	70.51
9H	81.0	94.18	13.18	1.48	1.18	79.81
10H	90.5	105.88	15.38	2.20	1.18	89.73
11H	100.0	117.65	17.65	2.27	1.18	99.70
202-1233C-						
1H	0.0	0.00	0.00		1.18	0.00
2H	7.8	6.46	–1.34	–1.34	1.18	5.47
3H	17.3	18.78	1.48	2.82	1.18	15.92
4H	26.8	28.44	1.64	0.16	1.18	24.10
5H	30.8	36.10	5.30	3.66	1.18	30.59
6H	40.3	47.81	7.51	2.21	1.18	40.52
7H	49.8	59.09	9.29	1.78	1.18	50.08
8H	59.3	69.58	10.28	0.99	1.18	58.97
9H	68.8	82.27	13.47	3.19	1.18	69.72
10H	78.3	92.53	14.23	0.76	1.18	78.42
11H	87.8	103.77	15.97	1.74	1.18	87.94
12H	97.3	114.73	17.43	1.46	1.18	97.23
13H	106.8	126.09	19.29	1.86	1.18	106.86
202-1233D-						
1H	0.0	0.00	0.00		1.18	0.00
2H	0.3	0.76	0.46	0.46	1.18	0.64
3H	9.8	11.57	1.77	1.31	1.18	9.81
4H	19.3	23.60	4.30	2.53	1.18	20.00
5H	28.8	32.01	3.21	–1.09	1.18	27.13
6H	34.3	41.15	6.85	3.64	1.18	34.87
7H	45.8	54.48	8.68	1.83	1.18	46.17
8H	55.3	65.57	10.27	1.59	1.18	55.57
9H	64.8	77.76	12.96	2.69	1.18	65.90
10H	74.3	88.54	14.24	1.28	1.18	75.03
11H	83.8	100.15	16.35	2.11	1.18	84.87
12H	93.3	109.65	16.35	0.00	1.18	92.92
13H	102.8	123.63	20.83	4.48	1.18	104.77
202-1233E-						
1H	0.0	–0.34	–0.34		1.18	–0.29
2H	8.4	8.77	0.37	0.71	1.18	7.43
3H	17.9	20.43	2.53	2.16	1.18	17.31
4H	27.4	32.35	4.95	2.42	1.18	27.42
5H	36.9	44.31	7.41	2.46	1.18	37.55
6H	46.4	56.32	9.92	2.51	1.18	47.73
7H	82.5	97.13	14.63	4.71	1.18	82.31
8H	92.0	108.58	16.58	1.95	1.18	92.02

Notes: * = calculated based on mbsf-mcd relationship for splice shown in Figure **F6,** p. 28. † = within the splice, the following equations apply: cmcd = mcd/growth factor, mcd = mbsf + cumulative depth offset, mcd = cmcd × growth factor, mbsf = cmcd × growth factor – cumulative offset. This table is also available in **ASCII.**

Table T3. Primary splice tie points, Site 1233.

Hole, core, section, interval (cm)	Depth (mbsf)	Depth (mcd)	Depth (cmcd)		Hole, core, section, interval (cm)	Depth (mbsf)	Depth (mcd)	Depth (cmcd)
202-					202-			
1233C-1H-3, 120	4.21	4.21	3.57	Tie to	1233D-2H-3, 45	3.75	4.21	3.57
1233D-2H-6, 15	7.95	8.41	7.13	Tie to	1233C-2H-2, 45	9.75	8.41	7.13
1233C-2H-5, 95	14.81	13.47	11.42	Tie to	1233D-3H-2, 40	11.70	13.47	11.42
1233D-3H-6, 125	18.56	20.33	17.23	Tie to	1233C-3H-2, 5	18.85	20.33	17.23
1233C-3H-5, 70	23.92	25.40	21.53	Tie to	1233D-4H-2, 30	21.10	25.40	21.53
1233D-4H-5, 125	26.54	30.84	26.14	Tie to	1233B-3H-2, 120	26.70	30.84	26.14
1233B-3H-7, 55	33.26	37.40	31.69	Tie to	1233C-5H-1, 130	32.10	37.40	31.69
1233C-5H5, 30	37.10	42.40	35.93	Tie to	1233D-6H-1, 125	35.55	42.40	35.93
1233D-6H-6, 5	41.67	48.52	41.12	Tie to	1233E-5H-3, 121	41.11	48.52	41.12
1233E-5H-6, 20	44.56	51.97	44.04	Tie to	1233C-6H-3, 149	44.46	51.97	44.04
1233C-6H-6, 130	48.77	56.28	47.69	Tie to	1233D-7H-2, 15	47.45	56.13	47.57
1233D-7H-6, 110	54.06	62.74	53.17	Tie to	1233C-7H-3, 80	53.60	62.89	53.30
1233C,-7H-6, 40	57.63	66.92	56.71	Tie to	1233D-8H-2, 115	56.65	66.92	56.71
1233D-8H-6, 135	62.86	73.13	61.97	Tie to	1233B-7H-1, 69	62.71	73.13	61.97
1233B,-7H-5, 95	68.95	79.37	67.26	Tie to	1233D-9H-3, 5	66.41	79.37	67.26
1233D-9H-6, 75	71.19	84.15	71.31	Tie to	1233B-8H-1, 95	72.45	84.15	71.31
1233B-8H-5, 125	78.59	90.29	76.52	Tie to	1233D-10H-2, 135	76.05	90.29	76.52
1233D-10H-7, 115	83.07	97.31	82.47	Tie to	1233C-10H-4, 117	83.08	97.31	82.47
1233C-10H-7, 60	87.00	101.23	85.79	Tie to	1233D-11H-2, 84	84.88	101.23	85.79
1233D-11H-8, 20	92.98	109.33	92.65	Tie to	1233E-8H-1, 75	92.75	109.33	92.65
1233E-8H-7, 15	100.66	117.24	99.36	Tie to	1233C-12H-3, 69	99.81	117.24	99.36
1233C-12H-6, 15	103.72	121.15	102.67	Tie to	1233B-11H-3, 74	103.50	121.15	102.67
1233B-11H-6, 60	107.68	125.33	106.21	Tie to	1233D-13H-2, 20	104.50	125.33	106.21
1233D-13H-6, 15	110.38	131.21	111.19	Tie to	1233C-13H-5, 39	111.92	131.21	111.19
1233C-13H-8, 95	116.36	135.65	114.96					

Note: This table is also available in **ASCII.**

Table T4. Secondary composite depth scale, Site 1233.

Core	Depth of core top		Depth offset		Translation to cmcd	
	Drillers (mbsf)	Composite (mcd)	Cumulative (m)	Differential (m)	Growth factor*	Depth (cmcd)†
202-1233A-						
1H	2.5	4.19	1.69		1.18	3.55
202-1233B-						
2H	14.5	16.10	1.60	1.60	1.18	13.64
3H	24.0	27.46	3.46	1.86	1.18	23.27
4H	33.5	39.47	5.97	2.51	1.18	33.45
5H	43.0	50.29	7.29	1.32	1.18	42.62
6H	52.5	61.69	9.19	1.90	1.18	52.28
7H	62.0	72.09	10.09	0.90	1.18	61.09
8H	71.5	82.87	11.37	1.28	1.18	70.23
9H	81.0	93.80	12.80	1.43	1.18	79.49
10H	90.5	105.39	14.89	2.09	1.18	89.31
11H	100.0	117.04	17.04	2.15	1.18	99.19
202-1233C-						
1H	0.0	0.00	0.00		1.18	0.00
2H	7.8	5.97	–1.83	–1.83	1.18	5.06
3H	17.3	18.83	1.53	3.36	1.18	15.96
4H	26.8	28.05	1.25	–0.28	1.18	23.77
5H	30.8	34.86	4.06	2.81	1.18	29.54
6H	40.3	47.53	7.23	3.17	1.18	40.28
7H	49.8	58.53	8.73	1.50	1.18	49.60
8H	59.3	69.25	9.95	1.22	1.18	58.69
9H	68.8	81.89	13.09	3.14	1.18	69.40
10H	78.3	92.15	13.85	0.76	1.18	78.09
11H	87.8	103.27	15.47	1.62	1.18	87.52
12H	97.3	114.13	16.83	1.36	1.18	96.72
13H	106.8	125.04	18.24	1.41	1.18	105.97
202-1233D-						
1H	0.0	0.00	0.00		1.18	0.00
2H	0.3	0.55	0.25	0.25	1.18	0.47
3H	9.8	11.30	1.50	1.25	1.18	9.58
4H	19.3	23.21	3.91	2.41	1.18	19.67
5H	28.8	31.54	2.74	–1.17	1.18	26.73
6H	34.3	40.48	6.18	3.44	1.18	34.31
7H	45.8	54.30	8.50	2.32	1.18	46.02
8H	55.3	65.24	9.94	1.44	1.18	55.29
9H	64.8	77.43	12.63	2.69	1.18	65.62
10H	74.3	88.21	13.91	1.28	1.18	74.75
11H	83.8	99.66	15.86	1.95	1.18	84.46
12H	93.3	109.16	15.86	0.00	1.18	92.51
13H	102.8	123.02	20.22	4.36	1.18	104.25
202-1233E-						
1H	0.0	–0.40	–0.40		1.18	–0.34
2H	8.4	8.88	0.48	0.88	1.18	7.53
3H	17.9	20.60	2.70	2.22	1.18	17.46
4H	27.4	31.14	3.74	1.04	1.18	26.39
5H	36.9	43.64	6.74	3.00	1.18	36.98
6H	46.4	56.04	9.64	2.90	1.18	47.49
7H	82.5	96.75	14.25	4.61	1.18	81.99
8H	92.0	107.97	15.97	1.72	1.18	91.50

Notes: * = calculated based on mbsf-mcd relationship for splice shown in Figure F6, p. 28. † = within the splice, the following equations apply: cmcd = mcd/growth factor, mcd = mbsf + cumulative depth offset, mcd = cmcd × growth factor, mbsf = cmcd × growth factor – cumulative offset. This table is also available in ASCII.

Table T5. Secondary splice tie points, Site 1233.

Hole, core, section, interval (cm)	Depth (mbsf)	Depth (mcd)	Depth (cmcd)		Hole, core, section, interval (cm)	Depth (mbsf)	Depth (mcd)	Depth (cmcd)
202-					202-			
1233B-1H-1	0.00	0.00	0.00					
1233B-1H-3, 60	3.60	3.60	3.05	Tie to	1233E-1H-3, 100	4.00	3.60	3.05
1233E-1H-6, 20	7.70	7.30	6.19	Tie to	1233A-1H-4, 110	5.61	7.30	6.19
1233A-1H-6, 95	8.49	10.18	8.63	Tie to	1233E-2H-1, 130	9.70	10.18	8.63
1233E-2H-5, 145	15.86	16.34	13.85	Tie to	1233B-2H-1, 23.5	14.74	16.34	13.85
1233B-2H-6, 50	22.50	24.10	20.42	Tie to	1233E-3H-3, 50	21.40	24.10	20.42
1233E-3H-6, 100	26.36	29.06	24.63	Tie to	1233C-4H-1, 99	27.81	29.06	24.63
1233C-4H-3, 95	30.74	31.99	27.11	Tie to	1233E-4H-1, 85	28.25	31.99	27.11
1233E-4H-6, 65	35.55	39.29	33.30	Append	1233B-4H-1, 0	33.50	39.47	33.45
1233B-4H-7, 20	42.41	48.38	41.00	Tie to	1233C-6H-1, 85	41.15	48.38	41.00
1233C-6H-3, 105	44.01	51.24	43.42	Tie to	1233B-5H-1, 95	43.95	51.24	43.42
1233B-5H-6, 10	50.30	57.59	48.81	Tie to	1233E-6H-2, 100	47.95	57.59	48.81
1233E-6H-7, 50	54.95	64.59	54.74	Tie to	1233B-6H-2, 140	55.40	64.59	54.74
1233B-6H-6, 105	61.06	70.25	59.53	Tie to	1233C-8H-2, 45	60.30	70.25	59.53
1233C-8H-7, 70	67.89	77.84	65.97	Tie to	1233D-9H-2, 23.5	65.21	77.84	65.97
1233D-9H-3, 5	66.41	79.04	66.98	Tie to	1233B-7H-5, 95	68.95	79.04	66.98
1233B-7H-7, 40	71.41	81.50	69.07	Append	1233C-9H-1, 0	68.80	81.89	69.40
1233C-9H-7, 5	76.87	89.96	76.24	Tie to	1233B-8H-5, 125	78.59	89.96	76.24
1233B-8H-7, 65	80.99	92.36	78.27	Tie to	1233C-10H-1, 19	78.51	92.36	78.27
1233C-10H-4, 35	82.25	96.10	81.44	Tie to	1233B-9H-2, 80	83.30	96.10	81.44
1233B-9H-5, 100	87.50	100.30	85.00	Tie to	1233E-7H-3, 55	86.05	100.30	85.00
1233E-7H-5, 135	89.77	104.02	88.15	Tie to	1233C-11H-2, 30	88.55	104.02	88.15
1233C-11H-5, 10	92.85	108.32	91.80	Tie to	1233B-10H-3, 5	93.43	108.32	91.80
1233B-10H-6, 85	98.20	113.09	95.84	Append	1233C-12H-1, 0	97.30	114.13	96.72
1233C-12H-3, 65	99.75	116.58	98.80	Append	1233B-11H-1, 0	100.01	117.05	99.19
1233B-11H-3, 70	103.46	120.50	102.12	Tie to	1233C-12H-6, 10	103.67	120.50	102.12
1233C-12H-8, 25	106.73	123.56	104.71	Tie to	1233D-13H-1, 53.5	103.34	123.56	104.71
1233D-13H-2, 20	104.50	124.72	105.69	Append	1233C-13H-1, 0	106.81	125.05	105.97
1233C-13H-5, 39	111.90	130.14	110.29					

Note: This table is also available in **ASCII.**

Table T6. OSUS-MS measurements, Hole 1233A.

Core, section, interval (cm)	Depth (mbsf)	Depth (mcd)	Magnetic susceptibility (instrument units)	Run number	Depth from top of core (cm)
202-1233A-					
1H- 1, 5	2.55	3.75	284	166	5
1H- 1, 10	2.60	3.80	162	166	10
1H- 1, 15	2.65	3.85	152	166	15
1H- 1, 20	2.70	3.90	151	166	20
1H- 1, 25	2.75	3.95	152	166	25
1H- 1, 30	2.80	4.00	145	166	30
1H- 1, 35	2.85	4.05	151	166	35
1H- 1, 40	2.90	4.10	157	166	40
1H- 1, 45	2.95	4.15	158	166	45
1H- 1, 50	3.00	4.20	161	166	50
1H- 1, 55	3.05	4.25	162	166	55
1H- 1, 60	3.10	4.30	161	166	60
1H- 1, 65	3.15	4.35	163	166	65
1H- 1, 70	3.20	4.40	163	166	70
1H- 1, 75	3.25	4.45	162	166	75
1H- 1, 80	3.30	4.50	161	166	80
1H- 1, 85	3.35	4.55	157	166	85
1H- 1, 90	3.40	4.60	159	166	90
1H- 1, 95	3.45	4.65	163	166	95
1H- 1, 100	3.50	4.70	171	166	100
1H- 1, 105	3.55	4.75	171	166	105
1H- 1, 110	3.60	4.80	173	166	110
1H- 1, 115	3.65	4.85	173	166	115
1H- 1, 120	3.70	4.90	188	166	120
1H- 1, 125	3.75	4.95	187	166	125
1H- 1, 130	3.80	5.00	166	166	130
1H- 1, 135	3.85	5.05	158	166	135
1H- 1, 140	3.90	5.10	158	166	140
1H- 1, 145	3.95	5.15	165	166	145
1H- 2, 5	4.06	5.26	148	167	155
1H- 2, 10	4.11	5.31	150	167	160
1H- 2, 15	4.16	5.36	142	167	165
1H- 2, 20	4.21	5.41	126	167	170
1H- 2, 25	4.26	5.46	112	167	175
1H- 2, 30	4.31	5.51	116	167	180
1H- 2, 35	4.36	5.56	114	167	185
1H- 2, 40	4.41	5.61	105	167	190
1H- 2, 45	4.46	5.66	112	167	195
1H- 2, 50	4.51	5.71	107	167	200
1H- 2, 55	4.56	5.76	100	167	205
1H- 2, 60	4.61	5.81	104	167	210
1H- 2, 65	4.66	5.86	119	167	215
1H- 2, 70	4.71	5.91	112	167	220
1H- 2, 75	4.76	5.96	107	167	225
1H- 2, 80	4.81	6.01	107	167	230
1H- 2, 85	4.86	6.06	107	167	235
1H- 2, 90	4.91	6.11	113	167	240
1H- 2, 95	4.96	6.16	114	167	245
1H- 2, 100	5.01	6.21	123	167	250
1H- 2, 105	5.06	6.26	136	167	255
1H- 2, 110	5.11	6.31	139	167	260
1H- 2, 115	5.16	6.36	136	167	265
1H- 2, 120	5.21	6.41	128	167	270
1H- 2, 125	5.26	6.46	119	167	275
1H- 2, 130	5.31	6.51	103	167	280
1H- 2, 135	5.36	6.56	97	167	285
1H- 2, 140	5.41	6.61	94	167	290
1H- 2, 145	5.46	6.66	101	167	295
1H- 3, 5	5.58	6.78	94	168	306
1H- 3, 10	5.63	6.83	93	168	311
1H- 3, 15	5.68	6.88	90	168	316
1H- 3, 20	5.73	6.93	94	168	321
1H- 3, 25	5.78	6.98	99	168	326

Note: Only a portion of this table appears here. The complete table is available in **ASCII**.

Table T7. OSUS-MS measurements, Hole 1233B.

Core, section, interval (cm)	Depth (mbsf)	Depth (mcd)	Magnetic susceptibility (instrument units)	Run number	Depth from top of core (cm)
202-1233B-					
1H-1, 5	0.05	0.05	113	173	5
1H-1, 10	0.10	0.10	116	173	10
1H-1, 15	0.15	0.15	119	173	15
1H-1, 20	0.20	0.20	121	173	20
1H-1, 25	0.25	0.25	127	173	25
1H-1, 30	0.30	0.30	145	173	30
1H-1, 35	0.35	0.35	149	173	35
1H-1, 40	0.40	0.40	145	173	40
1H-1, 45	0.45	0.45	136	173	45
1H-1, 50	0.50	0.50	140	173	50
1H-1, 55	0.55	0.55	147	173	55
1H-1, 60	0.60	0.60	147	173	60
1H-1, 65	0.65	0.65	153	173	65
1H-1, 70	0.70	0.70	155	173	70
1H-1, 75	0.75	0.75	160	173	75
1H-1, 80	0.80	0.80	159	173	80
1H-1, 85	0.85	0.85	153	173	85
1H-1, 90	0.90	0.90	152	173	90
1H-1, 95	0.95	0.95	150	173	95
1H-1, 100	1.00	1.00	155	173	100
1H-1, 105	1.05	1.05	157	173	105
1H-1, 110	1.10	1.10	167	173	110
1H-1, 115	1.15	1.15	170	173	115
1H-1, 120	1.20	1.20	169	173	120
1H-1, 125	1.25	1.25	165	173	125
1H-1, 130	1.30	1.30	160	173	130
1H-1, 135	1.35	1.35	156	173	135
1H-1, 140	1.40	1.40	145	173	140
1H-2, 5	1.56	1.56	156	174	155
1H-2, 10	1.61	1.61	161	174	160
1H-2, 15	1.66	1.66	158	174	165
1H-2, 20	1.71	1.71	158	174	170
1H-2, 25	1.76	1.76	167	174	175
1H-2, 30	1.81	1.81	169	174	180
1H-2, 35	1.86	1.86	160	174	185
1H-2, 40	1.91	1.91	155	174	190
1H-2, 45	1.96	1.96	151	174	195
1H-2, 50	2.01	2.01	153	174	200
1H-2, 55	2.06	2.06	157	174	205
1H-2, 60	2.11	2.11	163	174	210
1H-2, 65	2.16	2.16	166	174	215
1H-2, 70	2.21	2.21	170	174	220
1H-2, 75	2.26	2.26	166	174	225
1H-2, 80	2.31	2.31	171	174	230
1H-2, 85	2.36	2.36	179	174	235
1H-2, 90	2.41	2.41	197	174	240
1H-2, 95	2.46	2.46	190	174	245
1H-2, 100	2.51	2.51	161	174	250
1H-2, 105	2.56	2.56	154	174	255
1H-2, 110	2.61	2.61	147	174	260
1H-2, 115	2.66	2.66	136	174	265
1H-2, 120	2.71	2.71	133	174	270
1H-2, 125	2.76	2.76	139	174	275
1H-2, 130	2.81	2.81	150	174	280
1H-2, 135	2.86	2.86	150	174	285
1H-2, 140	2.91	2.91	136	174	290
1H-2, 145	2.96	2.96	108	174	295
1H-3, 5	3.06	3.06	116	175	305
1H-3, 10	3.11	3.11	126	175	310
1H-3, 15	3.16	3.16	125	175	315
1H-3, 20	3.21	3.21	127	175	320
1H-3, 25	3.26	3.26	109	175	325
1H-3, 30	3.31	3.31	102	175	330

Note: Only a portion of this table appears here. The complete table is available in **ASCII**.

Table T8. OSUS-MS measurements, Hole 1233C.

Core, section, interval (cm)	Depth (mbsf)	Depth (mcd)	Magnetic susceptibility (instrument units)	Run number	Depth from top of core (cm)
202-1233C-					
1H-1, 5	0.05	0.05	116	226	5
1H-1, 10	0.10	0.10	115	226	10
1H-1, 15	0.15	0.15	110	226	15
1H-1, 20	0.20	0.20	110	226	20
1H-1, 25	0.25	0.25	114	226	25
1H-1, 30	0.30	0.30	132	226	30
1H-1, 35	0.35	0.35	150	226	35
1H-1, 40	0.40	0.40	158	226	40
1H-1, 45	0.45	0.45	148	226	45
1H-1, 50	0.50	0.50	137	226	50
1H-1, 55	0.55	0.55	140	226	55
1H-1, 60	0.60	0.60	149	226	60
1H-1, 65	0.65	0.65	146	226	65
1H-1, 70	0.70	0.70	140	226	70
1H-1, 75	0.75	0.75	149	226	75
1H-1, 80	0.80	0.80	160	226	80
1H-1, 85	0.85	0.85	162	226	85
1H-1, 90	0.90	0.90	156	226	90
1H-1, 95	0.95	0.95	159	226	95
1H-1, 100	1.00	1.00	155	226	100
1H-1, 105	1.05	1.05	152	226	105
1H-1, 110	1.10	1.10	157	226	110
1H-1, 115	1.15	1.15	164	226	115
1H-1, 120	1.20	1.20	169	226	120
1H-1, 125	1.25	1.25	173	226	125
1H-1, 130	1.30	1.30	169	226	130
1H-1, 135	1.35	1.35	159	226	135
1H-1, 140	1.40	1.40	153	226	140
1H-1, 145	1.45	1.45	145	226	145
1H-2, 5	1.56	1.56	152	227	156
1H-2, 10	1.61	1.61	163	227	161
1H-2, 15	1.66	1.66	158	227	166
1H-2, 20	1.71	1.71	156	227	171
1H-2, 25	1.76	1.76	156	227	176
1H-2, 30	1.81	1.81	168	227	181
1H-2, 35	1.86	1.86	168	227	186
1H-2, 40	1.91	1.91	165	227	191
1H-2, 45	1.96	1.96	158	227	196
1H-2, 50	2.01	2.01	152	227	201
1H-2, 55	2.06	2.06	155	227	206
1H-2, 60	2.11	2.11	161	227	211
1H-2, 65	2.16	2.16	161	227	216
1H-2, 70	2.21	2.21	163	227	221
1H-2, 75	2.26	2.26	170	227	226
1H-2, 80	2.31	2.31	167	227	231
1H-2, 85	2.36	2.36	167	227	236
1H-2, 90	2.41	2.41	172	227	241
1H-2, 95	2.46	2.46	184	227	246
1H-2, 100	2.51	2.51	182	227	251
1H-2, 105	2.56	2.56	160	227	256
1H-2, 110	2.61	2.61	154	227	261
1H-2, 115	2.66	2.66	150	227	266
1H-2, 120	2.71	2.71	140	227	271
1H-2, 125	2.76	2.76	142	227	276
1H-2, 130	2.81	2.81	138	227	281
1H-2, 135	2.86	2.86	139	227	286
1H-2, 140	2.91	2.91	142	227	291
1H-2, 145	2.96	2.96	125	227	296
1H-3, 5	3.07	3.07	106	228	306
1H-3, 10	3.12	3.12	98	228	311
1H-3, 15	3.17	3.17	91	228	316
1H-3, 20	3.22	3.22	96	228	321
1H-3, 25	3.27	3.27	105	228	326

Note: Only a portion of this table appears here. The complete table is available in **ASCII**.

Table T9. OSUS-MS measurements, Hole 1233D.

Core, section, interval (cm)	Depth (mbsf)	Depth (mcd)	Magnetic susceptibility (instrument units)	Run number	Depth from top of core (cm)
202-1233D-					
1H-1, 5	0.05	0.05	273	313	5
1H-1, 10	0.10	0.10	124	313	10
1H-1, 15	0.15	0.15	130	313	15
1H-1, 20	0.20	0.20	136	313	20
1H-1, 25	0.25	0.25	131	313	25
1H-1, 30	0.30	0.30	138	313	30
2H-1, 5	0.35	0.81	143	314	5
2H-1, 10	0.40	0.86	153	314	10
2H-1, 15	0.45	0.91	158	314	15
2H-1, 20	0.50	0.96	161	314	20
2H-1, 25	0.55	1.01	169	314	25
2H-1, 30	0.60	1.06	169	314	30
2H-1, 35	0.65	1.11	168	314	35
2H-1, 40	0.70	1.16	161	314	40
2H-1, 45	0.75	1.21	158	314	45
2H-1, 50	0.80	1.26	159	314	50
2H-1, 55	0.85	1.31	163	314	55
2H-1, 60	0.90	1.36	170	314	60
2H-1, 65	0.95	1.41	170	314	65
2H-1, 70	1.00	1.46	168	314	70
2H-1, 75	1.05	1.51	174	314	75
2H-1, 80	1.10	1.56	183	314	80
2H-1, 85	1.15	1.61	183	314	85
2H-1, 90	1.20	1.66	179	314	90
2H-1, 95	1.25	1.71	166	314	95
2H-1, 100	1.30	1.76	163	314	100
2H-1, 105	1.35	1.81	160	314	105
2H-1, 110	1.40	1.86	157	314	110
2H-1, 115	1.45	1.91	159	314	115
2H-1, 120	1.50	1.96	162	314	120
2H-1, 125	1.55	2.01	163	314	125
2H-1, 130	1.60	2.06	167	314	130
2H-1, 135	1.65	2.11	174	314	135
2H-1, 140	1.70	2.16	172	314	140
2H-1, 145	1.75	2.21	169	314	145
2H-2, 5	1.86	2.32	156	315	155
2H-2, 10	1.91	2.37	187	315	160
2H-2, 15	1.96	2.42	193	315	165
2H-2, 20	2.01	2.47	175	315	170
2H-2, 25	2.06	2.52	165	315	175
2H-2, 30	2.11	2.57	161	315	180
2H-2, 35	2.16	2.62	166	315	185
2H-2, 40	2.21	2.67	174	315	190
2H-2, 45	2.26	2.72	171	315	195
2H-2, 50	2.31	2.77	172	315	200
2H-2, 55	2.36	2.82	160	315	205
2H-2, 60	2.41	2.87	153	315	210
2H-2, 65	2.46	2.92	137	315	215
2H-2, 70	2.51	2.97	124	315	220
2H-2, 75	2.56	3.02	118	315	225
2H-2, 80	2.61	3.07	113	315	230
2H-2, 85	2.66	3.12	100	315	235
2H-2, 90	2.71	3.17	94	315	240
2H-2, 95	2.76	3.22	92	315	245
2H-2, 100	2.81	3.27	114	315	250
2H-2, 105	2.86	3.32	114	315	255
2H-2, 110	2.91	3.37	114	315	260
2H-2, 115	2.96	3.42	108	315	265
2H-2, 120	3.01	3.47	92	315	270
2H-2, 125	3.06	3.52	83	315	275
2H-2, 130	3.11	3.57	85	315	280
2H-2, 135	3.16	3.62	91	315	285
2H-2, 140	3.21	3.67	89	315	290

Note: Only a portion of this table appears here. The complete table is available in **ASCII**.

Table T10. OSUS-MS measurements, Hole 1233E.

Core, section, interval (cm)	Depth (mbsf)	Depth (mcd)	Magnetic susceptibility (instrument units)	Run number	Depth from top of core (cm)
202-1233E-					
1H-1, 10	0.10	–0.24	148	220	10
1H-1, 15	0.15	–0.19	135	220	15
1H-1, 20	0.20	–0.14	117	220	20
1H-1, 25	0.25	–0.09	168	220	25
1H-1, 30	0.30	–0.04	158	220	30
1H-1, 35	0.35	0.01	174	220	35
1H-1, 40	0.40	0.06	140	220	40
1H-1, 45	0.45	0.11	155	220	45
1H-1, 50	0.50	0.16	159	220	50
1H-1, 55	0.55	0.21	151	220	55
1H-1, 60	0.60	0.26	144	220	60
1H-1, 65	0.65	0.31	141	220	65
1H-1, 70	0.70	0.36	144	220	70
1H-1, 75	0.75	0.41	150	220	75
1H-1, 80	0.80	0.46	159	220	80
1H-1, 85	0.85	0.51	154	220	85
1H-1, 90	0.90	0.56	155	220	90
1H-1, 95	0.95	0.61	168	220	95
1H-1, 100	1.00	0.66	168	220	100
1H-1, 105	1.05	0.71	168	220	105
1H-1, 110	1.10	0.76	161	220	110
1H-1, 115	1.15	0.81	171	220	115
1H-1, 120	1.20	0.86	160	220	120
1H-1, 125	1.25	0.91	158	220	125
1H-1, 130	1.30	0.96	159	220	130
1H-1, 135	1.35	1.01	165	220	135
1H-1, 140	1.40	1.06	170	220	140
1H-1, 145	1.45	1.11	176	220	145
1H-2, 5	1.56	1.22	166	221	155
1H-2, 10	1.61	1.27	160	221	160
1H-2, 15	1.66	1.32	160	221	165
1H-2, 20	1.71	1.37	157	221	170
1H-2, 25	1.76	1.42	160	221	175
1H-2, 30	1.81	1.47	166	221	180
1H-2, 35	1.86	1.52	163	221	185
1H-2, 40	1.91	1.57	160	221	190
1H-2, 45	1.96	1.62	160	221	195
1H-2, 50	2.01	1.67	164	221	200
1H-2, 55	2.06	1.72	172	221	205
1H-2, 60	2.11	1.77	167	221	210
1H-2, 65	2.16	1.82	164	221	215
1H-2, 70	2.21	1.87	157	221	220
1H-2, 75	2.26	1.92	155	221	225
1H-2, 80	2.31	1.97	159	221	230
1H-2, 85	2.36	2.02	156	221	235
1H-2, 90	2.41	2.07	161	221	240
1H-2, 95	2.46	2.12	162	221	245
1H-2, 100	2.51	2.17	166	221	250
1H-2, 105	2.56	2.22	184	221	255
1H-2, 110	2.61	2.27	172	221	260
1H-2, 115	2.66	2.32	171	221	265
1H-2, 120	2.71	2.37	180	221	270
1H-2, 125	2.76	2.42	180	221	275
1H-2, 130	2.81	2.47	188	221	280
1H-2, 135	2.86	2.52	172	221	285
1H-2, 140	2.91	2.57	162	221	290
1H-2, 145	2.96	2.62	157	221	295
1H-3, 5	3.07	2.73	147	222	305
1H-3, 10	3.12	2.78	155	222	310
1H-3, 15	3.17	2.83	169	222	315
1H-3, 20	3.22	2.88	154	222	320
1H-3, 25	3.27	2.93	145	222	325
1H-3, 30	3.32	2.98	134	222	330

Note: Only a portion of this table appears here. The complete table is available in **ASCII**.

Table T11. Lithologic Unit I, Site 1233.

Unit	Top Hole, core	Top Depth (mbsf)	Top Depth (mcd)	Base Hole, core	Base Depth (mbsf)	Base Depth (mcd)	Description	Interpretation
	202-			202-				
I	1233A-1H	2.5	3.7	1233A-1H	7.5	8.7	Nannofossil clay, nannofossil silty clay, and nannofossil-bearing silty clay	Hemipelagic sedimentation
I	1233B-1H	0.0	0.0	1233B-11H	109.6	127.2		
I	1233C-1H	0.0	0.0	1233C-13H	116.8	136.1		
I	1233D-1H	0	0	1233D-13H	112.8	133.6		
I	1233E-1H	0	–0.3	1233E-18H	101.3	117.9		

Table T12. Ash layers, Site 1233.

Top			Base				
Hole, core, section	Depth (mbsf)	Depth (mcd)	Hole, core, section	Depth (mbsf)	Depth (mcd)	Thickness (cm)	Lithology
202-			202-				
1233B-2H-1	14.71	16.74	1233B-2H-6	22.80	24.83	Subcentimeter	Interval of silt-rich layers
1233C-2H-4	12.38	11.04	1233C-3H-6	23.16	24.64		
1233D-3H-1	9.81	11.58	1233D-3H-4	15.76	17.53		
1233E-2H-1	8.41	8.78	1233E-3H-3	22.35	24.88		
			1233D-6H-5	41.33	48.18	Subcentimeter	Silt layer
			1233B-8H-4	77.02	88.72	10	Silty sand layer
			1233C-9H-5	75.44	88.91	27	Silty sand layer
			1233C-10H-1	78.98	93.21	7	Silty sand layer
1233C-11H-1	87.81	103.78	1233C-11H-7	96.78	112.75	Subcentimeter	Interval of silt-rich layers
			1233B-11H-2	102.65	120.30	Subcentimeter	Silt layer
			1233C-2H-6	16.16	14.82	8	Ash layer (I)
			1233C-11H-2	88.78	104.75	3	Ash layer (A)
			1233D-12H-2	95.78	112.13	20	Ash layer (I)
			1233E-8H-4	97.40	113.98	15	Ash layer (A)
			1233C-13H-4	110.45	129.74	6	Ash layer (I)
			1233D-13H-5	108.99	129.82	7	Ash layer (I)

Note: A = acidic composition, I = intermediate composition.

Table T13. Distribution of calcareous nannofossils, Site 1233. (**See table notes.** Continued on next page.)

Core, section interval (cm)	Depth (mbsf)	Depth (mcd)	Preservation	Abundance	*Braarudosphaera bigelowii*	*Calcidiscus leptoporus*	*Coccolithus pelagicus*	*Emiliania huxleyi*	*Gephyrocapsa oceanica* (large)	*Gephyrocapsa* spp. (*G. caribbeanica*) (medium)	*Gephyrocapsa* spp. (*G. muellerae*) (medium)	*Gephyrocapsa* spp. (small)	*Helicosphaera carteri*
202-1233A-													
1H-1, 40	0.40	1.60	G	A	R	F	F	F	R		C	C	F
1H-2, 40	1.90	3.10	G	A		F	F	F	F		C	A	F
202-1233B-													
1H-1, 40	0.40	0.40	G	A		F	F	F			F	C	
1H-3, 40	3.41	3.41	G	A		C	F	F	R		F	A	F
1H-CC	5.02	5.02	M	A	R	F	F	R				C	F
2H-1, 40	14.90	16.93	G	A		C		F	C		A	A	F
2H-3, 40	17.92	19.95	G	A	F	C	F	C	F		C	C	F
2H-5, 40	20.94	22.97	G	A		R	R	F	F		C	F	F
2H-7, 40	23.94	25.97	G	C	C	C		F	R		C	A	F
2H-CC	24.63	26.66	G	A	F	F		R				F	C
3H-1, 40	24.40	28.54	G	A		C	F	C			C	C	F
3H-3, 40	27.41	31.55	G	VA		C	C	C			A	A	C
3H-5, 40	30.42	34.56	G	A	F	C	F	F	F		C	A	
3H-7, 40	33.42	37.56	G	A	F	C	C	C			C	C	F
3H-CC	33.68	37.82	G	A	R	F	F	F			C	C	
4H-1, 40	33.90	40.55	G	A	F	F	C	F	R		A	A	
4H-3, 40	36.65	43.30	G	A		R	C	C			C	C	F
4H-5, 40	39.64	46.29	G	C		R	F	F			C	C	
4H-7, 40	42.64	49.29	G	A		R	C	R			A	A	
4H-CC	43.45	50.10	G	A	F		F				C	C	F
5H-1, 40	43.40	50.97	G	A	R	F	F	F			C	A	
5H-3, 40	46.42	53.99	G	A	R	R	F	C			C	F	
5H-5, 40	49.14	56.71	G	A		F	F	R			A	C	
5H-7, 40	52.15	59.72	G	A		C	C	F			C	A	
5H-CC	52.83	60.40	G	A		F	F	R			C	C	F
6H-1, 40	52.90	62.62	M	C		F	R	R			C	C	
6H-3, 40	55.91	65.63	M	A		F	R	R	R		A	C	R
6H-5, 40	58.94	68.66	M	A		C	F	F			C	A	F
6H-7, 40	61.96	71.68	G	C		F		F			C	C	
6H-CC	62.80	72.52	G	A		F	F	F			F	F	R
7H-1, 40	62.40	72.82	G	C		F	R	F			C	C	F
7H-3, 40	65.41	75.83	M	A		F	C	F	R		A	C	F
7H-5, 40	68.42	78.84	G	A		C	F	R			A	A	F
7H-7, 40	71.43	81.85	G	A		F	R	F			A	C	
7H-CC	71.79	82.21	G	A		F	F	R			C	C	F
8H-1, 40	71.90	83.60	G	C		F		C			C	F	R
8H-3, 40	74.91	86.61	M	C		F	F	F			A	F	R
8H-5, 40	77.72	89.42	G	A		R	R	R			A	A	
8H-7, 40	80.72	92.42	G	A		F	F	F			C	A	
8H-CC	81.33	93.03	G	A		F	F	R			C	A	F
9H-1, 40	81.40	94.58	G	VA		C	C	R			A	A	F
9H-3, 40	83.91	97.09	G	A		F	F	F			A	A	F
9H-5, 40	86.92	100.10	G	VA		C	F	F			A	A	F
9H-7, 40	89.94	103.12	M	A		R	F	R			A	A	F
9H-CC	90.88	104.06	G	A		R		R			F	C	
10H-1, 40	90.90	106.28	G	A		F	R	F			C	A	C
10H-3, 40	93.79	109.17	G	C		F	R	R			F	C	
10H-5, 40	96.66	112.04	M	C		F	F	C				F	
10H-6, 40	98.16	113.54	M	C		F	F	C				F	
10H-CC	98.43	113.81	P	C		F	F					C	
11H-1, 40	100.40	118.05	M	C		F	R	F		F	C	F	

Table T13 (continued).

Core, section interval (cm)	Depth (mbsf)	Depth (mcd)	Preservation	Abundance	*Braarudosphaera bigelowii*	*Calcidiscus leptoporus*	*Coccolithus pelagicus*	*Emiliania huxleyi*	*Gephyrocapsa oceanica* (large)	*Gephyrocapsa* spp. (*G. caribbeanica*) (medium)	*Gephyrocapsa* spp. (*G. muellerae*) (medium)	*Gephyrocapsa* spp. (small)	*Helicosphaera carteri*
11H-3, 40	103.17	120.82	M	C		F	F	R	F	C	R	A	R
11H-5, 40	106.14	123.79	M	A		F	C		F	A	F	C	
11H-7, 40	108.95	126.60	M	A		R		F		C	R	C	F
11H-CC	109.51	127.16	G	A		R		R			C	C	F

Notes: Preservation: G = good, M = moderate, P = poor. Abundance: VA = very abundant, A = abundant, C = common, F = few, R = rare.

Table T14. Distribution of foraminifers, Hole 1233B. (Continued on next page.)

Core, section,	Depth (mbsf)	Depth (mcd)	Preparation	Preservation	Abundance	Benthic/planktonic foraminifers (%)	*Globigerina bulloides*	*Globigerinita glutinata*	*Globorotalia scitula*	*Globorotalia inflata*	*Globorotalia truncatulinoides*	*Globorotalia ungulata*	*Neogloboquadrina dutertrei*	*Neogloboquadrina pachyderma* (s)	*Neogloboquadrina pachyderma* (d)	*Orbulina universa*	*Bolivina* spp.	*Bulimina marginata*	*Bulimina tuxpamensis*	*Bulimina* spp.	*Cassidulina teretis*	*Cassidulinoides* sp.	*Chilostomella ovoidea*	*Cibicidoides lobatulus*	*Cibicidoides* spp.	*Ehrenbergina serrata*	*Eubuliminella exilis*	*Fissurina* spp.	*Globobulimina affinis*	*Globobulimina pyrula*	*Globocassidulina subglobosa*	*Globulina prisca*	*Globulina* spp.	*Gyroidinoides orbicularis*	*Gyroidinoides soldanii*	*Hoeglundina elegans*	*Laevidentalina* sp.	*Martinotiella communis*	*Melonis affinis*	*Melonis* spp.	Miliolids	*Nonionella auris*	*Nonionella* spp.
202-1233B-																																									
1H-CC	5.02	5.02	S	G	A	25/75	C	C			F		C		C	F		3			1		21		1			16	6			1			1	11	9			40	
2H-CC	24.63	26.66	S	G	A	30/70	C			C				F		R	1	13			1		5			1	4	3	20			4		2	11				3	5	
3H-CC	33.68	37.82	S	G	A	15/85	C	R		F	C			F						1	21		4			1		2	3	9	2						1			26	
4H-CC	43.45	50.10	S	G	A	50/50	A		R	R	R	R		F		R		4			7					2			10	18					2			1			46	1
5H-CC	52.83	60.40	S	G	A	35/65	A	C		F	C			F		R		8			8			1		4	9		6	4		3							4	50	
6H-CC	62.80	72.52	S	G	A	35/65	A	C		C	C	R		F				19			9					4	5		4	38		4			4			1		3	
7H-CC	71.79	82.21	S	G	A	40/60	A		R	C	F	R		F						19	3	1	1		2	7	3	5	2	6		1			1			7	1	11	2
8H-CC	81.33	93.03	S	G	A	15/85	A	A	R	F	F	F	R		C		1	9			37					1		5					1		4			3	1	6	3
9H-CC	90.88	104.06	S	G	A	30/70	A	F	R		C	F		C				2			17			4	1	2	3	8	2			6			17			6		23	1
10H-CC	98.43	113.81	S	G	A	20/80	C	F	R	C	F	F		F		R			37		6		19		2		1	2	5	3					9			2			
11H-CC	109.51	127.16	S	G	A	43/57	C	F		C		R		R		F			2		13	1				15	1	1				2	1	1		11			11		2	

Notes: Preparation: S = sieve. Preservation: G = good. Abundance: A = abundant, C = common, F = few, R = rare.

Table T14 (continued).

Core, section	Depth (mbsf)	Depth (mcd)	Preparation	Preservation	Abundance	Benthic/Planktonic foraminifers (%)	*Nuttalides umbonifera*	*Oolina sulcata*	*Oolina* spp.	*Peneroplis* sp.	*Planulina wuellerstorfi*	*Praeglobobulimina spinescens*	*Protoglobobulimina pupoides*	*Proxifrons advena*	*Pullenia bulloides*	*Pullenia quinqueloba*	*Pyrgo serrata*	*Pyrgo* spp.	*Quinqueloculina* spp.	*Rutherfordoides mexicanus*	*Trifarina tricarinata*	*Uvigerina peregrina*	*Uvigerina* sp. 1
202-1233B-																							
1H-CC	5.02	5.02	S	G	A	25/75	16		1		17	3			2	1	22	9		13			
2H-CC	24.63	26.66	S	G	A	30/70					12	12			18		18	8	5	1		5	
3H-CC	33.68	37.82	S	G	A	15/85	2				1	4				13		6	5	3		26	
4H-CC	43.45	50.1	S	G	A	50/50	3	2		1	2	17			4	2	2	2	7	1	1	6	
5H-CC	52.83	60.4	S	G	A	35/65	1	2			16					1	3	1	3			13	
6H-CC	62.8	72.52	S	G	A	35/65	1				1		1		7	7	6		3	1			1
7H-CC	71.79	82.21	S	G	A	40/60	6				7	4			19		3	2	1		15	9	
8H-CC	81.33	93.21	S	G	A	15/85		2			1					17			3		10	21	
9H-CC	90.88	103.95	S	G	A	30/70	2	4			21					3	5				2		10
10H-CC	98.43	113.7	S	G	A	20/80		1	1		1	3	6	1	1	1		1	5	1	42		10
11H-CC	109.51	127.05	S	G	A	43/57					3			1		2	3	4	5		71	1	

Table T15. Distribution of diatoms, Holes 1233A, 1233B, and 1233C.

Hole, core, section, interval (cm)	Depth (mbsf)	Depth (mcd)	Identification	Method	Abundance	Preservation	*Actinocyclus curvatulus*	*Actinoptychus senarius*	*Aulacoseira granulata*	*Azpetia nodulifer*	*Chaetoceros* spp. (resting spores)	*Delphineis* spp.	*Fragilariopsis doliolus*	*Hemidiscus cuneiformis*	*Paralia sulcata*	*Pseudonitzschia*	*Roperia tesselata*	*Thalassionema nitzschioides*	*Thalassiosira* spp.	Freshwater benthic	Freshwater species (planktonic)	Marine benthic species	Marine neritic species (other)	Marine pelagic species (other) COSM	Marine pelagic species (other) WW	Marine pelagic species (other) CW
202-																										
Mudline	0.00	0.00	PAL	S	A	G		T	T		A				C			F	C–A		T		R	T		
1233B-1H-CC, 23–28	5.02	5.02	PAL	S	A	G			T		A	R			F			F	C	T	T	R	R			
1233C-1H-CC, 45–50	7.88	7.88	PAL	S	C–A	M–G					C–A	T			C				C	T	T	T	T	T		
1233A-1H-CC, 22–27	12.49	13.69	PAL	S	C–A	M–G			T		A	F	R		R			F	F–C	T	T	T	F			
1233B-2H-1, 40	14.90	16.93	Toothpick	S	F–C	M				T	C				R	R		R	C				F	T	T	
1233B-2H-3, 40	17.92	19.95	Toothpick	S	F	M		T			F	R						T	F		T	R		T		T
1233C-2H-CC, 26–31	18.03	20.06	PAL	S	F–C	M			T		A							C	C		T	T	T	T		R
1233B-2H-5, 40	20.94	22.97	Toothpick	S	F	M	T		T	T	F–C					T		T	F		T					
1233B-2H-7, 40	23.94	25.97	Toothpick	S	F	M	T				F	T				T			F			T	T	T		T
1233B-3H-1, 40	24.40	28.54	Toothpick	S	F	G				T	F					F			F				T			
1233B-2H-CC, 31–36	24.63	26.66	PAL	S	C–A	M–G		R	R		C–A	R				T		R	F–C	R	R	F–C	R			
1233B-3H-2, 40	25.91	30.05	Toothpick	S	C	M	T		T		F–C				T				R	T	T	F	T			
1233C-3H-CC, 31–36	26.83	28.31	PAL	S	C	M			T		A							T	C		T					
1233B-3H-3, 40	27.41	31.55	Toothpick	S	C	G			T		C	T				F			C		R	T	T			
1233B-3H-5, 40	30.42	34.56	Toothpick	S	C	M					C	F				F			C			R	R			
1233C-4H-CC, 32–37	32.45	34.09	PAL	S	A	G			T		A	F				F		T	C		T				T	
1233B-3H-7, 40	33.13	37.27	Toothpick	S	F–C	M	T				F								F							
1233B-3H-CC, 26–31	33.68	37.82	PAL	S	C–A	G			T	T	C	R							F	F	F	T	R	T		
1233B-4H-1, 40	33.90	40.55	Toothpick	S	F–C	M					F								C			R				
1233B-4H-3, 40	36.65	43.30	Toothpick	S	C	M		T	T		F					F			C		T		T			
1233B-4H-5, 40	39.64	46.29	Toothpick	S	A	G	T				A					T			A			T		T		
1233C-5H-CC, 33–38	39.83	45.13	PAL	S	A	G			T		A					R			A	T	T	T	T			
1233B-4H-7, 40	42.64	49.29	Toothpick	S	A	G					A	R				T			A				R			
1233B-5H-1, 40	43.40	50.97	Toothpick	S	C	M			T–R		C					T			C		R	F				
1233B-4H-CC, 43–48	43.45	50.10	PAL	S	C–A	M–G			T		C–A								F	T	R	R	R			
1233B-5H-3, 40	46.42	53.99	Toothpick	S	F	M				R	F					T			C							
1233B-5H-5, 40	49.14	56.71	Toothpick	S	A	G	F				C								C			T				R
1233C-6H-CC, 42–47	50.20	57.71	PAL	S	C	M					C					R	T		F	R		R		R		
1233B-5H-7, 40	52.15	59.72	Toothpick	S	C	M–G	R				C					F		F	C							
1233B-5H-CC, 25–30	52.83	60.40	PAL	S	C–A	G				T	C–A					T		F	C	T	T		T			
1233B-6H-1, 40	52.90	62.62	Toothpick	S	C	M	T				C	F				T		F	F			R	T			
1233B-6H-3, 40	55.91	65.63	Toothpick	S	A	M	T		T		A					F			C	T	T					
1233B-6H-5, 40	58.94	68.66	Toothpick	S	C	M–G	F				C								C							
1233C-7H-CC, 42–47	59.61	68.90	PAL	S	A	G					A	T							A	T		T				T
1233B-6H-7, 40	61.96	71.68	Toothpick	S	C	M–G					C	T				F			C				T			
1233B-6H-CC, 37–42	62.80	72.52	PAL	S	C–A	M–G			T	R	C							R	C		T	F	T	T		
1233C-8H-CC, 38–43	68.99	79.27	PAL	S	C	G		R		T	A	T						R	C				C	T		
1233B-7H-CC, 30–35	71.79	82.21	PAL	S	A	M–G					C	R				R		T	C			R	F			
1233B-8H-2, 40	73.40	85.28	Toothpick	S	C–A	G	R		F	F	C–A					T			F–C		F	T	T			
1233B-8H-4, 40	76.22	88.10	Toothpick	S	6	G	F			R–F	A	F–C		T		T		F	F–C	T	T	T	F	T		
1233C-9H-CC, 35–40	78.46	91.93	PAL	S	A	G				F	C	R							C			T	F	T	T	
1233B-8H-CC, 29–34	81.33	93.21	PAL	S	A	G				R	C–A							F	C	T	T	R	F	T		
1233B-9H-2, 40	82.91	95.98	Toothpick	S	C–A	M–G			T	F	C	T				T			R		T	R	F	T		
1233B-9H-4, 40	85.41	98.48	Toothpick	S	F–C	P–M			R	R	C	T							F–C		R	T	T			
1233C-10H-CC, 38–43	88.32	102.45	PAL	S	C–A	M				R	A	R				R			C			T	T			
1233B-9H-CC, 32–37	90.88	103.95	PAL	S	A	G			R		A	F	T						C	T	R	T	F			
1233B-10H-1, 40	90.90	106.17	Toothpick	S	C	M			R		C	F				T		F	C	T	R	T	R	T		
1233B-10H-2, 40	92.41	107.68	Toothpick	S	C	M	F			F	C								R	R	R	T	F	T		
1233B-10H-3, 40	93.79	109.06	Toothpick	S	C	M			T		C	F				T		R	F–C	R	F	T	T			
1233B-10H-4, 40	95.29	110.56	Toothpick	S	C–A	M–G	R				C–A	R						T	F				F			
1233C-11H-CC, 38–43	97.20	113.07	PAL	S	A	G					A	F						T	C				T			
1233B-10H-CC, 9–14	98.43	113.70	PAL	S	C	M			R		C							T	F		R	R	R	T		
1233C-12H-CC, 54–59	107.83	125.16	PAL	S	F	M			T	R	F					T		T	F		T					
1233B-11H-CC, 50–55	109.51	127.05	PAL	S	C	M			T		C	T				T		T	F		T	T	F	R		
1233C-13H-8, 30–35	115.71	134.90	PAL	S	F–C	M					F	T							F			T		T		

Notes: PAL = paleontology samples. S = sieve. Abundance: A = abundant, C = common, F = few. Preservation: G = good, M = moderate, P = poor. COSM = cosmopolitan forms, WW = warm-water forms, CW = cold-water forms.

Table T16. Headspace and vacutainer gas concentrations and C_1/C_2 ratio, Hole 1233B.

Core, section, interval (cm)	Depth (mbsf)	Depth (mcd)	Sample method	C_1 (ppmv)	C_2 (ppmv)	C_1/C_2
202-1233B-						
1H-2, 0–5	1.51	1.51	HS	11	0.0	
2H-4, 0–5	19.03	21.06	HS	11,236	0.0	
2H-5, 50–51	21.04	23.07	VAC	955,456	9.7	98,501
3H-4, 0–5	28.52	32.66	HS	25,902	0.0	
4H-2, 50–51	35.50	42.15	VAC	946,526	17.4	54,398
4H-4, 0–5	37.73	44.38	HS	22,833	0.7	32,619
5H-4, 0–5	47.23	54.80	HS	23,876	1.0	23,876
6H-4, 0–5	57.02	66.74	HS	40,550	2.7	15,018
6H-5, 50–51	59.04	68.76	VAC	967,700	39.8	24,314
8H-3, 60–61	75.11	86.81	VAC	951,138	57.4	16,570
8H-4, 0–5	75.82	87.52	HS	5,649	0.7	8,069
9H-3, 80–81	84.31	97.49	VAC	968,238	68.4	14,156
9H-4, 0–5	85.01	98.19	HS	5,125	0.8	6,406
10H-4, 0–5	94.89	110.27	HS	3,273	0.4	8,182
11H-3, 130–131	104.07	121.72	VAC	973,878	84.3	11,553
11H-4, 0–5	104.23	121.88	HS	7,507	1.5	5,004

Note: HS = headspace, VAC = vacutainer.

Table T17. Interstitial water geochemical data, Holes 1233B and 1233C.

Core, section, interval (cm)	Depth (mbsf)	Depth (mcd)	pH	Alkalinity (mM)	Salinity	Cl^- (mM)	Na^+ (mM)	SO_4^{2-} (mM)	HPO_4^{2-} (µM)	NH_4^+ (mM)	H_4SiO_4 (µM)	Mn^{2+} (µM)	Fe^{2+} (µM)	Ca^{2+} (mM)	Mg^{2+} (mM)	B (µM)	Sr^{2+} (µM)	Ba^{2+} (µM)	Li^+ (µM)	K^+ (mM)
202-1233B-																				
1H-1, 145–150	1.45	1.45	7.76	21.3	34.0	561	484	12.5	128	1.67	500	3.3	1	5.9	50.1	570	73	1.5	21	11.1
2H-3, 145–150	18.97	21.00	7.87	67.7	36.0	552	484	BDL	214	7.04	570	2.7	8	2.2	59.0	811	51	7.9	20	13.4
3H-3, 145–150	28.46	32.60	7.86	68.6	34.0	550	481	BDL	252	7.04	637	2.3	12	2.3	60.0	855	52	4.5	24	13.2
4H-3, 142–150	37.67	44.32	7.89	67.6	36.0	556	492	BDL	244	7.61	576	2.1	13	2.7	56.9	843	53	6.4	23	12.0
5H-3, 115–120	47.17	54.74	7.97	47.3	35.0	542	462	BDL	211	7.71	604	1.9	10	2.8	55.1	804	54	5.5	25	11.4
6H-3, 145–150	56.96	66.68	7.98	57.8	35.0	530	461	BDL	209	6.84	586	2.3	10	3.0	54.4	806	55	7.3	23	11.7
7H-3, 145–150	66.46	76.88	8.10	53.6	35.0	522	459	BDL	145	5.73	584	3.2	5	2.1	50.1	728	48	7.6	23	12.3
8H-3, 125–130	75.76	87.46	8.01	47.7	34.0	518	457	BDL	200	4.49	553	3.2	5	1.4	47.0	677	43	7.4	23	11.7
9H-3, 145–150	84.96	98.14	8.11	36.7	34.0	501	435	BDL	186	3.65	611	2.1	1	0.7	44.9	570	37	2.4	18	11.5
10H-3, 140–145	94.79	110.17	8.02	32.9	31.0	489	418	BDL	198	3.53	537	2.2	7	1.1	45.9	641	42	3.0	22	10.3
11H-3, 135–145	104.12	121.77	8.05	30.1	30.0	495	426	BDL	209	3.08	661	2.6	2	1.4	43.0	596	44	6.3	21	10.0
202-1233C-																				
1H-3, 145–150	4.47	4.47	7.83	45.3	34.0	556	484	BDL	190	3.88	480	2.2	6	1.8	51.0	735	74	35.9	15	11.5
2H-3, 150–155	12.32	10.98	7.86	58.4	35.0	558	486	BDL	217	5.98	498	4.1	53	2.0	56.7	850	65	24.9	19	12.9
3H-3, 145–150	21.69	23.17	7.85	66.9	37.0	551	485	BDL	288	7.08	536	2.8	13	2.2	58.2	832	54	7.5	21	12.2

Note: BDL = below detection limit (SO_4^{2-} = ~0.5 mM).

Table T18. Inorganic carbon, calcium carbonate, total carbon, total organic carbon, and total nitrogen concentrations, and TOC/TN ratio, Holes 1233A, 1233B, and 1233E. (**See table notes**. Continued on next page.)

Hole, core, section, interval (cm)	Depth (mbsf)	Depth (mcd)	IC (wt%)	$CaCO_3$ (wt%)	TC (wt%)	TOC (wt%)	TN (wt%)	TOC/TN (atomic)
202-								
1233B-1H-1, 74–75	0.74	0.74	1.09	9.1	2.98	1.89	0.23	7.17
1233B-1H-2, 74–75	2.25	2.25	1.01	8.4	2.64	1.63	0.23	6.07
1233B-1H-3, 74–75	3.75	3.75	0.85	7.1	2.92	2.07	0.26	6.80
1233A-1H-1, 74–75	3.24	4.44	0.86	7.2	2.75	1.89	0.23	7.02
1233A-1H-2, 74–75	4.75	5.95	0.77	6.4	2.76	2.42	0.24	8.75
1233A-1H-3, 74–75	6.27	7.47	1.28	10.6	2.90	1.62	0.20	7.01
1233A-1H-4, 74–75	7.78	8.98	1.16	9.7	2.81	1.65	0.20	6.98
1233E-2H-1, 74–75	9.14	9.51	1.24	10.4				
1233A-1H-5, 74–75	9.30	10.50	1.29	10.8	2.87	1.58	0.20	6.88
1233E-2H-2, 74–75	10.65	11.02	1.08	9.0				
1233A-1H-6, 74–75	10.83	12.03	1.15	9.6	2.62	1.47	0.18	6.95
1233E-2H-3, 74–75	12.16	12.53	1.07	8.9				
1233A-1H-7, 20–21	11.79	12.99	0.96	8.0	2.41	1.45	0.18	6.88
1233E-2H-4, 74–75	13.68	14.05	0.96	8.0				
1233E-2H-5, 74–75	15.20	15.57	0.97	8.1				
1233E-2H-6, 74–75	16.71	17.08	1.07	8.9				
1233B-2H-1, 74–75	15.24	17.27	1.13	9.4	2.21	1.08	0.15	6.17
1233E-2H-7, 20–21	17.66	18.03	0.73	6.1				
1233B-2H-2, 74–75	16.75	18.78	0.98	8.2	1.95	0.97	0.13	6.60
1233B-2H-3, 74–75	18.26	20.29	0.74	6.2	1.83	1.09	0.13	7.19
1233B-2H-4, 74–75	19.77	21.80	0.68	5.7	1.61	0.93	0.12	6.64
1233B-2H-5, 74–75	21.28	23.31	0.87	7.2	1.64	0.77	0.10	6.60
1233B-2H-6, 74–75	22.78	24.81	0.49	4.1	1.34	0.85	0.11	6.81
1233B-2H-7, 20–21	23.74	25.77	0.68	5.7				
1233B-3H-1, 74–75	24.74	28.88	0.67	5.5	1.44	0.77	0.10	6.58
1233B-3H-2, 74–75	26.25	30.39	0.70	5.9	1.43	0.73	0.11	5.71
1233B-3H-3, 74–75	27.75	31.89	0.81	6.8	1.64	0.83	0.11	6.47
1233B-3H-4, 74–75	29.26	33.40	0.58	4.9	1.27	0.69	0.09	6.57
1233B-3H-5, 74–75	30.76	34.90	0.55	4.6	1.28	0.73	0.11	5.69
1233B-3H-6, 74–75	32.26	36.40	0.60	5.0	1.45	0.85	0.11	6.62
1233B-3H-7, 20–21	32.93	37.07	0.37	3.1	1.02	0.65	0.09	6.19
1233B-4H-1, 74–75	34.24	40.89	0.57	4.8	1.23	0.66	0.09	6.29
1233B-4H-2, 74–75	35.74	42.39	0.51	4.3	1.18	0.67	0.09	6.38
1233B-4H-3, 74–75	36.99	43.64	0.37	3.1	0.93	0.56	0.08	6.00
1233B-4H-4, 74–75	38.47	45.12	0.19	1.6	0.93	0.74	0.09	7.05
1233B-4H-5, 74–75	39.98	46.63	0.40	3.3	1.31	0.91	0.11	7.09
1233B-4H-6, 74–75	41.48	48.13	0.33	2.8	1.02	0.69	0.09	6.57
1233B-4H-7, 20–21	42.44	49.09	0.58	4.9	1.53	0.95	0.11	7.40
1233B-5H-1, 74–75	43.74	51.31	0.29	2.4	0.93	0.64	0.09	6.10
1233B-5H-2, 74–75	45.25	52.82	0.34	2.9	0.99	0.65	0.09	6.19
1233B-5H-3, 74–75	46.76	54.33	0.41	3.5	1.25	0.84	0.11	6.55
1233B-5H-4, 74–75	47.97	55.54	0.58	4.8	1.42	0.84	0.10	7.20
1233B-5H-5, 74–75	49.48	57.05	0.33	2.7	0.99	0.66	0.08	7.07
1233B-5H-6, 74–75	50.98	58.55	0.27	2.2	1.28	1.01	0.12	7.21
1233B-5H-7, 20–21	51.95	59.52	0.60	5.0	1.37	0.77	0.10	6.60
1233B-7H-1, 74–75	62.74	73.16	0.31	2.6	1.04	0.73	0.10	6.41
1233B-7H-2, 74–75	64.24	74.66	0.55	4.6	1.15	0.60	0.08	6.57
1233B-7H-3, 74–75	65.75	76.17	0.59	5.0	1.28	0.69	0.11	5.45
1233B-7H-4, 74–75	67.25	77.67	0.69	5.7	1.42	0.73	0.12	5.09
1233B-7H-5, 74–75	68.76	79.18	0.42	3.5	1.21	0.79	0.10	6.54
1233B-7H-6, 74–75	70.26	80.68	0.61	5.1	1.38	0.77	0.10	6.66
1233B-7H-7, 20–21	71.23	81.65	0.33	2.7	1.07	0.74	0.09	6.90
1233B-8H-1, 74–75	72.24	83.94	1.01	8.5	1.65	0.64	0.08	6.74
1233B-8H-2, 74–75	73.74	85.44	0.35	2.9	0.92	0.57	0.08	6.44
1233B-8H-3, 74–75	75.25	86.95	0.82	6.8	1.77	0.95	0.11	7.53
1233B-8H-4, 74–75	76.56	88.26	0.37	3.1	1.43	1.06	0.12	7.73
1233B-8H-5, 74–75	78.06	89.76	0.62	5.1	1.70	1.08	0.12	7.49
1233B-8H-6, 74–75	79.56	91.26	0.76	6.3	1.58	0.82	0.10	7.03
1233B-8H-7, 20–21	80.52	92.22	0.54	4.5	1.68	1.14	0.13	7.73
1233B-9H-1, 74–75	81.74	94.92	0.94	7.8	1.60	0.66	0.08	6.97
1233B-9H-2, 74–75	83.25	96.43	0.84	7.0	1.53	0.69	0.08	7.37
1233B-9H-3, 74–75	84.25	97.43	0.86	7.1	1.29	0.43	0.06	6.42
1233B-9H-4, 74–75	85.75	98.93	0.49	4.1	0.89	0.40	0.05	6.65
1233B-9H-6, 74–75	88.77	101.95	0.39	3.2	0.90	0.51	0.06	6.98

Table T18 (continued).

Hole, core, section, interval (cm)	Depth (mbsf)	Depth (mcd)	IC (wt%)	$CaCO_3$ (wt%)	TC (wt%)	TOC (wt%)	TN (wt%)	TOC/TN (atomic)
1233B-9H-7, 74–75	90.28	103.46	0.30	2.5	0.89	0.59	0.07	7.24
1233B-10H-1, 74–75	91.24	106.62	0.51	4.3	1.01	0.50	0.06	6.85
1233B-10H-2, 74–75	92.75	108.13	0.15	1.2	0.60	0.45	0.06	6.88
1233B-10H-3, 74–75	94.13	109.51	0.21	1.8	0.85	0.64	0.07	7.50
1233B-10H-4, 74–75	95.63	111.01	0.36	3.0	1.48	1.12	0.11	8.41
1233B-10H-5, 74–75	97.00	112.38	0.20	1.7	0.69	0.49	0.06	6.99
1233B-10H-6, 74–75	98.17	113.55	0.61	5.1	1.09	0.48	0.06	6.58
1233B-11H-1, 74–75	100.74	118.39	0.38	3.1	0.76	0.38	0.05	5.94
1233B-11H-2, 74–75	102.22	119.87	0.30	2.5	0.67	0.37	0.06	5.52
1233B-11H-3, 74–75	103.51	121.16	0.29	2.4	1.04	0.75	0.09	7.35
1233B-11H-4, 74–75	104.97	122.62	0.67	5.6	1.22	0.55	0.07	6.65
1233B-11H-5, 20–21	105.94	123.59	0.76	6.3	1.44	0.68	0.08	7.37
1233B-11H-6, 74–75	107.89	125.54	0.35	2.9	0.73	0.38	0.06	5.44

Notes: IC = inorganic carbon, TC = total carbon, TOC = total organic carbon, TN = total nitrogen. The data from different holes are treated as constituting single profiles in meters composite depth (mcd).

Table T19. Age control points, Site 1233.

Depth (mcd)	Assigned age (ka)	Sedimentation rates (cm/k.y.)	Corrected sedimentation rates (cm/k.y.)*	Age control event
0.56	0.260			AMS ^{14}C (core GeoB 3313)
		145	119	
1.89	1.180			AMS ^{14}C (core GeoB 3313)
		143	117	
3.03	1.980			AMS ^{14}C (core GeoB 3313)
		85	70	
4.59	3.820			AMS ^{14}C (core GeoB 3313)
		110	90	
5.93	5.040			AMS ^{14}C (core GeoB 3313)
6.80	5.590	138	113	AMS ^{14}C (core GeoB 3313)
8.76	7.090			AMS ^{14}C (core GeoB 3313)
		173	142	
67.50	41.000			Laschamp Excursion
		150	123	
75.00	46.000			Paleomagnetic intensities
		50	41	
84.50	65.000			Paleomagnetic intensities
		44	36	
94.58	88.000			Paleomagnetic intensities
		76	62	
106.00	103.000			Paleomagnetic intensities
		33	27	
112.00	121.000			Paleomagnetic intensities
		50	41	
135.72	168.000			Extrapolated bottom age

Note: * = sedimentation rates reduced by 18% to correct for elastic rebound and gas expansion.

Table T20. Age-depth model, linear sedimentation rates, and mass accumulation rates, Site 1233.

Age (Ma)	Depth (mcd)	LSR (mcd/m.y.)	mcd growth factor	Corrected LSR (m/m.y.)	Dry density (g/cm^3)	$CaCO_3$ average concentration (wt%)	TOC average concentration (wt%)	Total MAR ($g/cm^2/k.y.$)	$CaCO_3$ MAR ($g/cm^2/k.y.$)	TOC MAR ($g/cm^2/k.y.$)	Noncarbonate MAR ($g/cm^2/k.y.$)
0.0	0.0										
10.0	13.2	132	1.18	112	0.72	8.9	1.32	81	7.2	1.07	74
20.0	30.4	172	1.18	146	0.89	7.0	0.74	130	9.1	0.96	121
30.0	49.3	189	1.18	160	0.96	4.2	0.74	154	6.5	1.14	148
40.0	65.8	165	1.18	140	0.97	3.4	0.77	136	4.6	1.05	132
50.0	76.2	104	1.18	88	0.98	3.6	0.67	86	3.1	0.57	83
60.0	81.6	54	1.18	46	0.94	4.8	0.75	44	2.1	0.32	41
70.0	86.8	52	1.18	44	1.01	4.7	0.65	45	2.1	0.29	43
80.0	92.0	52	1.18	44	0.94	5.4	0.98	41	2.2	0.40	39
90.0	97.2	52	1.18	44	0.96	6.4	0.83	42	2.7	0.35	39
100.0	102.4	52	1.18	44	1.03	5.9	0.97	45	2.7	0.44	43
110.0	107.6	52	1.18	44	1.01	3.4	0.55	44	1.5	0.24	43
120.0	112.8	52	1.18	44	1.01	1.9	0.68	44	0.9	0.30	43
130.0	118.0	51	1.18	44	1.05	5.1	0.48	46	2.3	0.22	44
140.0	123.1	51	1.18	43	1.04	3.4	0.51	45	1.5	0.23	44
150.0	128.2	51	1.18	43	1.07	4.6	0.53	46	2.1	0.25	44

Notes: LSR = linear sedimentation rate, MAR = mass accumulation rate. TOC = total organic carbon. This table is also available in **ASCII.**